CHARGE TRANSPORT IN POLYMER SEMICONDUCTOR FIELD-EFFECT TRANSISTORS

GUO HAN

A THESIS SUBMITTED FOR THE DEGREE OF DOCTOR OF PHILOSOPHY

DEPARTMENT OF PHYSICS

NATIONAL UNIVERSITY OF SINGAPORE

2014

Declaration

I hereby declare that the thesis is my original work and it has been written by me in its entirety.

I have duly acknowledged all the sources of information which have been used in the thesis.

This thesis has also not been submitted for any degree in any university previously.

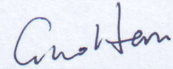

GUO Han

08 / 05 / 2014

Acknowledgements

The work described in this thesis was carried out in Organic Nano Device Laboratory (ONDL), Department of Physics, National University of Singapore (NUS) between August 2009 and September 2013, and was supported by research scholarship from NUS.

It has been wonderful four years of research experience in this lab, through which I have learned a lot. Certainly the journey was not easy and it would not possibly be completed without great help from the following people.

First of all, I would like to thank my supervisor Dr. Peter HO together with Dr. Lay-Lay CHUA for guiding me into the field of organic electronics, teaching me how to do research and giving great help at all time with inspiring ideas and discussions.

Next, I would like to thank Dr. Li-Hong ZHAO for being my mentor in my first two years. From her I learned most of my research skills from basics of working in the lab to running experiments, and she was always helpful with my problems in the experiments. Also I would like to thank Dr. Jing-Mei ZHUO for providing guidance and great amount of help in my last two years.

Then I would like to thank Dr. Loke-Yuen WONG, Dr. Rui-Qi PNG, Dr. Bo LIU, Dr. Zhi-Li CHEN, Dr. Guan-Hui LIM, Dr. Jie SONG, Dagmawi, Kendra, Hu Chen, Jin Guo and all the other members of ONDL for their constant assistance and useful discussion through the entire time.

Last but not least, my gratitude also goes to Mr. Wang from SSL and Mr. Ong from Physics E lab for giving technical support in my UPS and AFM measurements.

I would like to acknowledge Dr. Jing-Mei ZHUO for providing P3HT FET data in Chapter 4 and Yong-Hui for P(NDI2OD-T2) FET data in Chapter 6, Dr. Jie-Cong TANG for synthesizing PBTTT-C14 material used in Chapter 5, Dr. Li-Hong ZHAO for providing PBTTT DSC data in Fig. 5.1, also Dr. R. Coehoorn for giving insightful discussion on charge transport physics in organic FETs.

Table of Contents

Declaration i

Acknowledgements iii

Abstract ix

List of Tables xiii

List of Figures xv

List of Symbols xxi

Chapter 1. Introduction 1

1.1 Basics of organic field-effect transistors 1

1.1.1 Organic semiconductors 1

1.1.2 Field-effect transistors 3

1.1.3 OFET applications 4

1.2 Current status of OFETs 5

1.2.1 Materials and processing 5

1.2.2 Issues with OFETs 8

1.3 Structure characterization 9

1.4 Charge transport physics in organic semiconductors 11

1.4.1 Electronic structure of organic semiconductors 11

1.4.2 Charge transport models in polymer semiconductors 13

1.5 Motivation 18

1.6 Outline 19

1.7 References 20

Chapter 2. Hopping charge transport in two-dimensional space 35

2.1 Introduction 36

2.2 Modification of hopping transport models to 2D 37

2.2.1 2D Vissenberg-Matters (VM) model 39

2.2.2 2D Martens model 41

2.3 Results and discussion 42

2.3.1 Mobility at zero carrier concentration limit 42

2.3.2 Carrier concentration dependent mobility 46
2.4 Conclusion 50
2.5 References 50

Chapter 3. Universal charge transport model for OFETs 53
3.1 Introduction 54
3.2 Model development 55
3.2.1 Density-of-states 55
3.2.2 Hopping sites 58
3.2.3 Intersite hopping rate 60
3.2.4 Intersite conductance and carrier mobility 61
3.3 Results and discussion 64
3.3.1 Variable-range hopping 64
3.3.2 Effect of distributed αd 66
3.3.3 Transport level 66
3.3.4 Significance of this approach 67
3.5 Conclusion 70
3.6 References 70

Chapter 4. Effect of dielectric surface on the transport DOS of rrP3HT 75
4.1 Introduction 76
4.2 Experiment 77
4.3 Results and discussion 79
4.3.1 Surface treatment induced difference in charge transport 79
4.3.2 Model validation: regioregular P3HT on C_{18}-alkylsilyated SiO_2 gate dielectric 81
4.3.3 Effect of dielectric surface on the transport DOS of rrP3HT 87
4.4 Conclusion 92
4.5 References 93

Chapter 5. Effect of molecular weight and processing in PBTTT OFETs 97
5.1 Introduction 99
5.2 Experiment 100

5.2.1 Material synthesis and thermal property 100
5.2.2 Atomic force microscopy (AFM) 102
5.2.3 FET measurement 104
5.3 Results and discussion 105
5.3.1 Molecular weight effect 106
5.3.2 Processing effect 111
5.4 Conclusion 115
5.5 References 116

Chapter 6. Charge transport in high electron mobility P(NDI2OD-T2) FETs 119
6.1 Introduction 120
6.2 Experiment 121
6.3 Results and discussion 123
6.3.1 π-band calculation 123
6.3.2 Transport DOS in donor-acceptor polymer 125
6.4 Conclusion 130
6.5 References 130

Chapter 7. Summary and outlook 135

Appendix A. Disorder broadened π-band edge fitting 137
Appendix B. FET mobility extraction 139
Appendix C. FET data fitting 143
Appendix D. Hopping transport in square lattice 145

Abstract

Although the hopping nature of transport of field-induced carriers in polymer field-effect transistors has been known for over two decades now, the quantitative description of field effect mobility-carrier density-temperature $\mu(c, T)$ surface over extended temperature and carrier density ranges starting from the density-of-states (DOS) picture has not yet been demonstrated. This impedes understanding of the role of disorder, which is a fundamental feature of transport in these materials, and also appreciation of the other mobility-limiting parameters. As a result, it is not yet possible to quantitatively model the entire field-effect mobility surface of organic materials. Here we show that $\mu(c, T)$ surface can be accurately described over a wide temperature and field-induced carrier density ranges using a basic variable-range hopping model with minimum number of fitting parameters. This model allows the transport DOS and interchain coupling parameter to be reliably extracted for the first time from a global simulation of the entire $\mu(c, T)$ surface to understand how molecular weight and its distribution, processing conditions, and/or the dielectric interfaces influence the DOS and hence the experimentally observed rich diversity of transport behavior for a number of important families of polymer semiconductors, including rrP3HT, PBTTT and P(NDI2OD-T2).

In chapter 1, we provide a brief introduction to the topic.

In chapter 2, we modify two existing hopping transport models, Vissenberg-Matters (VM) model and Martens model, into 2D with Gaussian DOS. The calculated $\mu(c, T)$ surfaces under 2D are similar for these two models. Both models break down at

relatively high carrier concentration region, as they predict the mobility rapidly drops with increasing carrier concentration.

In chapter 3, we develop an "universal" two-dimensional charge transport model for field-effect transistors which behaves correctly also at high carrier densities. We propose that the anisotropic transport along the polymer chain and in π-stacking direction could be modeled as hopping in a cross lattice in αR space with αR defined as the interchain coupling strength. This transport DOS at π-band edge could be modeled by simple analytical functions such as Gaussians or sum-of-Gaussians, or treated as a numerical function, and the site density N_t inside transport DOS is coupled to its width σ. Finally, the $\mu(c, T)$ surface is calculated using Miller-Abrahams (MA) hopping rate, resistor network approach and percolation method. We show that it is possible to simulate the entire $\mu(c, T)$ surface with only these three parameters: the transport DOS tail shape, the interchain coupling parameter and the connectivity parameter ξ which measures the macroscopic transport "connectivity" across the channel region,

In chapter 4, we employ rrP3HT bottom-gate bottom-contact FETs to validate the new charge transport model developed in Chapter 3 and to study the effect of dielectric surfaces on the transport DOS. By using a hemi-Gaussian transport DOS, the entire $\mu(c, T)$ surface of FET device with alkyl-SiO_2 surface treatment can be quantitatively reproduced with only DOS width, the interchain coupling and the connectivity parameter as fitting parameters. A temperature dependence of the transport DOS width is found in the simulation, which is verified by variable temperature UPS measurement. The other two dielectric surfaces i.e. the perfluoroalkyl- and TMS-SiO_2 give rise to a non-Gaussian tailing of the DOS and a depression of the connectivity parameter. The results are consistent with the generation of shallow traps from the co-

existence of a population of perturbed rrP3HT chain segments in the lying-down P3HT orientation.

In chapter 5, we study the effect of molecular weight and processing on charge transport in PBTTT-C14 top-gate bottom-contact OFETs, using four different molecular weights (MW) and three processing conditions. The PBTTT film morphology vary from long and partially fused ribbons at low MWs, through short ribbons, then to 2D terraces at high MWs, after same annealing to the liquid crystalline (LC) phase and slow cooling. Simulation of the $\mu(c, T)$ surfaces using the new hopping transport model reveals that the behavior of mobility, which increases with MW first then levels off, arises from a trade-off between transport DOS tail width and microstructural connectivity, while interchain coupling is more or less constant. The evolution of the transport DOS tail width and microstructural connectivity parameters show mimic the earlier trend.

In chapter 6, we study the charge transport in a high electron mobility donor-acceptor polymer P(NDI2OD-T2) with top-gate bottom-contact FET devices, which show mobility ~ 0.1 $cm^2 V^{-1} s^{-1}$ at room temperature. The extracted $\mu(c, T)$ surface shows much narrower mobility spread when charge carrier density increases, along with similar activation energy to that of rrP3HT and PBTTT. The narrow spread is attributed to a narrow transport DOS of P(NDI2OD-T2). This narrow transport DOS width is the primary reason for the high electron mobility in P(NDI2OD-T2) despite its slightly worse interchain coupling and intermediate connectivity compared to rrP3HT and PBTTT.

List of Tables

Table 2.1 The fitted p_0, a and b and the theoretical p_0 for both 2D VM and Martens models at different site densities. 46

Table 4.1 Connectivity parameter ξ for rrP3HT OFET devices with the three different surface treatments. 92

Table 5.1 Summary of molecular weights, mobility at 295 K and fitting parameters for the PBTTT-C14 TGBC FET devices. 115

Table 7.1 Summary of extracted parameters for all materials and experiment conditions studied in this thesis. 136

List of Figures

Figure 1.1 (a) Formation of π/π^* orbital by p_z orbital overlapping in a single small molecule or polymer chain segment. (b) Overlapping of HOMO/LUMO orbital to form HOMO/LUMO band in ethylene as an example for single crystals.[10] 2

Figure 1.2 (a) Commonly used FET device structures. (b) Example $I-V$ curves of an OFET. 4

Figure 1.3 (a) OTFT active matrix backplane coupled with E-Ink. Photography courtesy of Plastic Logic. (b) First printed polymer RFID tag (13.56 MHz). PolyIC press picture. (c) Microprocessor foils: leftmost foils each have two microprocessors; each processor contains 3381 plastic transistors. Picture from IMEC.[22] (d) The world's lightest and thinnest flexible sensor. Picture from Someya-Sekitani Group, University of Tokyo........ 5

Figure 1.4 Chemical structures of some high mobility solution-processable organic semiconductors. Structures are taken from literature.[29-34] 6

Figure 1.5 Illustration of the charge transport process in the disorder model. 14

Figure 1.6 Illustration of the charge transport process in the mobility edge model...... 18

Figure 2.1 Calculated zero-concentration limit reduced mobility $\mu_{red}(0)$ results. (a) $\mu_{red}(0)$ by 2D Vissenberg-Matters (VM) model and 2D Martens model with Gaussian Density of States (DOS) at different N_t/α^2. (b) $\mu_{red}(0)$ by 2D and 3D VM models with Gaussian DOS, under same inter-site distance (assuming same α in 2D and 3D). 44

Figure 2.2 Calculated critical hopping distance R^* in unit of average inter-site distance under different N_t/α^2 by 2D Martens model with Gaussian DOS. (Assuming same α) 45

Figure 2.3 Calculated carrier concentration (f) dependent reduced mobility $\mu_{red}(f)$ results. (a) $\mu_{red}(f)$ by 2D VM model and 2D Martens model with Gaussian DOS and $N_t/\alpha^2 = 10^{-2}$. (b) $\mu_{red}(f)$ by 2D and 3D VM models with Gaussian DOS and $N_t/\alpha^2 = 10^{-2}$ for 2D, $N_t/\alpha^3 = 10^{-3}$ for 3D respectively. 47

Figure 2.4 Calculated $R*$ and $E*$ at different Fermi levels (different carrier concentrations) by 2D Martens model with Gaussian DOS. (a)&(b) $R*$ in unit of average intersite distance and $E*$ in unit of DOS width respectively at $N_t/\alpha^2 = 10^{-2}$. (c) Ratio of $R*$ to its value at zero-concentration limit $R*(0)$ at different N_t/α^2. (d) Ratio of $E*$ to its value at zero-concentration limit $E*(0)$ at different N_t/α^2...48

Figure 2.5 Comparison of $\mu_{red}(f)$ calculated by 2D VM model and by Eqn. 2.11 respectively with Gaussian DOS. (a) $\mu_{red}(f)$ at $N_t/\alpha^2 = 10^{-2}$, $a = 0.566$ and $b = 0.485$ used in the equation. (b) $\mu_{red}(f)$ at $f = 10^{-1}$, a and b are taken from Table 2.1 for corresponding N_t/α^2..49

Figure 3.1 Transport Density of States (tDOS) in polymer semiconductors. (a) Calculated π-band for oligothiophene with 8, 12 and 16 thiophene units, indicated by area under curve (excluding sulfur peak). (b) Edge of rrP3HT π-band (pink shaded area) measured by UPS. (c) Convolution of uniform DOS (height h_0) with Gaussian disorder σ_{dis} gives broadened tail at the edge, which is well fitted by single Gaussian with $\sigma = 1.13\sigma_{dis}$ and peak height $A = 0.913h_0$. (d) Illustration of π-band (green region under curve) with width E_0, and the transport DOS (pink region) at π-band edge. 57

Figure 3.2 Hopping transport in a cross lattice (αR space) in polymer semiconductors. (a) A simplified view of polymer chains (green) and hopping sites (red) in the π-aggregation, longer interval between sites along the polymer chain comes from longer delocalization length of π electron wavefunction in that direction. (b) Illustration of stronger inter-site coupling in the intrachain hopping paths k_{intra} than in interchain hopping paths k_{inter}, The coupling strength is represented by peak numbers. (c) The basic picture of hopping transport in αR space, in which transport sites form square lattice. Only hops along the polymer chain and in the π-stacking directions are allowed as indicated by hopping paths k_1, k_2 59

Figure 3.3 Variable-range hopping in polymer semiconductors. (a) Illustration of hopping to n^{th} neighbors in αR space. (b) Uniform distribution of αd in Miller-Abrahams hopping rate equation, d is the π-stacking distance. (c) Distribution of reduced conductance G_{ij}' to n^{th} neighbor at 295 K and 77 K under Gaussian DOS with $\sigma = 90$ meV and αd distribution with $\langle\alpha d\rangle = 0.85$ and $\alpha_w = 0.06$. The reduced conductance G_c' of the resistor network is determined by using bond percolation number $B_c = 2$. 65

Figure 3.4 Calculated Fermi level (E_F), Activation energy (E_A) of mobility and Transport level (E_T) at different carrier concentrations ($f = 2 - 20\%$, interval 2%) with Gaussian DOS (width σ) and $\langle\alpha d\rangle = 1.0$. 67

Figure 3.5 Calculated reduced mobility μ' with Gaussian DOS. 69

Figure 4.1 Schematic of BGBC FET structure, top to bottom: semiconductor (red), source-drain contacts (yellow), SiO_2 dielectric with surface treatment (white) and *p*-doped silicon gate (grey). The structure of rrP3HT is shown together with the three surface treatments on SiO_2. 78

Figure 4.2 Measured $\mu(c, T)$ surfaces for rrP3HT BGBC FET devices with three different surface treatments. 80

Figure 4.3 Fitting result for rrP3HT OFET with alkyl-SiO_2 dielectric. (a) Comparison of experimental and simulated $\mu(c, T)$ surfaces. (b) Transport DOS width narrowing with temperature decreasing. 82

Figure 4.4 Variable temperature UPS measurement result of rrP3HT film. (a) HOMO edge narrowing with temperature decreasing. (b) HOMO edge can be fitted well with a single Gaussian function. Extracted Gaussian width (red dots) decreases with temperature, the trend is illustrated by the blue curve. 84

Figure 4.5 The transport DOS of rrP3HT OFET with alkyl-SiO_2 dielectric at 295 K and 77 K, together with the transport levels (E_T) and Fermi levels (E_F) for high and low carrier densities. 85

Figure 4.6 The activation energy (E_A) of mobility for rrP3HT BGBC devices with different surface treatments on SiO_2. O_2-plasma: oxygen plasma treated SiO_2 dielectric; OTS: alkyl-SiO_2 dielectric; PDS: perfluoroalkyl-SiO_2 dielectric; HMDS: TMS-SiO_2 dielectric. 88

Figure 4.7 Fitting results for rrP3HT OFET devices with (a) perfluoroalkyl-SiO_2 dielectric and (b) TMS-SiO_2 dielectric. 91

Figure 4.8 Transport DOS at 295 K for rrP3HT OFET devices with the three different surface treatments. 92

Figure 5.1 (a) Chemical structure of PBTTT-C14. (b) Phase transition temperatures for PBTTT-C14 with different molecular weights (MWs). (Data from Lihong) 102

Figure 5.2 AFM pictures of different MWs PBTTT-C14 films under different annealing conditions: (**A**) Annealed at temperatures below nematic phase, annealing temperatures are $T_k - 10$K (P22) or $T_k'' - 10$K (P11−P3), quench cooled down; (**B**) Annealed at nematic phase, annealing temperatures are $T_k +$

10K (P22) or $T_k'' + 10$K (P11−P3), quench cooled down; (**C**) Annealed at nematic phase, same annealing temperatures as (B) but slow cooled down at 0.1 K/min. 103

Figure 5.3 (a) Structure of the top-gate bottom-contact (TGBC) FET on the left, chemical structure of AF2400 on the right. (b) Fitting results for PBTTT-C14 TGBC FET devices with different MWs and processed with annealing condition C. 107

Figure 5.4 Extracted transport DOS at 295 K for PBTTT-C14 TGBC FET devices with different MWs and processed with annealing condition C. 108

Figure 5.5 Fitting parameters for PBTTT-C14 TGBC FET devices with different MWs and processed with annealing condition C. (a) Mobility of the four devices under room temperature at highest carrier density. (b)-(d) Coupling parameter, connectivity parameter and DOS width at 295 K respectively. Error in the fitting parameters indicated in the plot for P6 device. 108

Figure 5.6 Fitting results for PBTTT-C14 TGBC FET devices with lowest MW (P3) and processed with different annealing conditions. 112

Figure 5.7 Fitting parameters for PBTTT-C14 TGBC FET devices with lowest MW (P3) and processed with different annealing conditions. (a) Transport DOS at 295 K. (b1) Mobility of the three devices under room temperature at the highest carrier density. (b2)-(b4) Coupling parameter, connectivity parameter and DOS width at 295 K respectively. 114

Figure 6.1 (a) Chemical structure of P(NDI2OD-T2). b) Structure of dielectric polymers. From top to bottom: PS, PMMA, CYTOP. c) BGTC FET device structure 121

Figure 6.2 (a) π band structure of (T-NDI-T)$_x$ unit, x = 1, 2, 3. (b) π band width for x = 1 − 3. (c) Energy levels of four molecular orbital for four molecular structures, from left to right: thiophone (T), 6-thiophene (6T), NDI, T-NDI-T. From top to bottom: highest π^* orbital, LUMO, HOMO, lowest π orbital............... 124

Figure 6.3 Fitting results for P(NDI2OD-T2) TGBC FET With CYTOP dielectric. a) Experimental and simulated $\mu(c, T)$ surface. b) Transport DOS width change with temperature in simulation. c) & d) Transport DOS together with transport level (E_T)and Fermi level (E_F) for c = 1.9 x 10^{12} cm^{-2} for CYTOP-gated device at 295 K and 113 K respectively. 127

Figure 6.4 Fitting results for P(NDI2OD-T2) TGBC FET With PS dielectric. (a) Experimental and simulated $\mu(c, T)$ surface. (b) Transport DOS width change with temperature in simulation. (c) & (d) Transport DOS together with transport level (E_T)and Fermi level (E_F) for c = 1.8 x 10^{12} cm^{-2} for PS-gated device at 295 K and 113 K respectively. 129

Figure A.1 Convolution of uniform DOS (width 10 eV) with Gaussian disorder (width σ_{dis}). (a) Broadening at the edge after convolution compared to the uniform DOS (black line). (b) The parameters of the single Gaussian function that can best fit the broadened DOS tail. From top to bottom: peak height normalized to uniform DOS height, width, Difference of the original DOS edge (5 eV) with its center location, normalized by σ_{dis}. 137

Figure B.1 (a) Example of threshold voltage extraction at source-drain contact. Data from rrP3HT BGBC FET device with alkyl-SiO_2 dielectric. (b) Example of threshold voltage extraction in gate bias V_{gs}. Data from P(NDI2OD-T2) TGBC FET device with CYTOP dielectric. 140

Figure B.2 (a) $\mu(c, T)$ surface plotted as $\mu(c)$ curves at different temperatures. (b) $\mu(c, T)$ surface plotted by $\mu(T)$ curves at different carrier densities, which is used for fitting. Data from rrP3HT BGBC FET device with alkyl-SiO_2 dielectric. 141

Figure C.1 (a) $\Delta 1$ − $\Delta 4$ defined by the four (c,T) points. (b) Calculated $\Delta 1$ − $\Delta 4$ for rrP3HT BGBC FET device with alkyl-SiO_2 dielectric, using Gaussian DOS (fixed width σ) under conditions: c_{high} and c_{low} = 6.0 x 10^{12} and 1.7 x 10^{12} cm^{-2}, T_{high} and T_{low} = 295 and 77 K. Grey lines give the allowed carrier concentration for this device at each σ, which comes from the coupling between carrier concentration and σ. 144

Figure D.1 In square lattice, (a) the number of neighbors $N(R)$ at distance R (R is normalized by lattice constant d), (b) total number of neighbors $\Sigma N(R)$ within distance R. 145

Figure D.2 Variable-range hopping in square lattice. (a) Illustration of hopping to neighbors at different distances in R space. (b) Uniform distribution of αd. (c) Distribution of reduced conductance G_{ij}' for hopping paths to neighbor sites *a*, b and c at 295 K and 77 K with Gaussian DOS (σ = 90 meV) and a uniform distribution (<α> = 0.85 and α_w = 0.06). The reduced conductance G_c' of the resistor network is determined by using bond percolation number $B_c = 2$. 146

Figure D.3 Calculated reduced mobility μ' in square lattice with Gaussian DOS. 146

Figure D.4 Calculated Activation energy (E_A) of mobility and Transport levels (E_T) at different carrier concentrations (f = 2 – 20 %, interval 2 %) with Gaussian DOS (width σ) and $<\alpha d> = 1.0$ in square lattice. 147

Figure D.5 Fitting result for rrP3HT OFET with alkyl-SiO_2 dielectric in square lattice (a) Comparison of experimental and simulated $\mu(c, T)$ surfaces, $\sigma = 100$ meV at 295 K and 80 meV at 77 K, $<\alpha d> = 0.85$, $\xi = 0.36$. (b) Transport DOS width narrowing with temperature decreasing. (c) The transport DOS at 295 K and 77 K, together with the transport levels (E_T) and Fermi levels (E_F) for high and low carrier densities...148

List of Symbols

α	inverse of wave function delocalization length
B_c	bond percolation number
c	carrier density
d	π-stacking distance
ε	site energy
E_A	activation energy
E_T	transport energy
E_F	Fermi level
f	carrier concentration
G	conductance
k_B	Boltzmann constant
μ	mobility or chemical potential
μ' or μ_{red}	reduced mobility
N_0	π-orbital density
N_t	Transport site density
σ	Gaussian transport DOS width or conductivity
ν_0	attempt hopping frequency
w	hopping frequency
ξ	connectivity parameter

Chapter 1. Introduction

1.1 Basics of organic field-effect transistors

1.1.1 Organic semiconductors

Organic semiconductors have been of great interest to both research community and industry since 1980s, when it was demonstrated that the electric and opto-electric properties of undoped organic materials can be used for electronic devices which are organic field-effect transistors (OFETs)[1-3], organic light-emitting diodes (OLEDs)[4,5] and organic photovoltaics (OPVs)[6] and etc. Up until now, OLEDs have been widely used in real products such as OLED TVs and lightings;[7] OFETs are very near to large range application in display backpanel and organic circuits;[8] and OPVs are in rapid developing progress to reach high enough efficiency.[9]

The advantages of organic semiconductors mainly come from their ability to be rather easily processed compared to silicon, especially for polymers and some small molecules that can be processed in solution. The simple processing step makes it possible to fabricate organic devices at low cost on large area, flexible and transparent plastic substrates. Besides, the material properties of organic semiconductors can be tuned in a large range by adjusting their chemical structures.

The semiconducting property of organic materials comes from the p_z orbital overlapping, which results in orbital splitting to form delocalized π/π^* orbital in π/π^* bands with bandgap between HOMO (highest occupied molecular orbital) and LUMO (lowest unoccupied molecular orbital) for a single molecule or polymer chain segment, as shown in Fig. 1.1a. In organic single crystals, the HOMO and LUMO orbital further overlap to form HOMO and LUMO bands with narrower bandgap, as shown in Fig.

1.1b. The overlapping between organic molecules is generally weak, as a result the bandwidth of HOMO and LUMO bands is normally only around several hundred meV.[10] So for single crystal, the charge transport is band transport which is characterized by mobility decreasing with increasing temperature.[11] However, this band transport mechanism is still controversy as the observed band transport behavior could also be because mobility is limited by thermally induced disorder.[12] In polymer semiconductors, there exists strong disorder which localizes charge carriers. The charge transport is usually described by the trap-and-release model[13] or hopping transport models[14] depending on the degree of disorder.[15,16]

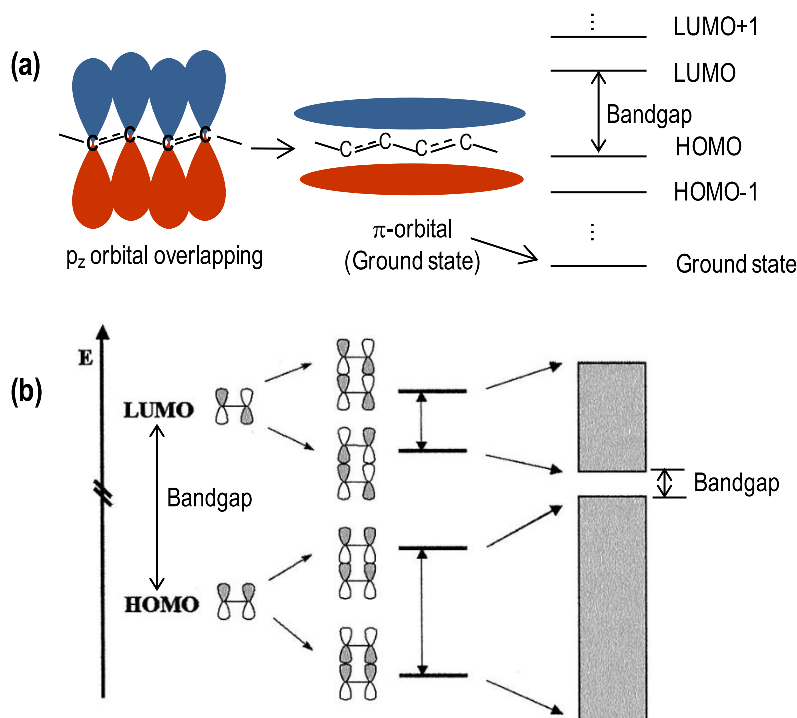

Figure 1.1 (a) Formation of π/π^* orbital by p_z orbital overlapping in a single small molecule or polymer chain segment. (b) Overlapping of HOMO/LUMO orbital to form HOMO/LUMO band in ethylene as an example for single crystals.[10]

1.1.2 Field-effect transistors

The first practical field-effect transistor (FET) was invented by Shockley in 1947 and the modern metal-oxide-insulator (MOS) FET was invented in 1960, the commonly used structure of which is shown in Fig. 1.2a, including bottom-gate top-contact (BGTC), bottom-gate bottom-contact (BGBC) and top-gate bottom-contact (TGBC). The FET is a three-terminal device, in which gate bias (V_{gs}) controls the carrier density in the semiconductor channel between source/drain contacts by capacitor effect while source/drain bias (V_{sd}) controls the current across the channel.

When V_{gs} is large compared to V_{sd}, the device is in the linear regime where the carrier density across the channel is nearly constant and source-drain current (I_{sd}) increases linearly with V_{sd}. When V_{gs} is smaller than V_{sd}, the device is in the saturation regime. The carrier density gradually decrease from source contact to the point in the channel where $V_{gs} = V_{sd}$. The large resistance of the region between that point to drain contact causes I_{sd} to saturate and do not further increase with V_{sd}. The $I-V$ characteristics of FET in linear and saturation regimes are described by:

$$\begin{aligned} I_{sd,lin} &= \mu_{lin} C \frac{W}{L} [(V_{gs} - V_{th}) V_{sd} - \frac{{V_{sd}}^2}{2}] \\ I_{sd,sat} &= \mu_{sat} \frac{CW}{2L} (V_{gs} - V_{th})^2 \end{aligned} \tag{1.1}$$

Where μ_{lin} and μ_{sat} is the charge carrier mobility in the linear and saturation regime respectively, C is the capacitance of dielectric layer, W and L is channel width and length respectively, V_{th} is the threshold voltage in gate bias, only when V_{gs} is larger than V_{th} charge carriers start to accumulate in the channel, the source contact is

assumed to biased at 0 ($V_s = 0\ V$). An example of the $I-V$ curves is shown in Fig. 1.2b.

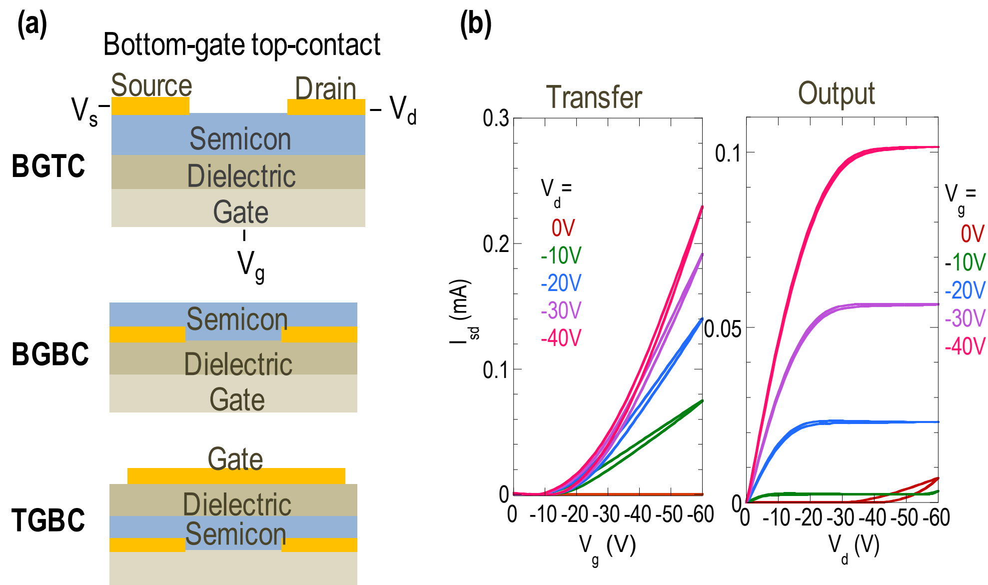

Figure 1.2 (a) Commonly used FET device structures. (b) Example $I-V$ curves of an OFET.

FET Performance is normally characterized by several parameters such as charge carrier mobility, current on/off ratio, gate leakage current, gate threshold voltage, sub-threshold slope (S) and device stability etc.

1.1.3 OFET applications

With rapidly improving performance, OFETs show great application potential in display backpanels, organic circuits and sensors.[8,17,18] In display backpanels, the OFET matrix controls the on/off of the lighting pixels in e-ink displays[19] and liquid crystal displays (LCDs) or directly supply current to the light-emitting pixel in OLED displays which has much higher mobility requirement for the OFETs.[8,20] Organic circuits such as radio frequency identification tag (RFID)[21] and an even more complicated microprocessor[22] have been demonstrated. Also very flexible and stretchable sensor matrix with OFETs

has been demonstrated, which can be used as e-skin etc.[23-25] Examples of latest applications are shown in Fig. 1.3.

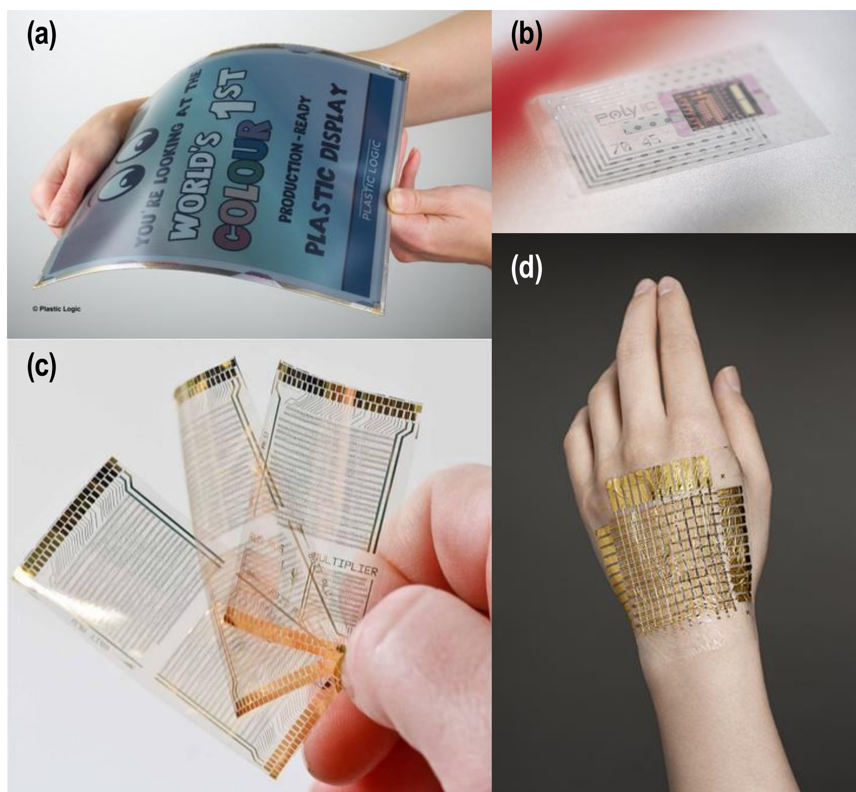

Figure 1.3 (a) OTFT active matrix backplane coupled with E-Ink. Photography courtesy of Plastic Logic. (b) First printed polymer RFID tag (13.56 MHz). PolyIC press picture. (c) Microprocessor foils: leftmost foils each have two microprocessors; each processor contains 3381 plastic transistors. Picture from IMEC.[22] (d) The world's lightest and thinnest flexible sensor. Picture from Someya-Sekitani Group, University of Tokyo.

1.2 Current status of OFETs

1.2.1 Materials and processing

The field-effect mobility of organic semiconductors has greatly improved over the past 30 years.[26-28] Currently for both polymers and small molecules, the reported mobility is constantly above that of α-Silicon (0.5 – 1 cm^2 V^{-1} s^{-1}), which is used as a benchmark

for application requirement. The chemical structures of some commonly used high mobility materials are given in Fig. 1.4.

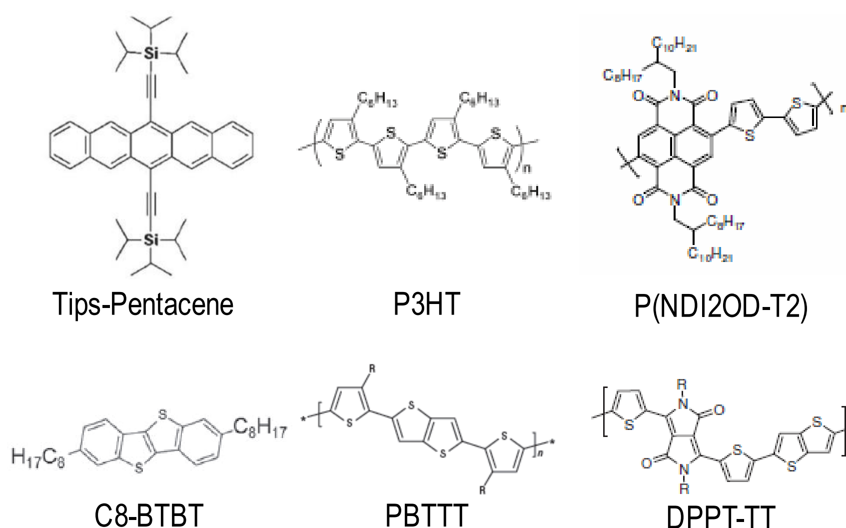

Figure 1.4 Chemical structures of some high mobility solution-processable organic semiconductors. Structures are taken from literature.[29-34]

For solution-processable small molecules, the commonly used materials are Tips-Pentacene and its derivatives[35,36], thienoacene family[37] and NDI/PDI (naphthalene/ perylene diimide) families (*n*-type)[36]. The highest mobility of Tips-Pentacene is reported to be 4.6 $cm^2 V^{-1} s^{-1}$ by using solution shear method.[38] In the thienoacene family, C10-DNTT transistors array can reach average mobility of 7 $cm^2 V^{-1} s^{-1}$ by using oriented growth method;[30] while ink-jet printed C8-BTBT transistors array shows average mobility as high as 16.4 $cm^2 V^{-1} s^{-1}$ with the maximum value at 31.3 $cm^2 V^{-1} s^{-1}$.[39]

For polymers, the commonly used materials are P3HT[40], PBTTT[32,41] and recently reported high mobility donor-acceptor polymers[42] such as CDT-BTZ[43], IDT-BT[44], DPP series[27,34] and P(NDI2OD-T2)[33] (*n*-type). The highest hole and electron mobility of unaligned films is reported to be around 12 $cm^2 V^{-1} s^{-1}$ for P-29-DPPDTSE[45] and 6.3 $cm^2 V^{-1} s^{-1}$ for PDBPyBT[46] respectively. With alignment, the average mobility of

PCDTPT at certain molecular weight is reported to be as high as 16.4 $cm^2 V^{-1} s^{-1}$ with the maximum value at 23.7 $cm^2 V^{-1} s^{-1}$.[47] Together with the high mobility, the polymers in some cases can also show ambipolar charge transport behavior with balanced hole and electron mobility,[48-50] which is useful for application in complementary circuits.

The processing conditions of the semiconductor materials during FET devices fabrication can greatly affect the device performance,[51,52] which is evident from the above description that the highest mobility generally is reached under certain processing conditions. The microstructure/morphology of the semiconductor films can be affected by factors such as solvents,[53] deposition methods,[54] annealing conditions after deposition[55] etc during fabrication, among which the deposition methods is most important. To reach high mobility, the deposition process is carefully controlled in order for the semiconductor films to form highly ordered structure for solution-processable small molecules and highly orientated polymer chains for polymers. For the solution-processable small molecules, the ordered structure is generally achieved by controlled drying of the solution from one end to the other end to get directional crystallization.[30,38] For the polymers, the charge transport process along the polymer backbone is the fastest at the microscope level, compared to that in the π-π stacking direction or in the alkyl direction. There are basically two kinds of methods to align the polymer chains to achieve anisotropic charge transport at the macroscopic level with possibly high charge transport mobility in the direction parallel to the polymer chains. One is to use the same principle of directional growth by controlled drying as for small molecules, examples include flow-coating method,[56] zone-casting method,[57] temperature gradient method[58] etc. The other one is to use pre-defined structure to control polymer orientations to achieve alignment, the methods to create the pre-defined structure are rubbing polyimide film,[59] imprinting,[60] scratching SiO_2[47] etc.

Besides the semiconductor materials, gate dielectric also plays a very important role in determining device performance.[61,62] The charge carrier mobility is reported to decrease when gate dielectric constant (k) goes high,[63-65] which is explained as a result of semiconductor DOS broadening near the high-k dielectric.[66,67] This effect is less obvious for polymers with long alkyl chains,[33] which separate the polymer backbone from the semiconductor-dielectric interface by a large distance and thus greatly suppresses this broadening effect. The chemical groups of the gate dielectric can act as hole/electron traps so that generally polymer semiconductors only show *p*- or *n*-type behavior. By choosing proper gate dielectric and right processing conditions, the polymer semiconductors can show ambipolar charge transport behavior with balanced hole and electron mobility,[48,68-70] especially for recently reported donor-acceptor polymers.[49,50] The choice of dielectric in bottom gate FET device is more important than in top gate FET device, as the microstructure of the semiconductor film at the bottom interface is strongly affected by the underlying dielectric,[71] as a result the device performance can vary in several orders of magnitude with different dielectric/surface treatments,[71,72] the mobility affecting factors include surface energy[73], surface roughness[74] etc.

1.2.2 Issues with OFETs

Apart from requirement on the charge carrier mobility, which has already been fulfilled for many applications, there are some other problems needed to be. First, the currently demonstrated device bias is too high compared to α-Si device. This is because of high threshold voltage in gate bias (V_{gs}) and also high carrier density (thus high V_{gs}) in order to get good mobility. In order to lower down the device bias,

several methods are demonstrated such as using high-k materials as gate dielectric,[62,75] reducing gate dielectric thickness by using crosslinked polymer dielectrics[76,77] or self-assembled monolayers (SAMs) as gate dielectric[78,79], using polyelectrolytes as gate dielectric[80,81] etc. Second, the high contact resistance (R_c) at the source or drain/semiconductor contacts becomes a serious problem for high field-effect mobility device,[82,83] in which a large part of the source-drain bias (V_{sd}) will be lost at the metal/semiconductor contacts therefore the devices are contact limited. The common methods to solve this contact resistance problem are: varying metal electrode to match energy levels of semiconductors,[84] using thiol-based SAMs on metal electrodes to control the interface dipole,[85] using charge injection layer between metal/semiconductor,[86] using carbon based electrodes[87] etc. Third, OFETs generally have stability issue under longtime operation during which $V_{gs,th}$ increases overtime.[88] The cause of the bias stress effect is not understood clearly, the presence of water is likely to be one main reason[89] while other possible mechanisms are under investigation.[90]

1.3 Structure characterization

Polymer semiconductors generally have complex film structures as a result of their disordered nature; nevertheless it is import to study the molecule packing structures in the film especially at the semiconductor-dielectric interface since these packing structures determine the electronic structures of the semiconductor in the microscopic level and thus the electric properties of the device at the macroscopic level such as charge carrier mobility etc. The common characterization techniques include probe methods (AFM, KPFM etc.), scattering methods (XRD, TEM etc.) and absorption

methods (UV-Vis, Ellipsometry, NEXAFS etc.), there are also some other useful techniques but they are relatively complex and not widely used (2D-NMR etc.).[43,91-93]

The most common probe method is AFM, which is used to study the surface morphology of semiconductor films. For region-regular P3HT (rrP3HT), low molecular weight (MW) films show a highly ordered, nanorod-like surface structure, while high MW films show less ordered, isotropic nodule film morphology.[94] For PBTTT films, when annealed above its liquid crystal transition temperature, low MW films show nanorod-like film morphology similar to rrP3HT, high MW films show terrace-like morphology with step height same as PBTTT molecule height in the alkyl direction, indicating PBTTT molecules form edge-on in-plane π-stacking.[95] For the donor-acceptor polymers, the film morphology generally shows isotropic or amorphous structure.[33,34]

The most common scattering method is XRD and normally GIXRD (Grazing incidence X-ray diffraction) is used to study the periodic structures in the film because of its small penetration depth which is suitable for thin film study. From GIXRD results one can get some basic information on molecule packing such as π-stacking distance, face-on/edge-on orientation etc. The π-stacking distance for polymer semiconductors is usually around 3.6-3.9 Å.[34,40,55,96,97] The XRD results of rrP3HT and PBTTT films show that their molecules usually adopt edge-on orientation to form in-plane π-stacking.[40,55] For P(NDI2OD-T2), the molecules generally have face-on orientation but it can transit to edge-on orientation under thermal annealing, without causing loss of performance.[96,98,99] Detailed study of the XRD results reveals large disorder in π-stacking direction for PBTTT and P(NDI2OD-T2), the position disorder of the molecules is around $10 - 20\%$ of the π-stacking distance.[93,100] Another useful

scattering method is TEM, which is used to get domain sizes in polymer semiconductor films, The domain size in PBTTT-C14 film is determined to be around ~600 nm, smaller than that measured by AFM.[101]

In the absorption methods, polarized Visible, IR light are used to measure the dichroic ratio of the film or polarized X-ray is used to measure the average molecular orientation angles in the film. This NEXAFS technique is surface sensitive and very useful for OFET study since the charge transport happens at only the first or two monolayers in the polymer film. It is straightforward to measure the top surface of the polymer film, while the buried bottom surface of the polymer film can be studied by peeling off the film from low surface energy substrates.[96,97,102] The measurements for common polymers show that P3HT film at the bottom interface was considerably more disordered than in the bulk and had a large fraction of molecules with face-on orientation;[103] PBTTT molecules form edge-on in-plane π-stacking, the conjugated planes tilt about 21° and the alkyl chains tilt about 45° away from substrate normal;[104] for P(NDI2OD-T2) the molecules at the bottom interface tend to adopt face-on orientation compared to those at top surface.[96]

1.4 Charge transport physics in organic semiconductors

1.4.1 Electronic structure of organic semiconductors

The electronic structure of organic semiconductors determines its electrical property and generally can be calculated by tight-binding model.[15] In tight-binding model, the wavefunction of delocalized molecular orbital in the system is calculated based on wavefunction of localized orbital on individual molecules/polymer chain segments

(sites). The model requires several inputs which are the fundamental parameters describing the material properties.[10,15] First the site energy ε of the localized orbital, the disorder in the system will cause the energy to spread and its distribution form the density of states (DOS). Then in organic semiconductors charge carriers will induce molecular geometry change called polaron, which will change the site energy by electron-phonon coupling – diagonal disorder. The coupling strength λ relates to the reorganization energy of the molecule. Also the overlapping strength between orbital is given by the transfer integral t, which will be modulated by lattice vibration and called off-diagonal disorder whose strength is given by parameter α.[105]

The polaron can be observed in CMS (charge modulation spectroscopy) experiments. Its presence introduces new energy levels in the bandgap as shown by quantum calculations[106,107] and thus induces new absorption bands mostly in the visible light region, the intensity of this absorption is only 10^{-4} of the absorption between HOMO and LUMO under normal device bias conditions. Nevertheless, the effect can be clearly observed by bias modulation together with lock-in technique.[40,67,108,109]

The tight-binding model was applied on single polyethylene chain to calculate its band structure and the result shows the existence of soliton on polymer chain.[110-112] The electronic structure of 1D stack of Pentacene molecules shows that the wavefunction is localized by the off-diagonal disorder, so the charge transport in Pentacene might be thermal induced disordered limited rather than band transport as thought previously.[105] An even larger system containing 12 or 24 P3HT chains were also calculated recently. The results show that charge carriers are mostly localized on the polymer chains and the DOS tail is greatly modulated by material properties such as regioregularity etc.[113,114]

1.4.2 Charge transport models in polymer semiconductors

Disorder plays an essential role of determining the electronic structure hence the charge transport in organic semiconductors, even in polycrystalline films of small molecules as shown by important studies with Pentacene.[115-119] In polycrystalline Pentacene films with large crystalline domain size (up to μm), the apparent field effect mobility inside the domain is only ~ 1 $cm^2\ V^{-1}\ s^{-1}$, which is one order lower than that of its single crystal, and it is independent of the domain sizes.[117] GIXRD reveals the existence of small crystallites (25 − 50 nm) inside the domain, which causes HOMO level fluctuation across the domain with root of mean square amplitude of just 10 meV as measured by atomic force microscope potentiometry (AFMP).[117,119] The small fluctuation i.e. disorder results in the low mobility inside the domain, while charge transport is further limited by the domain boundaries as well as other factors e.g. metal/semiconductor contacts, metal induced damages etc in Pentacene OFET devices.[117] This shows the importance of disorder in charge transport study in organic semiconductors. For polymer semiconductor films that are generally more disordered, there are currently two types of charge transport models, the disorder model and the mobility edge model, differing in their emphasis of disorder as the primary or secondary feature respectively.[13,14]

Disorder models In disorder models, charge carriers are localized on individual sites with site energy ε, and they can make variable range hop to neighboring sites with assistant of thermal energy.[115] The site energy is usually assumed to be not correlated to each other while in some models; the correlation is taken into account. When not correlated, the site energy distribution i.e. the Density of States (DOS) is generally assumed to be Gaussian or in sometimes exponential. Inside the DOS, the charge

carriers occupy the energy levels according to Fermi-Dirac statistics, as shown in Fig. 1.5.

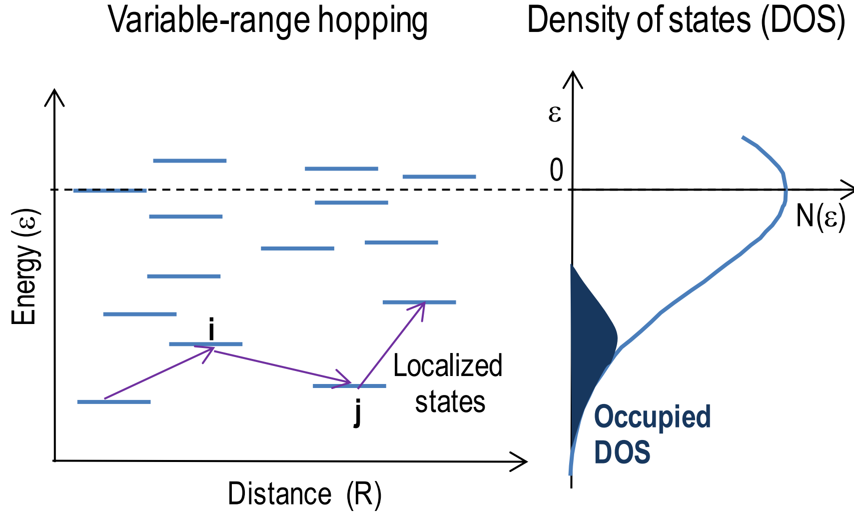

Figure 1.5 Illustration of the charge transport process in the disorder model.

There are two hopping rate equations that are commonly used in disordered models. One is the Miller-Abrahams (MA) hopping rate equation,[116] which is valid for weak electron-phonon coupling and at low temperature. The equation is given by:

$$w_{ij} = \begin{cases} \nu_0 \exp(-2\alpha R_{ij} - \dfrac{\varepsilon_i - \varepsilon_j}{k_B T}) & \varepsilon_j < \varepsilon_i \\ \nu_0 \exp(-2\alpha R_{ij}) & \varepsilon_j \geq \varepsilon_i \end{cases} \tag{1.2}$$

where w_{ij} is the hopping rate from site j to i, ν_0 is the attempt frequency, R_{ij} is the distance between sites i and j, ε_i and ε_j are the site energies whose values are taken from the DOS distribution, α is the electronic coupling parameter which is described as the inverse of the delocalize length of the wavefunction when carriers occupy the site. In the presence of external electric field E, site energy needs to include the coulomb energy of the carrier in the electric field. The hopping rate is different for upward and downward hopping.

The other one is the semi-classical electron transfer rate developed by Marcus et al.,[117] which is valid for strong electron-phonon coupling and at high temperature. After taking into account the effect of off-diagonal disorder by assuming the transfer integral follows an exponential decay $t = t_0 exp(-\alpha R_{ij})$, the equation is given by:

$$w_{ij} = \frac{t_0}{\hbar}\left(\frac{\pi}{\lambda_{reorg} k_B T}\right)^{1/2} \exp\left(-2\alpha R_{ij} - \frac{(\lambda_{reorg} + \varepsilon_i - \varepsilon_j)^2}{4\lambda_{reorg} k_B T}\right) \quad (1.3)$$

Where w_{ij} is the hopping rate from site j to i, t_0 is a constant transfer integral, λ_{reorg} is the molecular reorganization energy during charge transfer; other parameters have the same meaning as above. We can see the hopping rate is same for upward and downward direction in energy. The value of λ_{reorg} can be obtained from quantum calculation.

Bässler et al.[118] first developed the Gaussian disorder model (GDM) with Gaussian DOS and MA hopping rate to study the hopping charge transport at low carrier concentration limit by Monte-Carlo method. The site energy is not correlated and the off-diagonal disorder term α is assumed to follow a Gaussian distribution with standard deviation Σ. The simulation results show that the energy distribution of charge carriers relaxes into a Gaussian distribution centered at $-\sigma\hat{s}$, where σ is the Gaussian DOS width and $\hat{s} = \sigma / k_B T$. The mobility shows temperature dependence $\mu(T) \sim exp(-4\hat{s}^2/9)$ which suggests charge transport can be viewed simply as charge carriers hopping from energy level at $-\sigma\hat{s}$ to the transport level at the center of Gaussian DOS. The method was modified to correlated disorder model (CDM) which takes into account the effect of energy correlation by assuming charge carriers interact with randomly orientated dipoles in surrounding sites,[119-121] in order to explain the experimentally observed Poole-Frenkel dependence of mobility on the electric field.

Vissenberg et al.[122] developed an analytical hopping transport model (VM model) for OFETs, based on exponential DOS, MA hopping rate, resistor network approach[123] and percolation method[124]. In this model, charge carriers can hop in three dimensional spaces, the conductivity of the 3D hopping system can be derived analytically. For charge transport in OFETs where charge carrier density gradually decrease in the gate electric field direction when away from the interface, the mobility at each carrier density layer is averaged to give the macroscopic field-effect mobility with an analytical equation:[122]

$$\mu = \frac{\sigma_0}{e}\left(\frac{\pi (T_0/T)^3}{(2\alpha)^3 B_c \Gamma(1-T_0/T)\Gamma(1+T_0/T)}\right)^{T_0/T} \times \left[\frac{(CV_g)}{2k_B T_0 \varepsilon_s}\right]^{T_0/T-1} \qquad (1.4)$$

Where σ_0 is the conductivity prefactor, Γ is gamma function, C is the capacitance of the FET dielectric layer, ε_S is the dielectric constant of the semiconductor, $k_B T_0$ is the width of the exponential DOS, α is a fixed value, Bc equals to 2.8, which is the average bond number for bond percolation in 3D random lattice. This model breaks down at temperature $T > T_0$ and high carrier concentration $- E_F \sim k_B T_0$, where E_F is the Fermi level which depends on temperature, carrier concentration and DOS width.

The effect of carrier concentration on mobility was studied by Tanase et al.,[125] in which the Novikov model (CDM model) and the VM model were used to extract DOS from I - V curves of diode and transistor respectively for two common used materials, OC_1C_{10}-PPV and P3HT. The results show that for both materials the extracted Exponential DOS from transistor data is a good approximation of the extracted Gaussian DOS from diode data in the energy range where the transistors operates. So with the same DOS, the difference in the measured mobility for Diode and transistor comes from strong dependence of mobility at high carrier concentration range. The carrier concentration

effect was then included into GDM to get the Extend Gauss Disorder Model (EGDM) by Pasveer et al.[126] and Coehoorn et al.[127] The various semi-analytical charge transport models[122,123,128-132] were reviewed and modified by Coehoorn et al.[127] with Gaussian DOS and MA hopping equations, in the paper the mobility μ is described as a function of the three parameters: $\hat{s}$, $N_t^{1/2}/\alpha$ and c, where $\hat{s} = \sigma/k_BT$, which characterizes the status of the system in the low electric field limit. The calculation results show that most of these models predict similar charge transport behavior at low carrier concentration region.

Mobility Edge Model The band transport and hopping transport are two extreme cases for charge transport. At the existence of both band states and trap states, the charge carriers in the trap states can be thermally activated across mobility edge into band states to transport for some distance before being trapped again, as shown in Fig. 1.6. This approach is called multi-trap release model or mobility edge model (ME) model, which is originally developed for α-Si.[13,133] This model assumes that charge carriers in the band have constant mobility μ_0, while charge carriers in the trapped states have zero mobility. The DOS of the band is normally assumed to be the DOS of free electron gas and the DOS of the trap state is described by an exponential function, the two DOS is connected at the mobility edge. The mobility of the device is given by the ratio of number of free charge carriers N_{mob} to total number of charge carriers N_{tot}, i.e. $\mu = \mu_0 N_{mob}/N_{tot}$.

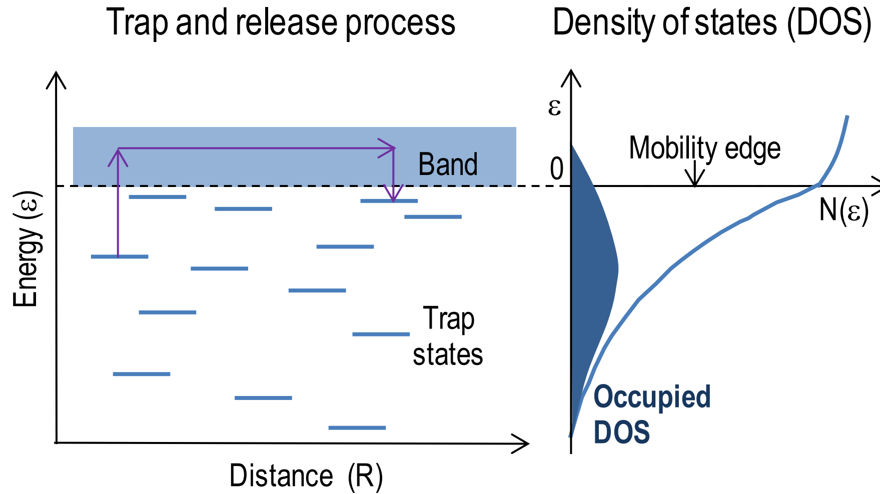

Figure 1.6 Illustration of the charge transport process in the mobility edge model.

1.5 Motivation

The charge transport process in polymer semiconductors is not well understood because of the disorder nature of the polymer semiconductors.[93] At the presence of strong disorder, hopping transport models are suitable to describe the charge transport process in OFETs. The Gaussian disorder model first developed by Bässler et al.[118] gives a simple view of charge transport physics in disordered materials at low carrier concentration limit, which is governed by charge hopping process from Occupied DOS center to a fixed transport level. The charge transport is determined by the DOS tail that is occupied by charge carriers while DOS shape above transport level does not matter much.

The analytical equation in the EGDM developed by Coehoorn et al.[127] can fit some of our PBTTT FET data quite well in a wide carrier concentration and temperature ranges with reasonable fitting parameters. This provides evidence that the charge transport is essentially a hopping process and coincides with the large disorder in the π-stacking

direction from detailed study of PBTTT XRD data,[16] despite the observed highly ordered structure in PBTTT AFM data.[95] There are some basic assumptions in the equation derivation making it more suitable to work in low carrier concentration range with diodes, which needs to be justified to apply it on transistors. Also in view that the charge transport process in OFETs should be treated as a 2D or quasi-2D process because the charge carriers distribute in a very thin layer near dielectric with high carrier density.[134] We decide to develop a universal transport model for OFETs based on Coehoorn model, making change to several other limitations in current hopping transport models such as the fixed DOS shape, fixed coupling parameters etc. besides the issue with carrier concentration and dimensionality.

1.6 Outline

In Chapter 2, we will modify two existing hopping transport models to compare the charge transport behavior in 2D and 3D. In Chapter 3, we develop an “universal“ two-dimensional charge transport model for field-effect transistors. In chapter 4, we use rrP3HT bottom-gate bottom-contact FETs to validate the new charge transport model developed in Chapter 3 and to study the effect of dielectric surface on the transport DOS. In chapter 5, we study the effect of molecular weight and processing on charge transport in PBTTT-C14 top-gate bottom-contact OFETs. In chapter 6, we study the charge transport in a high electron mobility donor-acceptor polymer P(NDI2OD-T2) with top-gate bottom-contact OFETs.

1.7 References

1 Tsumura, A., Koezuka, H. & Ando, T. Macromolecular electronic device: Field-effect transistor with a polythiophene thin-film. *Appl. Phys. Lett.* **49**, 1210 (1986).

2 Koezuka, H., Tsumura, A. & Ando, T. Field-Effect Transistor with polythiophene thin-film. *Synth. Met.* **18**, 699-704 (1987).

3 Burroughes, J. H., Jones, C. A. & Friend, R. H. New semiconductor-device physics in polymer Diodes and Transistors. *Nature* **335**, 137-141 (1988).

4 Tang, C. W. & Vanslyke, S. A. Organic electroluminescent diodes. *Appl. Phys. Lett.* **51**, 913-915 (1987).

5 Burroughes, J. H. *et al.* Light-emitting diodes based on conjugated polymers. *Nature* **347**, 539-541 (1990).

6 Tang, C. W. Two-layer organic photovoltaic cell. *Appl. Phys. Lett.* **48**, 183-185 (1986).

7 Friend, R. H. *et al.* Electroluminescence in conjugated polymers. *Nature* **397**, 121 (1999).

8 Sirringhaus, H. 25th Anniversary Article: Organic Field-Effect Transistors: The Path Beyond Amorphous Silicon. *Adv. Mater.* **26**, 1319 (2014).

9 Dou, L. T. *et al.* 25th Anniversary Article: A Decade of Organic/Polymeric Photovoltaic Research. *Adv. Mater.* **25**, 6642 (2013).

10 Bredas, J. L., Calbert, J. P., da Silva, D. A. & Cornil, J. Organic semiconductors: A theoretical characterization of the basic parameters governing charge transport. *PNAS* **99**, 5804 (2002).

11 Gershenson, M. E., Podzorov, V. & Morpurgo, A. F. Colloquium: Electronic transport in single-crystal organic transistors. *Rev. Mod. Phys.* **78**, 973 (2006).

12 Troisi, A. Charge transport in high mobility molecular semiconductors: classical models and new theories. *Chem. Soc. Rev.* **40**, 2347 (2011).

13 Street, R. A., Northrup, J. E. & Salleo, A. Transport in polycrystalline polymer thin-film Transistors. *Phys. Rev. B* **71**, 165202 (2005).

14 Bässler, H. & Kohler, A. in *Unimolecular and Supramolecular Electronics I: Chemistry and Physics Meet at Metal-Molecule Interfaces* Vol. 312 *Topics in Current Chemistry* 1-65 (2012).

15 Coropceanu, V. *et al.* Charge transport in organic semiconductors. *Chem. Rev.* **107**, 926 (2007).

16 Noriega, R. & Salleo, A. in *Organic Electronics II: More Materials and Applications* (2012).

17 Arias, A. C., MacKenzie, J. D., McCulloch, I., Rivnay, J. & Salleo, A. Materials and Applications for Large Area Electronics: Solution-Based Approaches. *Chem. Rev.* **110**, 3 (2010).

18 Klauk, H. Organic thin-film transistors. *Chem. Soc. Rev* **39**, 2643 (2010).

19 Gelinck, G. H. *et al.* Flexible active-matrix displays and shift registers based on solution-processed organic transistors. *Nat. Mater.* **3**, 106 (2004).

20 Street, R. A. Thin-Film Transistors. *Adv. Mater.* **21**, 2007 (2009).

21 Cantatore, E. *et al.* A 13.56-MHz RFID system based on organic transponders. *IEEE J. Solid-State Circuits* **42**, 84 (2007).

22 Myny, K. *et al.* An 8-Bit, 40-Instructions-Per-Second Organic Microprocessor on Plastic Foil. *IEEE J. Solid-State Circuits* **47**, 284 (2012).

23 Hammock, M. L., Chortos, A., Tee, B. C. K., Tok, J. B. H. & Bao, Z. A. 25th Anniversary Article: The Evolution of Electronic Skin (E-Skin): A Brief History, Design Considerations, and Recent Progress. *Adv. Mater.* **25**, 5997 (2013).

24 Kaltenbrunner, M. *et al.* An ultra-lightweight design for imperceptible plastic electronics. *Nature* **499**, 458 (2013).

25 Bauer, S. *et al.* 25th Anniversary Article: A Soft Future: From Robots and Sensor Skin to Energy Harvesters. *Adv. Mater.* **26**, 149 (2014).

26 Wang, C. L., Dong, H. L., Hu, W. P., Liu, Y. Q. & Zhu, D. B. Semiconducting pi-Conjugated Systems in Field-Effect Transistors: A Material Odyssey of Organic Electronics. *Chem. Rev.* **112**, 2208 (2012).

27 Nielsen, C. B., Turbiez, M. & McCulloch, I. Recent advances in the development of semiconducting DPP-containing polymers for transistor applications. *Adv. Mater.* **25**, 1859 (2013).

28 Zhao, Y., Guo, Y. L. & Liu, Y. Q. 25th Anniversary Article: Recent Advances in n-Type and Ambipolar Organic Field-Effect Transistors. *Adv. Mater.* **25**, 5372 (2013).

29 Mannsfeld, S. C. B., Tang, M. L. & Bao, Z. A. Thin Film Structure of Triisopropylsilylethynyl-Functionalized Pentacene and Tetraceno 2,3-b thiophene from Grazing Incidence X-Ray Diffraction. *Adv. Mater.* **23**, 127 (2011).

30 Nakayama, K. *et al.* Patternable solution-crystallized organic transistors with high charge carrier mobility. *Adv. Mater.* **23**, 1626 (2011).

31 Facchetti, A. pi-Conjugated polymers for organic electronicsan d photovoltaic cell applications. *Chem. Mater.* **23**, 733 (2011).

32 McCulloch, I. *et al.* Liquid-crystalline semiconducting polymers with high charge-carrier mobility. *Nat. Mater.* **5**, 328 (2006).

33 Yan, H. *et al.* A high-mobility electron-transporting polymer for printed transistors. *Nature* **457**, 679 (2009).

34 Li, Y. N., Singh, S. P. & Sonar, P. A high mobility p-type DPP-Thieno 3,2-b thiophene copolymer for organic thin-film Transistors. *Adv. Mater.* **22**, 4862 (2010).

35 Park, S. K., Jackson, T. N., Anthony, J. E. & Mourey, D. A. High mobility solution processed 6,13-bis(triisopropyl-silylethynyl) pentacene organic thin film transistors. *Appl. Phys. Lett.* **91**, 063514 (2007).

36 Anthony, J. E., Facchetti, A., Heeney, M., Marder, S. R. & Zhan, X. W. n-Type Organic Semiconductors in Organic Electronics. *Adv. Mater.* **22**, 3876 (2010).

37 Takimiya, K., Shinamura, S., Osaka, I. & Miyazaki, E. Thienoacene-based organic semiconductors. *Adv. Mater.* **23**, 4347 (2011).

38 Giri, G. *et al.* Tuning charge transport in solution-sheared organic semiconductors using lattice strain. *Nature* **480**, 504 (2011).

39 Minemawari, H. *et al.* Inkjet printing of single-crystal films. *Nature* **475**, 364 (2011).

40 Sirringhaus, H. *et al.* Two-dimensional charge transport in self-organized, high-mobility conjugated polymers. *Nature* **401**, 685-688 (1999).

41 McCulloch, I. *et al.* Semiconducting thienothiophene copolymers: Design, synthesis, morphology, and performance in thin-film organic transistors. *Adv. Mater.* **21**, 1091 (2009).

42 Zhang, Z. G. & Wang, J. Z. Structures and properties of conjugated Donor-Acceptor copolymers for solar cell applications. *J. Mater. Chem.* **22**, 4178 (2012).

43 Tsao, H. N. *et al.* Ultrahigh Mobility in Polymer Field-Effect Transistors by Design. *J. Am. Chem. Soc* **133**, 2605 (2011).

44 Zhang, W. M. *et al.* Indacenodithiophene Semiconducting Polymers for High-Performance, Air-Stable Transistors. *J. Am. Chem. Soc* **132**, 11437 (2010).

45 Kang, I., Yun, H. J., Chung, D. S., Kwon, S. K. & Kim, Y. H. Record High Hole Mobility in Polymer Semiconductors via Side-Chain Engineering. *J. Am. Chem. Soc* **135**, 14896 (2013).

46 Sun, B., Hong, W., Yan, Z., Aziz, H. & Li, Y. Record High Electron Mobility of 6.3 $cm^2 V^{-1} s^{-1}$ Achieved for Polymer Semiconductors Using a New Building Block. *Adv. Mater.*, doi:10.1002/adma.201305981 (2014).

47 Tseng, H. R. *et al.* High-Mobility Field-Effect Transistors Fabricated with Macroscopic Aligned Semiconducting Polymers. *Adv. Mater.*, (early view) (2014).

48 Zaumseil, J. & Sirringhaus, H. Electron and ambipolar transport in organic field-effect transistors. *Chem. Rev.* **107**, 1296 (2007).

49 Baeg, K. J. *et al.* Remarkable enhancement of hole transport in top-gated n-Type polymer field-effect transistors by a high-k dielectric for ambipolar electronic circuits. *Adv. Mater.* **24**, 5433 (2012).

50 Chen, Z. Y. *et al.* High-Performance ambipolar Diketopyrrolopyrrole-Thieno 3,2-b thiophene copolymer Field-Effect Transistors with balanced hole and electron mobilities. *Adv. Mater.* **24**, 647 (2012).

51 Wen, Y. G., Liu, Y. Q., Guo, Y. L., Yu, G. & Hu, W. P. Experimental techniques for the fabrication and characterization of organic thin films for field-effect transistors. *Chem. Rev.* **111**, 3358 (2011).

52 Tsao, H. N. & Mullen, K. Improving polymer transistor performance via morphology control. *Chem. Soc. Rev* **39**, 2372 (2010).

53 Wang, S. *et al.* Solvent effects and multiple aggregate states in high-mobility organic field-effect transistors based on poly(bithiophene-alt-thienothiophene). *Appl. Phys. Lett.* **93**, 162103 (2008).

54 Liu, S. H., Wang, W. C. M., Briseno, A. L., Mannsfeld, S. C. E. & Bao, Z. N. Controlled deposition of crystalline organic semiconductors for field-effect-transistor applications. *Adv. Mater.* **21**, 1217 (2009).

55 Chabinyc, M. L., Toney, M. F., Kline, R. J., McCulloch, I. & Heeney, M. X-ray scattering study of thin films of poly(2,5-bis(3-alkylthiophen-2-yl)thieno 3,2-b thiophene). *J. Am. Chem. Soc.* **129**, 3226 (2007).

56 DeLongchamp, D. M. *et al.* Controlling the Orientation of Terraced Nanoscale "Ribbons" of a Poly(thiophene) Semiconductor. *Acs Nano* **3**, 780 (2009).

57 Lee, M. J. *et al.* Anisotropy of charge transport in a uniaxially aligned and chain-extended, high-mobility, conjugated polymer semiconductor. *Adv. Func. Mater.* **21**, 932 (2011).

58 Jimison, L. H., Toney, M. F., McCulloch, I., Heeney, M. & Salleo, A. Charge-transport anisotropy due to grain boundaries in directionally crystallized thin films of regioregular poly(3-hexylthiophene). *Adv. Mater.* **21**, 1568 (2009).

59 Sirringhaus, H. *et al.* Mobility enhancement in conjugated polymer field-effect transistors through chain alignment in a liquid-crystalline phase. *Appl. Phys. Lett.* **77**, 406 (2000).

60 Zheng, Z. J. *et al.* Uniaxial alignment of liquid-crystalline conjugated polymers by nanoconfinement. *Nano Lett.* **7**, 987 (2007).

61 Facchetti, A., Yoon, M. H. & Marks, T. J. Gate dielectrics for organic field-effect transistors: New opportunities for organic electronics. *Adv. Mater.* **17**, 1705 (2005).

62 Ortiz, R. P., Facchetti, A. & Marks, T. J. High-k Organic, Inorganic, and Hybrid Dielectrics for Low-Voltage Organic Field-Effect Transistors. *Chem. Rev.* **110**, 205 (2010).

63 Veres, J., Ogier, S. D., Leeming, S. W., Cupertino, D. C. & Khaffaf, S. M. Low-k insulators as the choice of dielectrics in organic field-effect transistors. *Adv. Func. Mater.* **13**, 199 (2003).

64 Veres, J., Ogier, S., Lloyd, G. & de Leeuw, D. Gate insulators in organic field-effect transistors. *Chem. Mater.* **16**, 4543 (2004).

65 Hulea, I. N. *et al.* Tunable Frohlich polarons in organic single-crystal transistors. *Nat. Mater.* **5**, 982 (2006).

66 Richards, T., Bird, M. & Sirringhaus, H. A quantitative analytical model for static dipolar disorder broadening of the density of states at organic heterointerfaces. *J. Chem. Phys.* **128** (2008).

67 Zhao, N. *et al.* Polaron localization at interfaces in high-mobility microcrystalline conjugated polymers. *Adv. Mater.* **21**, 3759 (2009).

68 Chua, L. L. *et al.* General observation of n-type field-effect behaviour in organic semiconductors. *Nature* **434**, 194-199 (2005).

69 Zaumseil, J., Friend, R. H. & Sirringhaus, H. Spatial control of the recombination zone in an ambipolar light-emitting organic transistor. *Nat. Mater.* **5**, 69 (2006).

70 Zaumseil, J., Donley, C. L., Kim, J. S., Friend, R. H. & Sirringhaus, H. Efficient top-gate, ambipolar, light-emitting field-effect transistors based on a green-light-emitting polyfluorene. *Adv. Mater.* **18**, 2708 (2006).

71 Zhuo, J. M. *et al.* Evidence for a transistion adlayer interface structure that determines the field-effect transport in semicrystalline polymer organic semiconductor films (Manuscript in preparation).

72 Yoon, M. H., Kim, C., Facchetti, A. & Marks, T. J. Gate dielectric chemical structure-organic field-effect transistor performance correlations for electron, hole, and ambipolar organic semiconductors. *J. Am. Chem. Soc.* **128**, 12851 (2006).

73 Kline, R. J., McGehee, M. D. & Toney, M. F. Highly oriented crystals at the buried interface in polythiophene thin-film transistors. *Nat. Mater.* **5**, 222 (2006).

74 Chua, L. L., Ho, P. K. H., Sirringhaus, H. & Friend, R. H. Observation of field-effect transistor behavior at self-organized interfaces. *Adv. Mater.* **16**, 1609 (2004).

75 Majewski, L. A., Schroeder, R. & Grell, M. One volt organic transistor. *Adv. Mater.* **17**, 192 (2005).

76 Yoon, M. H., Yan, H., Facchetti, A. & Marks, T. J. Low-voltage organic field-effect transistors and inverters enabled by ultrathin cross-linked polymers as gate dielectrics. *J. Am. Chem. Soc.* **127**, 10388 (2005).

77 Cheng, X. Y. *et al.* Air Stable Cross-Linked Cytop Ultrathin Gate Dielectric for High Yield Low-Voltage Top-Gate Organic Field-Effect Transistors. *Chem. Mater.* **22**, 1559 (2010).

78 Halik, M. *et al.* Low-voltage organic transistors with an amorphous molecular gate dielectric. *Nature* **431**, 963 (2004).

79 Klauk, H., Zschieschang, U., Pflaum, J. & Halik, M. Ultralow-power organic complementary circuits. *Nature* **445**, 745 (2007).

80 Cho, J. H. *et al.* Printable ion-gel gate dielectrics for low-voltage polymer thin-film transistors on plastic. *Nat. Mater.* **7**, 900 (2008).

81 Kim, S. H. *et al.* Electrolyte-Gated Transistors for Organic and Printed Electronics. *Adv. Mater.* **25**, 1822 (2013).

82 Bürgi, L., Sirringhaus, H. & Friend, R. H. Noncontact potentiometry of polymer field-effect transistors. *Appl. Phys. Lett.* **80**, 2913 (2002).

83 Natali, D. & Caironi, M. Charge injection in solution-processed organic field-effect transistors: Physics, models and characterization methods. *Adv. Mater.* **24**, 1357 (2012).

84 Bürgi, L., Richards, T. J., Friend, R. H. & Sirringhaus, H. Close look at charge carrier injection in polymer field-effect transistors. *J. Appl. Phys.* **94**, 6129 (2003).

85 Cheng, X. Y. *et al.* Controlling Electron and Hole Charge Injection in Ambipolar Organic Field-Effect Transistors by Self-Assembled Monolayers. *Adv. Func. Mater.* **19**, 2407 (2009).

86 Whiting, G. L. & Arias, A. C. Chemically modified ink-jet printed silver electrodes for organic field-effect transistors. *Appl. Phys. Lett.* **95**, 253302 (2009).

87 Sirringhaus, H. *et al.* High-resolution inkjet printing of all-polymer transistor circuits. *Science* **290**, 2123 (2000).

88 Sirringhaus, H. Reliability of Organic Field-Effect Transistors. *Adv. Mater.* **21**, 3859 (2009).

89 Bobbert, P. A., Sharma, A., Mathijssen, S. G. J., Kemerink, M. & de Leeuw, D. M. Operational Stability of Organic Field-Effect Transistors. *Adv. Mater.* **24**, 1146 (2012).

90 Lee, W. H., Choi, H. H., Kim, D. H. & Cho, K. 25th Anniversary Article: Microstructure Dependent Bias Stability of Organic Transistors. *Adv. Mater.* **26**, 1660 (2014).

91 Salleo, A., Kline, R. J., DeLongchamp, D. M. & Chabinyc, M. L. Microstructural characterization and charge transport in thin films of conjugated polymers. *Adv. Mater.* **22**, 3812-3838 (2010).

92 DeLongchamp, D. M., Kline, R. J., Fischer, D. A., Richter, L. J. & Toney, M. F. Molecular characterization of organic electronic films. *Adv. Mater.* **23**, 319 (2011).

93 Rivnay, J., Mannsfeld, S. C. B., Miller, C. E., Salleo, A. & Toney, M. F. Quantitative determination of organic semiconductor microstructure from the molecular to device scale. *Chem. Rev.* **112**, 5488 (2012).

94 Kline, R. J. *et al.* Dependence of regioregular poly(3-hexylthiophene) film morphology and field-effect mobility on molecular weight. *Macromol.* **38**, 3312 (2005).

95 Zhao, L. H. *et al.* Role of borderline solvents to Induce pronounced extended-chain lamellar order in pi-stackable polymers. *Macromol.* **44**, 9692 (2011).

96 Schuettfort, T. *et al.* Surface and bulk structural characterization of a high-mobility electron-transporting polymer. *Macromol.* **44**, 1530 (2011).

97 Zhang, X. R. *et al.* Molecular Packing of High-Mobility Diketo Pyrrolo-Pyrrole Polymer Semiconductors with Branched Alkyl Side Chains. *J. Am. Chem. Soc.* **133**, 15073 (2011).

98 Rivnay, J. *et al.* Drastic Control of Texture in a High Performance n-Type Polymeric Semiconductor and Implications for Charge Transport. *Macromol.* **44**, 5246 (2011).

99 Rivnay, J. *et al.* Unconventional Face-On Texture and Exceptional In-Plane Order of a High Mobility n-Type Polymer. *Adv. Mater.* **22**, 4359 (2010).

100 Rivnay, J., Noriega, R., Kline, R. J., Salleo, A. & Toney, M. F. Quantitative analysis of lattice disorder and crystallite size in organic semiconductor thin films. *Phys. Rev. B* **84**, 045203 (2011).

101 Zhang, X. R. *et al.* In-Plane Liquid Crystalline Texture of High-Performance Thienothiophene Copolymer Thin Films. *Adv. Func. Mater.* **20**, 4098 (2010).

102 Chabinyc, M. L. *et al.* Lamination method for the study of interfaces in polymeric thin film transistors. *J. Am. Chem. Soc.* **126**, 13928 (2004).

103 Ho, P. K. H. *et al.* Solvent effects on chain orientation and interchain pi-interaction in conjugated polymer thin films: Direct measurements of the air and substrate interfaces by near-edge X-ray absorption spectroscopy. *Adv. Mater.* **19**, 215 (2007).

104 DeLongchamp, D. M. *et al.* High carrier mobility polythiophene thin films: Structure determination by experiment and theory. *Adv. Mater.* **19**, 833 (2007).

105 Troisi, A. Prediction of the absolute charge mobility of molecular semiconductors: the case of rubrene. *Adv. Mater.* **19**, 2000 (2007).

106 Cornil, J., Beljonne, D. & Bredas, J. L. Nature of optical-transitions in conjugated oligomers. 2. Theoretical characterization of neutral and doped oligothiophenes. *J. Chem. Phys.* **103**, 842 (1995).

107 Cornil, J., Beljonne, D. & Bredas, J. L. Nature of optical-transitions in conjugated oligomers .1. theoretical characterization of neutral and doped oligo(phenylenevinylene)s. *J. Chem. Phys.* **103**, 834 (1995).

108 Brown, P. J., Sirringhaus, H., Harrison, M., Shkunov, M. & Friend, R. H. Optical spectroscopy of field-induced charge in self-organized high mobility poly(3-hexylthiophene). *Phys. Rev. B* **63** (2001).

109 Caironi, M. *et al.* Very Low Degree of Energetic Disorder as the Origin of High Mobility in an n-channel Polymer Semiconductor. *Adv. Func. Mater.* **21**, 3371 (2011).

110 Fesser, K., Bishop, A. R. & Campbell, D. K. Optical-absorption from polarons in a model of polyacetylene. *Phys. Rev. B* **27**, 4804 (1983).

111 Su, W. P., Schrieffer, J. R. & Heeger, A. J. Solitons in polyacetylene. *Phys. Rev. Lett.* **42**, 1698 (1979).

112 Su, W. P., Schrieffer, J. R. & Heeger, A. J. Soliton excitations in polyacetylene. *Phys. Rev. B* **22**, 2099 (1980).

113 Cheung, D. L., McMahon, D. P. & Troisi, A. A realistic description of the charge carrier wave function in microcrystalline polymer semiconductors. *J. Am. Chem. Soc.* **131**, 11179 (2009).

114 McMahon, D. P. *et al.* Relation between microstructure and charge transport in polymers of different regioregularity. *J. Phys. Chem. C* **115**, 19386 (2011).

115 Li, S. G. *et al.* THz-wave absorption by field-induced carriers in pentacene thin-film transistors for THz imaging sensors. *Org. Electron.* **14**, 1157 (2013).

116 Matsubara, R., Ohashi, N., Sakai, M., Kudo, K. & Nakamura, M. Analysis of barrier height at crystalline domain boundary and in-domain mobility in pentacene polycrystalline films on SiO_2. *Appl. Phys. Lett.* **92**, 242108 (2008).

117 Matsubara, R. *et al.* Crystal order in pentacene thin films grown on SiO2 and its influence on electronic band structure. *Org. Electron.* **12**, 195 (2011).

118 Nakamura, M. *et al.* Extrinsic limiting factors of carrier transport in organic field-effect transistors. *Appl. Phys. A* **95**, 73 (2009).

119 Ohashi, N. *et al.* Conductivity fluctuation within a crystalline domain and its origin in pentacene thin-film transistors. *Appl. Phys. Lett.* **91**, 162105 (2007).

120 Mott, N. F. Conduction in non-crystalline materials. 3. Localized states in a pseudogap and near extremities of conduction and valence bands. *Philos. Mag.* **19**, 835 (1969).

121 Miller, A. & Abrahams, E. Impurity conduction at low concentrations. *Phys. Rev.* **120**, 745 (1960).

122 Marcus, R. A. On the theory of oxidation-reduction reactions involving electron transfer. 1. *J. Chem. Phys.* **24**, 966 (1956).

123 Bässler, H. Charge transport in disordered organic photoconductors - a monte-carlo simulation study. *Phys. Status Solidi B* **175**, 15 (1993).

124 Novikov, S. V., Dunlap, D. H., Kenkre, V. M., Parris, P. E. & Vannikov, A. V. Essential role of correlations in governing charge transport in disordered organic materials. *Phys. Rev. Lett.* **81**, 4472-4475 (1998).

125 Yu, Z. G., Smith, D. L., Saxena, A., Martin, R. L. & Bishop, A. R. Molecular geometry fluctuation model for the mobility of conjugated polymers. *Phys. Rev. Lett.* **84**, 721 (2000).

126 Yu, Z. G., Smith, D. L., Saxena, A., Martin, R. L. & Bishop, A. R. Molecular geometry fluctuations and field-dependent mobility in conjugated polymers. *Phys. Rev. B* **63**, 085202 (2001).

127 Vissenberg, M. & Matters, M. Theory of the field-effect mobility in amorphous organic transistors. *Phys. Rev. B* **57**, 12964-12967 (1998).

128 Ambegaokar, V., Halperin, B. I. & Langer, J. S. Hopping conductivity in disordered systems. *Phys. Rev. B* **4**, 2612 (1971).

129 Pike, G. E. & Seager, C. H. Percolation and conductivity - computer study. 1. *Phys. Rev. B* **10**, 1421 (1974).

130 Tanase, C., Meijer, E. J., Blom, P. W. M. & de Leeuw, D. M. Unification of the hole transport in polymeric field-effect transistors and light-emitting diodes. *Phys. Rev. Lett.* **91**, 216601 (2003).

131 Pasveer, W. F. *et al.* Unified description of charge-carrier mobilities in disordered semiconducting polymers. *Phys. Rev. Lett.* **94**, 206601 (2005).

132 Coehoorn, R., Pasveer, W. F., Bobbert, P. A. & Michels, M. A. J. Charge-carrier concentration dependence of the hopping mobility in organic materials with Gaussian disorder. *Phys. Rev. B* **72**, 155206 (2005).

133 Baranovskii, S. D., Cordes, H., Hensel, F. & Leising, G. Charge-carrier transport in disordered organic solids. *Phys. Rev. B* **62**, 7934 (2000).

134 Baranovskii, S. D., Faber, T., Hensel, F. & Thomas, P. The applicability of the transport-energy concept to various disordered materials. *J. Phys.: Condens. Matter* **9**, 2699 (1997).

135 Martens, H. C. F. *et al.* Understanding the doping dependence of the conductivity of conjugated polymers: Dominant role of the increasing density of states and growing delocalization. *Phys. Rev. B* **67**, 121203 (2003).

136 Movaghar, B. & Schirmacher, W. On the theory of hopping conductivity in disordered-systems. *J. Phys. C - Solid State Phys.* **14**, 859 (1981).

137 Roichman, Y., Preezant, Y. & Tessler, N. Analysis and modeling of organic devices. *Phys. Status Solidi A* **201**, 1246 (2004).

138 Salleo, A. *et al.* Intrinsic hole mobility and trapping in a regioregular poly(thiophene). *Phys. Rev. B* **70**, 115311 (2004).

139 Chua, L. L., Friend, R. H. & Ho, P. K. H. Organic double-gate field-effect transistors: Logic-AND operation. *Appl. Phys. Lett.* **87**, 253512 (2005).

Chapter 2. Hopping charge transport in two−dimensional space

In this chapter, we modify two existing hopping transport models, Vissenberg-Matters (VM) model and Martens model, into 2D with Gaussian Density of States (DOS) following formulism in the paper by Coehoorn et al.[1] The calculated reduced mobility-carrier concentration-temperature surfaces are similar for these two models. In comparison of the charge transport behavior in 2D and 3D with VM model, the results show that the average hopping distance of charge carriers is larger in 2D due to the reduced number of neighboring sites with low site energy differences, also more importantly the reduced mobility is lower in 2D at all carrier concentrations especially for low temperature and low site density cases. The results show that the reduced neighboring site density from 3D to 2D has a large impact on the charge transport behavior. Both models break down at relatively high carrier concentration region, in which mobility rapidly drops with increasing carrier concentration.

2.1 Introduction

In field-effect transistors the charge carriers in the channel accumulate in a very thin (1 − 2 nm) layer near to the dielectric,[2,3] thus the two main features in the charge transport in FETs are: high carrier density and restricted transport space. The charge carrier mobility in organic FETs is shown to increase with carrier density in device operation region (~ several 10^{12} cm^{-2})[4] and this effect is incorporated into the hopping transport models,[5-7] within which charge carriers are generally allowed to transport in three-dimensional (3D) space, that seems to contradict the situation in FETs.

The dimensionality of charge transport in organic FETs has been studied by both experiments and numerical simulations. In the experiments, generally the performance of FET devices is measured as a function of semiconductor thickness. The studies with small molecules show that the charge carrier mobility saturates at a coverage of about two monolayers of the molecules.[8,9] Similarly for FET devices with polymer layers deposited by Langmuir-Blodgett (LB) method, the charge carrier mobility saturates at one monolayer for rrP3HT[10] and three monolayers for P(NDI2OD-T2)[11]. For FET device with spin-on PBTTT film, the charge carrier mobility saturates when the film thickness is around 20 nm.[12] In the simulation study, similarly the charge transport behavior is monitored while increasing the number of monolayers. The current is shown mainly in the first two monolayers at most conditions regardless of the degree of disorder, applied gate voltage etc.[13]

It seems necessary to use two-dimensional (2D) charge transport model for organic FETs in view of the reduced dimensionality of charge transport in them, especially for FETs with monolayer semiconductor. For example, in a self assembled monolayer field-effect transistor (SAMFET) with semiconducting SAM as active layer,[14] in which

the charge transport is truly two-dimensional. The mobility edge (ME) model can be easily applied in 2D situation by using 2D density of states (DOS).[15] Some of the hopping transport models are also modified into 2D to study the resulted charge transport behavior, reporting reduced mobility[16] and reduced temperature dependence of source-drain current[17].

In this chapter, we will modify the VM model and the Martens model into 2D form following the formulism in the paper by Coehoorn et al.,[1] to study the charge transport behavior in 2D and compare with that in 3D.

2.2 Modification of hopping transport models to 2D

In this modification we keep the same basic assumptions of the extended Gaussian disorder model,[1,7] just that the charge carriers are now only allowed to hop in a two-dimensional space. The basic transport picture is that: charge carriers are localized onto charge transport sites as a result of disorder; the sites distribute randomly in the 2D space; charge carriers can hop between sites with assist of thermal energy.

The site energies are assumed to be not correlated to each other and the density of states (DOS) of the system i.e. the site energy distribution is given by a Gaussian function:

$$g(\varepsilon) = \frac{N_t}{\sqrt{2\pi}\sigma} \exp(-\frac{\varepsilon^2}{2\sigma^2}) \quad (2.1)$$

Where ε is the site energy, σ is the DOS width, N_t is the site density in 2D (unit cm^{-2}). The occupational probability of energy levels is given by Fermi-Dirac statistics:

$$f(\varepsilon) = \frac{1}{1+\exp(\frac{\varepsilon-\mu}{k_B T})} \cong \frac{1}{1+\exp(\frac{\varepsilon-E_F}{k_B T})} \quad (2.2)$$

Where k_B is Boltzmann constant, T is temperature, μ is chemical potential at the site and it is related to the Fermi level E_F by the equation: $\mu = E_F - eER_x$, where e is elementary charge, E is the electric field at the site and R_x is the component of site position vector $\vec{R}$ in the electric field direction. In the low electric field limit, which is the case in the channel of organic FETs where charge transport happens, μ and E_F are roughly same as each other. For a certain carrier density c, E_F of the system is given by the equation $c = \int_{-\infty}^{+\infty} d\varepsilon g(\varepsilon) f(\varepsilon)$.

The hopping rate between sites is given by the Miller-Abrahams (MA) equation:[18]

$$w_{ij} = \begin{cases} \nu_0 \exp(-2\alpha R_{ij} - \frac{\varepsilon_i - \varepsilon_j}{k_B T}) & \varepsilon_j < \varepsilon_i \\ \nu_0 \exp(-2\alpha R_{ij}) & \varepsilon_j \geq \varepsilon_i \end{cases} \quad (2.3)$$

where w_{ij} is the hopping rate from site j to i, ν_0 is the attempt frequency, R_{ij} is the distance between sites i and j, ε_i and ε_j are the site energies whose values are taken from the Gaussian distribution, α is the inverse of the delocalization length of the wave function of the charge carriers and its value is assumed to be the same for all sites.

As described in the paper by Coehoorn et al.,[1] under these basic assumptions and in the low electric field limit, the status of the system can be characterized by three dimensionless parameters: $\hat{s}$, $N_t^{1/2}/\alpha$ and c, where $\hat{s} = \sigma / k_B T$, since these include all the fundamental parameters of the system. As a result, the charge transport behavior of charge carriers in the system, which is generally described by the mobility

μ of charge carriers, will be derived as a function of the three parameters with some other pre-factor terms describing macroscopic properties of the system.

There are several semi-analytical hopping transport models to determine the charge carrier mobility μ from the three parameters and most of them predict similar charge transport behaviors under Gaussian DOS, as reviewed by Coehoorn et al.[1] We will choose Vissenberg-Matters (VM) model[5] and the model by Martens et al.[19] (Martens model) to modify into 2D, and based on that to try to derive an analytical equation of μ in 2D similar to its 3D form following the derivation procedures in paper by Coehoorn et al.[1]

2.2.1 2D Vissenberg-Matters (VM) model

In the Vissenberg-Matters model,[5] the charge transport is treated as percolation of charge carriers in a resistor network, within which any two sites i and j is connected with a resistor $R_{ij} = 1/G_{ij}$, The resistor cluster, which contains all the high conductivity paths with $G_{ij} \leq G_x$, only becomes percolated i.e. conductive when G_x increases to the critical value G_c. The system conductance G equals to the conductance of the cluster at the percolation threshold, which is determined by the conduction paths in the cluster with highest conductance G_c. So only hopping paths with $G_{ij} \leq G_c$ contribute to the charge transport and the charge carrier mobility of the system is determined by the most difficult hops.

At steady states when the site occupational probability is not changing, the current I_{ij} between site i and j is given by: $I_{ij} = e(w_{ij} f_j (1-f_i) - w_{ji} f_i (1-f_j))$, where *w* is the MA hopping rate and f is the Fermi-Dirac occupational probability. So in the low electric

field limit and low carrier concentration limit, the conductance G_{ij} of hopping path between i and j is given as:

$$G_{ij} = G_0 \exp(-2\alpha R_{ij} - \frac{\left|\varepsilon_i - \varepsilon_j\right| + \left|\varepsilon_i - E_F\right| + \left|\varepsilon_j - E_F\right|}{2k_B T}) \qquad (2.4)$$

Where $G_0 = e^2 \nu_0 / k_B T$. Eqn. 2.4 can be written as $G_{ij} = G_0 \exp(-s_{ij})$ and for critical conductance $G_c = G_0 \exp(-s_c)$. The system conductivity σ is assumed to be proportional to G_c and is given by this equation:

$$\sigma = \sigma_0 \exp(-s_c) \qquad (2.5)$$

where $\sigma_0 = G_0 / N_t^{-1/2}$.[1] The value of s_c is calculated as follow: for the resistor cluster at percolation threshold, each site in it has on average B_c connections i.e. conduction paths to all the other sites in it, as described by this equation:

$$N_b(s_c) / N_s(s_c) = B_c \qquad (2.6)$$

Where $N_b(s_c)$ and $N_s(s_c)$ is the bond and site density in the resistor cluster at percolation threshold respectively, B_c equals to about 4.5 for a two-dimensional random lattice.[20] As required by $s_{ij} \leq s_c$ for the conduction paths to be able contribute to the charge transport, we can calculate N_b and N_s using the equations: $N_s(s_c) = \int_{E_F - s_c k_B T}^{E_F + s_c k_B T} g(\varepsilon) d\varepsilon$ and $N_b(s_c) = \int d^3 R_{ij} \int_{-\infty}^{+\infty} d\varepsilon_i \int_{-\infty}^{+\infty} d\varepsilon_j g(\varepsilon_i) g(\varepsilon_j) \theta(s_c - s_{ij})$, where θ is the Heaviside step function.[1]

2.2.2 2D Martens model

In the model by Martens et al. (Martens model),[19] the system conductance is determined by critical hops from sites at Fermi level E_F to a neighboring site with site energy $E*$ at distance $R*$ away, such that the conductance $G*$ of this hopping path is the smallest among hopping paths to all the other neighbors. The system conductivity σ is proportional to $G*$ and assumed to be given by:

$$\sigma = \sigma_0 \exp(-2\alpha R^* - \frac{\varepsilon^* - E_F}{k_B T}) \tag{2.7}$$

Where σ_0 is similar to that in VM model, $R*$ and $E*$ can be calculated from the two criteria:

(1) Each site has on average B_M neighboring sites within radius R^*, whose energy is between E_F and ε^*.

(2) R^* and ε^* are taken such that the conductivity is minimal.

The two criteria can be written into following equations under Gaussian DOS:

$$R* = \left(\frac{\frac{2B_M}{\pi N_t}}{erf(\frac{\varepsilon *}{\sqrt{2}\sigma}) - erf(\frac{E_F}{\sqrt{2}\sigma})}\right)^{\frac{1}{2}} \tag{2.8}$$

$$\frac{\sqrt{\frac{2}{\pi}}(\frac{2B_M}{\pi})^{\frac{1}{2}} \frac{\alpha}{N_t^{1/2}} \exp(\frac{\varepsilon *^2}{\sqrt{2}\sigma^2})}{(erf(\frac{\varepsilon *}{\sqrt{2}\sigma}) - erf(\frac{E_F}{\sqrt{2}\sigma}))^{\frac{3}{2}}} = \hat{s} \tag{2.9}$$

Where erf is the error function, the value of B_M in 2D is taken to be 2.6, which is determined following the same procedure as in 3D,[1] such that with 2D uniform DOS

the VM model and Martens model predict the same charge transport behavior as the variable range hopping model by Mott.[21] The model by Mott predicts that the conductivity of a 2D variable range hopping system is given by $\sigma = \sigma_0 \exp[-(T_1/T)^3]$, Where T_1 is the characteristic temperature expressed as $\xi\alpha^2 / k_B C$, C is the site density in the 2D uniform DOS, ξ is a constant. With same 2D uniform DOS, the value of ξ in 2D VM and Martens is given by $16Bc/\pi$ and $27B_M/\pi$ respectively. So with $Bc = 4.5$ for 2D VM model, we have $B_M = 2.6$ for 2D Martens model.

2.3 Results and discussion

The charge carrier mobility $\mu = \sigma / ce = \sigma / fN_te$, at zero concentration limit f can be written as $f = \exp(E_F / k_BT + \hat{s}^2 / 2)$.[1] Based on the conductivity equations in 2D VM and Martens model, we can write $\mu = \mu_0\, exp(-p)$ = $\mu_0\, \mu_{red}$, where $\mu_0 = \sigma_0 / N_te$ and $\mu_{red} = exp(-p)$ is a function of the three parameters: $\hat{s}$, $N_t^{1/2}/\alpha$ and c.[1]

2.3.1 Mobility at zero carrier concentration limit

At zero carrier concentration limit, μ can be written as $\mu(0) = \mu_0\mu_{red}(0) = \mu_0 exp(-p(0))$ and $\mu_{red}(0)$ is only function of $\hat{s}$ and $N_t^{1/2}/\alpha$. The $\mu_{red}(0)$ can be further simplified into function of $N_t^{1/2}/\alpha$ only at the high temperature (T) limit, at which point an analytical equation of $p(0)|_{T\to\infty} = p_0$ can be obtained and it is expressed as $p_0 = (4B_c/\pi)^{1/2} * (N_t^{1/2}/\alpha)$ for VM model and $p_0 = (4B_M/\pi)^{1/2} * (N_t^{1/2}/\alpha)$ for Martens model. So $p(0)$ can be written as p_0 plus a temperature dependent term expressed as

a Taylor expansion of $\hat{s}$, i.e $p(0) = p_0 + a\hat{s} + b\hat{s}^2$. Where we take only first two terms of the Taylor expansion, a and b are prefactors that can be obtained by polynomial fitting of numerical calculation results of $p(0)$ or derived analytically.

The $p(0)$ in 3D can be expressed in an analytical equation, for which $a = 0.566$ and $b = 0.5 - d/p_0$ where $d = 0.680$.[1] Following the same derivation procedure, we obtained $a = 0.496$ and $d = -0.246$ for 2D case. The negative value of constant d is different from the positive values obtained by numerical calculation, which seems to be consistent for both 2D VM and Martens models, therefore the discussion will be based on the numerical calculation results.

Similarly to that in 3D, at zero-concentration limit the charge transport behavior in 2D VM and Martens model is very similar as shown in Fig. 2.1a. In general, 2D Martens model predicts slightly higher reduced mobility than 2D VM model, the difference only becomes large at low site density combined with high temperature or low disorder. The comparison of charge transport behavior in 2D and 3D is made with VM model as shown in Fig. 2.1b. The reduced mobility is always higher in 3D than that in 2D. The difference depends very weakly on ŝ but rapidly increase as the site density decreases. This reduction of mobility in 2D is a natural result of the reduced dimensionality in variable range hopping system. As a result, the neighboring site density greatly decreases from 3D to 2D, charge carriers are thus forced to hop longer distances in order to find neighbors with small site energy differences which are more difficult hops and consequently lower down the mobility, also the lowering effect are much stronger at low site density range.

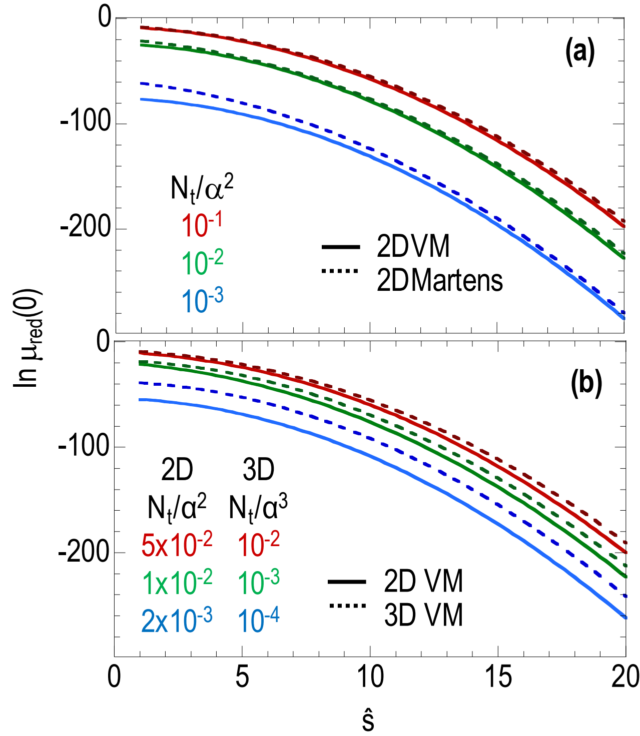

Figure 2.1 Calculated zero-concentration limit reduced mobility $\mu_{red}(0)$ results. (a) $\mu_{red}(0)$ by 2D Vissenberg-Matters (VM) model and 2D Martens model with Gaussian Density of States (DOS) at different N_t/α^2. (b) $\mu_{red}(0)$ by 2D and 3D VM models with Gaussian DOS, under same inter-site distance (assuming same α in 2D and 3D).

The increase of hopping distance in 2D and the effect of $\hat{s}$ and $N_t^{1/2}/\alpha$ on hopping distance can be seen clearly from calculated R^* results by 2D Martens model, as shown in Fig. 2.2. At high temperature limit, charge carriers can obtain enough thermal energy to overcome whatever the energy difference it is to the nearest neighbor, thus the charge transport is characterized by nearest neighbor hopping. When temperature decreases, charge carriers are forced to hop longer distances in order to find neighbors with small site energy differences, thus R^* increases with T. The charge transport becomes non-nearest neighbor hopping except for the case of very low site density, in which the average intersite distance is so large that the mobility is dominated by the distance term, thus the charge transport is nearest neighbor hopping regardless of the temperature.

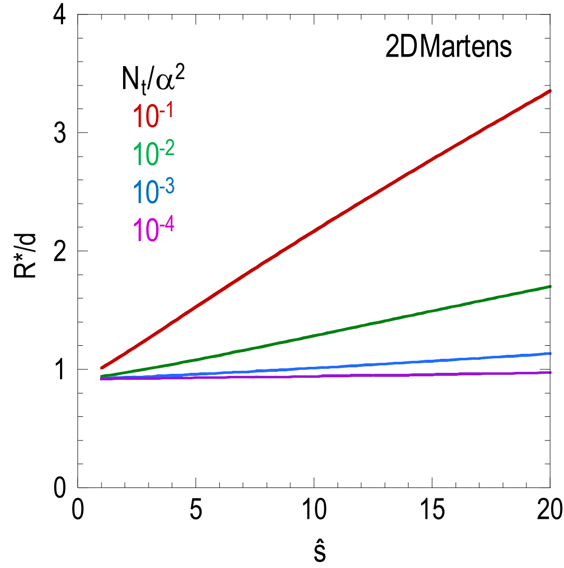

Figure 2.2 Calculated critical hopping distance R^* in unit of average inter-site distance under different N_t/α^2 by 2D Martens model with Gaussian DOS. (Assuming same α)

Table 2.1 shows the fitted p_0, a and b from calculated $p(0)$ in the range $2 < \hat{s} < 6$ for both 2D VM and Martens models at different site densities, together with values of p_0 calculated from the theoretical equations. The numerical and theoretical values of p_0 match each other very well. The value of a and b basically do not depend on $N_t^{1/2}/\alpha$, except for the value of a in 2D Martens model which increases with $N_t^{1/2}/\alpha$

	2D VM model				2D Martens Model			
N_t/α^2	$p_{0\ theory}$	p_0	a	b	$p_{0\ theory}$	p_0	a	b
1	2.39	3.16	0.048	0.391	1.84	3.28	-0.27	0.400
$5x10^{-1}$	3.38	3.79	0.366	0.388	2.60	3.99	0.032	0.396
$3x10^{-1}$	4.36	4.48	0.563	0.390	3.36	4.69	0.257	0.393
$2x10^{-1}$	5.34	5.28	0.673	0.397	4.11	5.39	0.434	0.392
$1x10^{-1}$	7.55	7.35	0.725	0.422	5.81	6.99	0.728	0.391
$5x10^{-2}$	10.68	10.56	0.650	0.453	8.22	9.35	0.978	0.396
$3x10^{-2}$	13.79	13.74	0.595	0.470	10.61	11.61	1.192	0.395
$2x10^{-2}$	16.89	16.87	0.574	0.478	13.00	13.94	1.331	0.398
$1x10^{-2}$	23.88	23.88	0.566	0.485	18.39	19.25	1.549	0.404
$1x10^{-3}$	75.52	75.52	0.564	0.495	58.14	58.84	2.150	0.425
$1x10^{-4}$	238.83	238.83	0.564	0.498	183.86	184.46	2.602	0.441

Table 2.1 The fitted p_0, a and b and the theoretical p_0 for both 2D VM and Martens models at different site densities.

2.3.2 Carrier concentration dependent mobility

Figure 2.3a shows the calculated carrier concentration dependent reduced mobility $\mu_{red}(f)$ for both 2D VM and Martens models at $N_t/\alpha^2 = 10^{-2}$. Again the two models predict similar charge transport behavior while 2D Martens model predicting higher mobility. The mobility is only carrier concentration (f) dependent when f is larger than certain threshold value, which increases with site density. Both models break down at relatively high carrier concentration range where the model assumptions are no longer

valid. Figure 2.3b shows the $\mu_{red}(f)$ for VM model in both 2D and 3D with $N_t/\alpha^2 = 10^{-2}$ and $N_t/\alpha^3 = 10^{-3}$ respectively. Again we can see that μ_{red} in 3D is larger than that in 2D as a natural result of reduced dimensionality in variable range hopping.

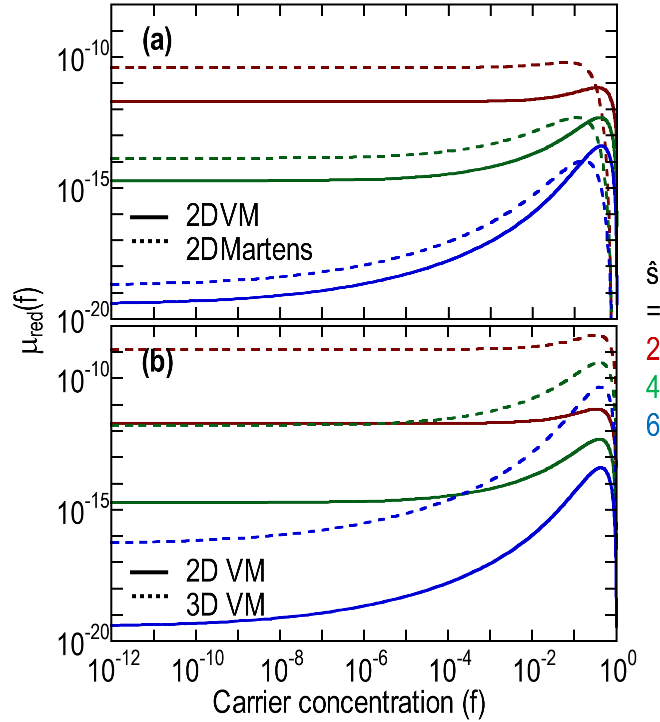

Figure 2.3 Calculated carrier concentration (f) dependent reduced mobility $\mu_{red}(f)$ results. (a) $\mu_{red}(f)$ by 2D VM model and 2D Martens model with Gaussian DOS and $N_t/\alpha^2 = 10^{-2}$. (b) $\mu_{red}(f)$ by 2D and 3D VM models with Gaussian DOS and $N_t/\alpha^2 = 10^{-2}$ for 2D, $N_t/\alpha^3 = 10^{-3}$ for 3D respectively.

Figure 2.4a&b show the calculated R^* and E^* from 2D Martens model respectively at $N_t/\alpha^2 = 10^{-2}$ and different carrier concentrations. E^* decreases with temperature while R^* increases with it. Both are nearly carrier concentration independent when E_F/σ is below −1 i.e. when f is low. This is valid for R^* at all site densities as shown in Fig. 2.4c, but becomes invalid for E^* when $N_t/\alpha^2 > 10^{-2}$ i.e. high site density as shown in Fig. 2.4d. So in the low carrier concentration and low site density range, both E^* and R^* are independent of carrier concentration. According to Martens model, the carrier concentration dependent reduced mobility $\mu_{red}(f)$ can be written as $\gamma exp(E_F/k_BT)/f$,

where γ is a constant while $\mu_{red}(0) = \gamma exp(-\hat{s}^2/2)$. The ratio between carrier concentration dependent reduced mobility $\mu(f)$ and mobility at zero-concentration limit $\mu(0)$ is:

$$\frac{\mu(f)}{\mu(0)} \cong \frac{1}{f}\exp(\frac{E_F(f)}{k_B T}+\frac{1}{2}\hat{s}^2) \quad (2.10)$$

In the previous section, $\mu(0) = \mu_0 exp(-p(0))$, $\mu_0 = \sigma_0/N_t e$ and $p(0) = p_0 + a\hat{s} + b\hat{s}^2$. Thus $\mu(f)$ in 2D is given by this equation:

$$\mu_{2D}(f) = \frac{ev_0}{N_t^{1/2}k_B T}\Phi\exp(-p_0 - \ln c - (a - \frac{E_F}{\sigma_{DOS}})\hat{s} + (\frac{1}{2} - b)\hat{s}^2) \quad (2.11)$$

Where similarly Φ is a dimensionless factor to account for other mobility affecting macroscopic factors that are not included in this hopping transport model, p_0 equals to $(4B_c/\pi)^{1/2} * (N_t^{1/2}/\alpha)$ with $B_C = 4.5$, also the value of a and b can be taken from Table 2.1 for different site densities.

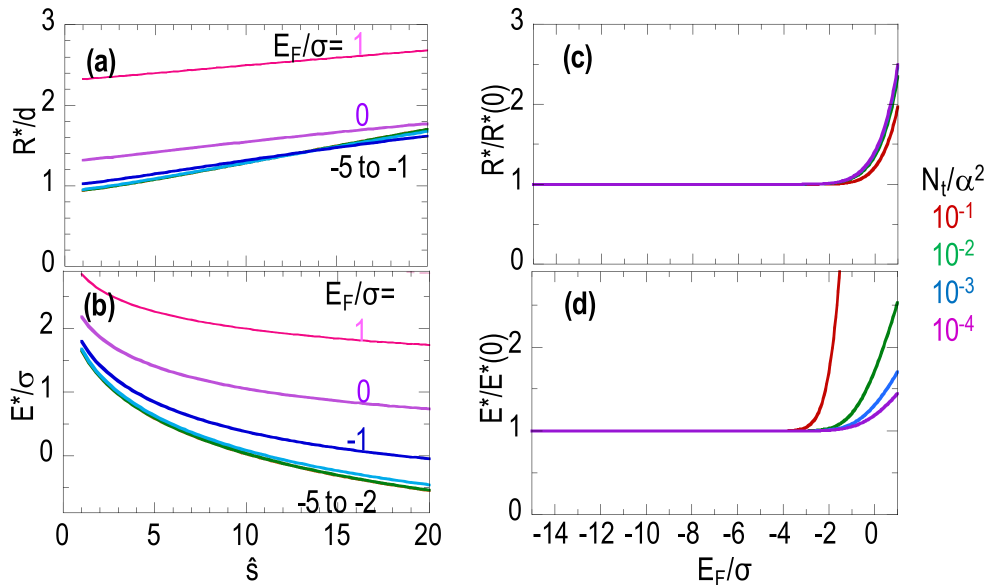

Figure 2.4 Calculated $R*$ and $E*$ at different Fermi levels (different carrier concentrations) by 2D Martens model with Gaussian DOS. (a)&(b) $R*$ in unit of average intersite distance and $E*$ in unit of DOS width respectively at $N_t/\alpha^2 = 10^{-2}$. (c)

Ratio of R^* to its value at zero-concentration limit $R^*(0)$ at different N_t/α^2. (d) Ratio of E^* to its value at zero-concentration limit $E^*(0)$ at different N_t/α^2.

Figure 2.5a show the $\mu_{red}(f)$ calculated from both the 2D VM model and Eqn. 2.11 at $N_t/\alpha^2 = 10^{-2}$. The two predict very similar charge transport behavior at low concentration range, while at the high carrier concentration range the two results start to deviate from each other especially at low temperature. The deviation is much more obvious at high site density as shown in Fig. 2.5b, where $\mu_{red}(f)$ predicted by the equation starts to increase when temperature decreases, indicating that the equation is no longer valid within this range. Overall, the analytical equation is a good approximation to describe hopping charge transport in system with and low carrier concentration and low site density.

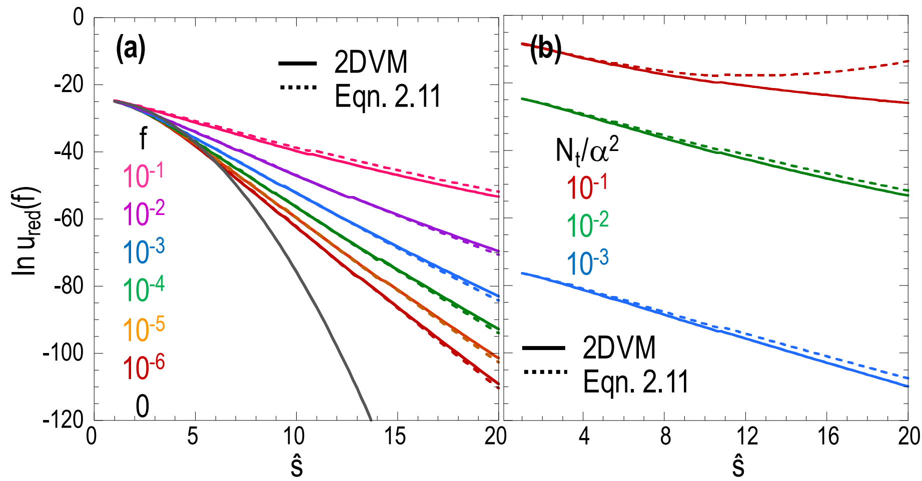

Figure 2.5 Comparison of $\mu_{red}(f)$ calculated by 2D VM model and by Eqn. 2.11 respectively with Gaussian DOS. (a) $\mu_{red}(f)$ at $N_t/\alpha^2 = 10^{-2}$, $a = 0.566$ and $b = 0.485$ used in the equation. (b) $\mu_{red}(f)$ at $f = 10^{-1}$, a and b are taken from Table 2.1 for corresponding N_t/α^2 .

2.4 Conclusion

In variable hopping system with Gaussian DOS, the charge transport behavior in 2D and 3D is similar while the charge carrier mobility in 2D is lower as a result of reduced dimensionality, which results in reduced neighboring site number and longer average hopping distance. The VM model and Martens model predict similar charge transport behavior in 2D and both models break down at relatively high carrier concentration region.

2.5 References

1 Coehoorn, R., Pasveer, W. F., Bobbert, P. A. & Michels, M. A. J. Charge-carrier concentration dependence of the hopping mobility in organic materials with Gaussian disorder. *Phys. Rev. B* **72**, 155206 (2005).

2 Chua, L. L., Friend, R. H. & Ho, P. K. H. Organic double-gate field-effect transistors: Logic-AND operation. *Appl. Phys. Lett.* **87**, 253512 (2005).

3 Demeyu, L., Stafstrom, S. & Bekele, M. Monte Carlo simulations of charge carrier mobility in semiconducting polymer field-effect transistors. *Phys. Rev. B* **76**, 155202 (2007).

4 Tanase, C., Meijer, E. J., Blom, P. W. M. & de Leeuw, D. M. Unification of the hole transport in polymeric field-effect transistors and light-emitting diodes. *Phys. Rev. Lett.* **91**, 216601 (2003).

5 Vissenberg, M. & Matters, M. Theory of the field-effect mobility in amorphous organic transistors. *Phys. Rev. B* **57**, 12964 (1998).

6 Salleo, A. *et al.* Intrinsic hole mobility and trapping in a regioregular poly(thiophene). *Phys. Rev. B* **70**, 115311 (2004).

7 Pasveer, W. F. *et al.* Unified description of charge-carrier mobilities in disordered semiconducting polymers. *Phys. Rev. Lett.* **94**, 206601 (2005).

8 Dinelli, F. *et al.* Spatially correlated charge transport in organic thin film transistors. *Phys. Rev. Lett.* **92**, 116802 (2004).

9 Shehu, A. *et al.* Layered distribution of charge carriers in organic thin film transistors. *Phys. Rev. Lett.* **104**, 246602 (2010).

10 Sandberg, H. G. O. *et al.* Ultrathin regioregular poly(3-hexyl thiophene) field-effect transistors. *Langmuir* **18**, 10176 (2002).

11 Fabiano, S. *et al.* From monolayer to multilayer n-channel polymeric field-effect transistors with precise conformational order. *Adv. Mater.* **24**, 951 (2012).

12 Himmelberger, S. *et al.* Effects of confinement on microstructure and charge transport in high performance semicrystalline polymer semiconductors. *Adv. Funct. Mater.* **23**, 2091 (2013).

13 Sharma, A., van Oost, F. W. A., Kemerink, M. & Bobbert, P. A. Dimensionality of charge transport in organic field-effect transistors. *Phys. Rev. B* **85**, 235302 (2012).

14 Smits, E. C. P. *et al.* Bottom-up organic integrated circuits. *Nature* **455**, 956 (2008).

15 Wang, C. C. *et al.* Microstructural origin of high mobility in high-performance poly(thieno-thiophene) thin-film transistors. *Adv. Mater.* **22**, 697 (2010).

16 Emelianova, E. V., van der Auweraer, M., Adriaenssens, G. J. & Stesmans, A. Carrier mobility in two-dimensional disordered hopping systems. *Org. Electron.* **9**, 129 (2008).

17 Brondijk, J. J. *et al.* Two-dimensional charge transport in disordered organic semiconductors. *Phys. Rev. Lett.* **109**, 056601 (2012).

18 Miller, A. & Abrahams, E. Impurity conduction at low concentrations. *Phys. Rev.* **120**, 745 (1960).

19 Martens, H. C. F. *et al.* Understanding the doping dependence of the conductivity of conjugated polymers: Dominant role of the increasing density of states and growing delocalization. *Phys. Rev. B* **67**, 121203 (2003).

20 Pike, G. E. & Seager, C. H. Percolation and conductivity - computer study. 1. *Phys. Rev. B* **10**, 1421 (1974).

21 Mott, N. F. Conduction in non-crystalline materials. 3. Localized states in a pseudogap and near extremities of conduction and valence bands. *Philos. Mag.* **19**, 835 (1969).

Chapter 3. Universal charge transport model for OFETs

In this chapter, we develop an "universal" two-dimensional charge transport model for field-effect transistors. We show that by coarse-graining the transport sites in the polymer film, the anisotropic transport along polymer chain and in π-stacking direction could be modeled as hopping in a cross lattice in αR space with αR defining the interchain coupling strength. This transport DOS at π-band edge could be modeled by simple analytical functions such as Gaussians or sum-of-Gaussians, or treated as a numerical function, and the site density N_t inside transport DOS is coupled to its width σ. Finally the mobility-carrier density-temperature $\mu(c, T)$ surface is calculated using Miller-Abrahams (MA) hopping rate, resistor network approach and percolation method. With Gaussian DOS, the calculated results show the variable range hopping feature of charge transport with extended hopping distances at low temperatures. Also the calculated $\mu(c, T)$ surface could be modulated in large range by model parameters $\langle \alpha d \rangle$ and σ. We show it is possible to simulate the entire $\mu(c, T)$ surface with only these three parameters: the transport DOS tail shape, the interchain coupling parameter and the connectivity parameter ξ which measures the macroscopic transport "connectivity" across the channel region,

3.1 Introduction

The physics of charge transport in organic semiconductors remains an active area of research because of the complex nature of these materials. The lack of a widely applicable approach to investigate their transport DOS hampers efforts to understand the central structure–morphology−property relations of these materials. The performance of solution-processed OFETs has improved sufficiently in recent years as a result of the emergence of new materials and better control that they now appear very attractive for technological applications[1-5] thus it is now imperative to reexamine our state of understanding of the structure−morphology−property relations of these materials.

There are presently two main families of charge transport models, the disorder model and the mobility edge model, differing in their emphasis of disorder as the primary or secondary feature respectively.[6-9] A variety of experimental work including structural investigations suggests that solution-processed polymer semiconductors have a significant level of underlying disorder, even in the presence of lamellar stacking, and so disorder models are the natural starting viewpoint.[10-12] Bässler et al.[13] developed the archetypal Gaussian Disorder Model (GDM) in which carriers are considered to hop in a Gaussian DOS in Monte-Carlo simulations, which reveals that carrier mobility has a non-Arrhenius temperature dependence, $\mu(T) \propto \exp(-9\hat{s}^2/4)$, where $\hat{s} = \sigma/k_BT$, σ is the width of the DOS, k_B is Boltzmann constant and T is the temperature. Later this model was extended to include the mobility dependence on carrier concentration in the Extended Gaussian Disorder Model (EGDM),[14] which could be simplified to yield analytical solutions for an assumed exponential DOS in a percolating resistor−network formalism (the Vissenberg−Matters model)[15] to describe transport in organic field-effect

transistors (OFETs), or for assumed Gaussian DOS (the Coehoorn model)[16,17] to describe transport in organic light emitting diodes (OLEDs). The model could only fit limited temperature T and carrier density c ranges in the $\mu_{FET}(c,\ T)$[18,19] The key insights afforded by these models include the "transport level" where carriers have to typically reach in their hopping transport, the interplay between energetic disorder and long-range orbital coupling which promotes variable-range hopping particularly at low temperatures. However the chief disadvantage is that the DOS shapes in these models are fixed *a priori* by simplifying assumptions which may severely limit their general applicability to dielectric−semiconductor interfaces, and more crucially the ability to extract vital structure−morphology−property relations.

3.2 Model development

OFETs are characterized during operation by a high charge-carrier density of the order of 10^{12} cm^{-2} accumulated in a region of monolayer thickness at the semiconductor−dielectric interface.[20] Therefore we sought to develop a 2D transport model based on the Coehoorn model[16] as the starting point. We adopted a number of assumptions that have been customary in the field, but we provide further justifications here.

3.2.1 Density-of-states

The integrated π-electron density (in units of cm^{-2}) of the monolayer is known *a priori* from crystal structure and molecular packing at the interface. These π electrons are energetically distributed over a fairly wide occupied π molecular orbital (MO) band,

which is sometimes called the π valence band (≈ 8 eV wide from quantum chemical calculations). Examples of the computed DOS distributions for a family of oligothiophenes are shown in Fig. 3.1a, and an example ultraviolet photoemission spectrum is shown in Fig. 3.1b. The energy-integrated DOS of the π band N_o is *a priori* known from the molecular structure of the organic semiconductor and its packing density. Typically, the DOS distribution is more-or-less flat over the central portion of the band with relatively sharply defined edges. These edges should become broadened by thermal or other sources of disorder. A step-like Heaviside edge convoluted with Gaussian of width σ_{dis} (standard deviation) gives a tail that is well modeled (see appendix A) by a Gaussian of width $\sigma = 1.13\ \sigma_{dis}$ and a height of 0.913 h_o where h_o is the Heaviside function height, as shown in Fig. 3.1c.

The injection of holes into this band causes holes to accumulate in the frontier region (i.e., high-energy edge) of the band. For typical DOS and carrier densities encountered in FETs, the Fermi level E_F lies well inside the band tail (see Fig. 3.4). Conversely the injection of electrons into the unoccupied π MO band called the π conduction band causes electrons to accumulate in the band tail. To avoid repetition, we describe below only the situation for holes. The situation for electrons is exactly analogous.

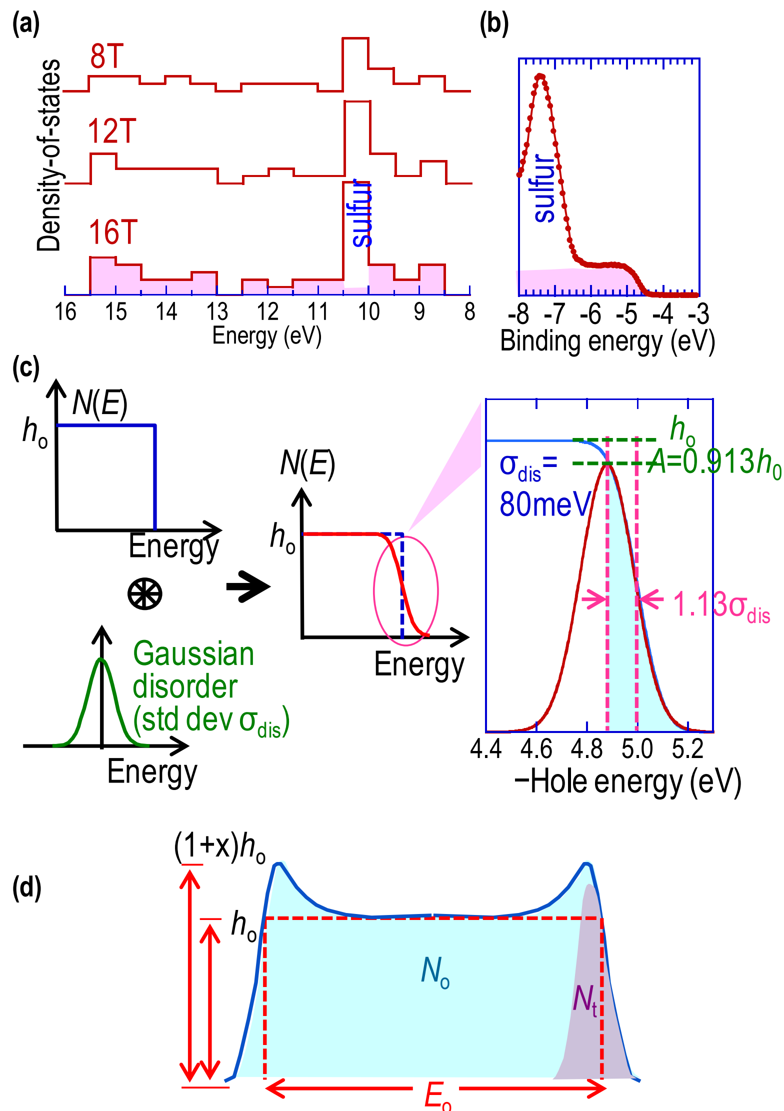

Figure 3.1 Transport Density of States (tDOS) in polymer semiconductors. (a) Calculated π-band for oligothiophene with 8, 12 and 16 thiophene units, indicated by area under curve (excluding sulfur peak). (b) Edge of rrP3HT π-band (pink shaded area) measured by UPS. (c) Convolution of uniform DOS (height h_0) with Gaussian disorder σ_{dis} gives broadened tail at the edge, which is well fitted by single Gaussian with $\sigma = 1.13\sigma_{dis}$ and peak height $A = 0.913h_0$. (d) Illustration of π-band (green region under curve) with width E_0, and the transport DOS (pink region) at π-band edge.

Only those states that fall in a narrow energy range from just below the Fermi level E_F up to just above the transport level is relevant to transport of the accumulated holes in OFETs. This gives the critical section of the DOS that is relevant to transport. It is

only a tiny slice of the entire DOS. This transport DOS can be modeled by simple analytical functions such as Gaussians or sum-of-Gaussians, or treated as a numerical function. The total number of sites N_t included in this model DOS shape depends on the model itself, which is known *a priori* and often a small fraction of the total available π electron states. For the case of the DOS shape given in Fig. 3.1d, where the frontier edge is Gaussian-like, N_t is proportional to σ, and related to N_o by the equation $\frac{N_t}{N_o} = \frac{A}{h_o} \cdot \frac{\sqrt{2\pi} \cdot \sigma}{E_o + \sqrt{2\pi} \cdot \sigma_1 \cdot x}$, where σ is the effective Gaussian width of the modeled DOS, x and σ_1 respectively are the relative height and width of the DOS pileup if any at the edge, and the meanings of the other terms are given in the figure. Typically, σ_1 is of the order of 0.1 eV which is << E_o, and x is also around 1 or smaller for the materials of interest here. Hence the $\sigma_1 x$ term can be neglected.

3.2.2 Hopping sites

Hopping transport within the polymer OSC monolayer can then be treated as hopping of charge carriers between more or less localized “sites” in the presence of site energetic disorder and intersite coupling variation (Fig. 3.2a). The sites refer to the effective transport sites discussed earlier, marked here by red dots decorating the polymer chains. Their total density is given by N_t. The exact location of these sites is not important for macroscopic transport analysis. Only their density and their intersite coupling determines transport behavior.

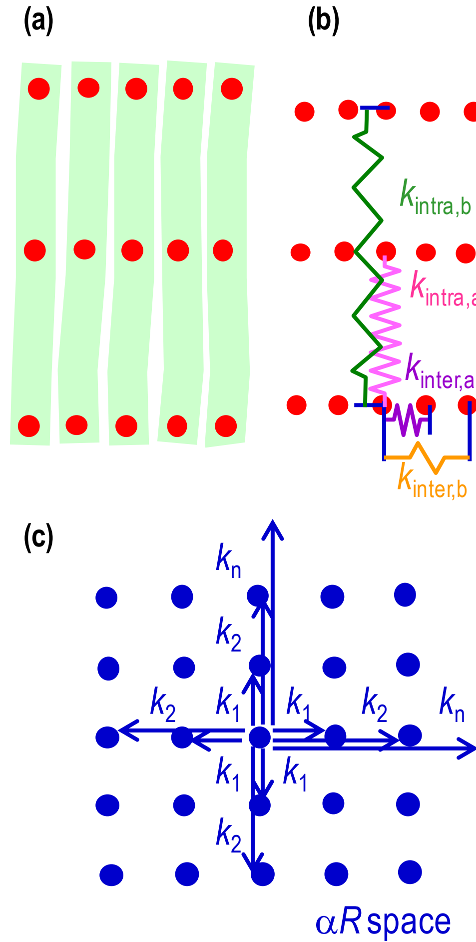

Figure 3.2 Hopping transport in a cross lattice (αR space) in polymer semiconductors. (a) A simplified view of polymer chains (green) and hopping sites (red) in the π-aggregation, longer interval between sites along the polymer chain comes from longer delocalization length of π electron wavefunction in that direction. (b) Illustration of stronger inter-site coupling in the intrachain hopping paths k_{intra} than in interchain hopping paths k_{inter}, The coupling strength is represented by peak numbers. (c) The basic picture of hopping transport in αR space, in which transport sites form square lattice. Only hops along the polymer chain and in the π-stacking directions are allowed as indicated by hopping paths k_1, k_2 ...

A key challenge to the analysis is the chains are highly anisotropic with a large electronic bandwidth along the chain but a small bandwidth between chains. This causes the effective coupling strength in the interchain direction to be considerably smaller than in the intrachain direction, i.e., $\alpha_{inter,a} >> \alpha_{intra,a}$ since the coupling strength is proportional to the delocalization length of wavefunction ($1/\alpha$) (Fig. 3.2b). Transfer integral calculations suggest that tunneling rate has the approximate

exp($-\alpha R$) dependence in both these directions, albeit with $\alpha_{inter} >> \alpha_{intra}$. This suggests that the transport analysis can be greatly simplified through coarse-graining by treating the intrachain sites within a length L, where $exp(-\alpha_{intra}L) = exp(-\alpha_{inter}d)$, and d is the interchain distance, together as a single "super" site. The justification for this is the carrier can explore L along the chain during the time it takes to make an interchain hop. The effect of this is to reduce the apparent energetic disorder and improve intersite coupling between chains, since the carrier can explore the "best link". Furthermore, these hops can occur to the nearest neighbor (e.g., $k_{inter,a}$ and $k_{intra,a}$) or to further neighbors (e.g., $k_{inter,b}$ and $k_{intra,b}$) depending on energy difference and intersite coupling (Fig. 3.2b).

This coarse-graining procedure then allows us to redraw the transport connectivity diagram as a square lattice in αR space characterized by a single average $<\alpha d>$ (Fig. 3.2c). This greatly simplifies the evaluation of mobility through the percolating resistor network problem. The blue dots represent the reduced sites for the purpose of mobility evaluation through percolation theory. The hops from any origin are now represented by $k_{1,}$ k_2,... Note however in this model that the allowed hops are limited to interchain and intrachain directions which are along the directions of the two primitive lattice vectors. Diagonal hops are not allowed.

3.2.3 Intersite hopping rate

We followed Coehoorn et al.[16] to compute the probability distribution function of the intersite conductance G_{ij}' for the test DOS with uncorrelated energetic disorder and the test αd_o distribution, for a given carrier density. If there was in fact energetic correlation between sites, the assumption of no correlation causes a narrowing of the

effective transport DOS width. We assumed the hopping rate is given by Abrahams−Miller (MA) equation:[21]

$$w_{ij} = \begin{cases} \nu_0 \exp(-2\alpha R_{ij} - \dfrac{\varepsilon_i - \varepsilon_j}{k_B T}) & \varepsilon_j < \varepsilon_i \\ \nu_0 \exp(-2\alpha R_{ij}) & \varepsilon_j \geq \varepsilon_i \end{cases} \quad (3.1)$$

where w_{ij} is the hopping rate from site j to i, ν_0 is the attempt frequency, R_{ij} is the distance between sites i and j, ε_i and ε_j are the site energies whose values are taken from the model transport DOS distribution, and α is the intersite coupling parameter assumed to follow a uniform distribution on the interval $\alpha_0[1-\alpha_w, 1+\alpha_w]$ to allow for variability in coupling strength and intersite distance.

Detailed simulation of electron transfer in the Franck−Condon approximation shows the form of W_{ij} changes from Marcus behavior in the limit of small vibronic coupling (i.e., small Huang−Rhys factor) which is in the classical region, to Abrahams−Miller behavior in the limit of large vibronic coupling (i.e., large Huang-Rhys factor) between the initial and final states following electron transfer.[22] Since there is strong vibronic coupling in polymer organic semiconductors, the MA equation and not the Marcus equation provides the more appropriate description of the hopping rate.

3.2.4 Intersite conductance and carrier mobility

Assuming thermal equilibrium of the charge carriers, the site occupational probability is given by the Fermi-Dirac distribution. Then the conductance G_{ij} between sites i and j is given by:

$$G_{ij} = \frac{e^2 \nu_0}{2k_B T} \exp(-2\alpha R_{ij} - \frac{|\varepsilon_i - \varepsilon_j|}{2k_B T}) / \cosh(\frac{\varepsilon_i - E_F}{2k_B T}) \cosh(\frac{\varepsilon_j - E_F}{2k_B T}) \quad (3.2)$$

where E_F is Fermi level of the system which depends on the DOS, carrier concentration c and temperature T; and ν_0 is the phenomenological hopping attempt frequency. We can expect this to be given by the dominant phonon−electron lattice mode (≈ 1500 cm^{-1}, measured in Raman spectroscopy). Following Coehoorn, we define a reduced conductance G_{ij}' implicitly according to $G_{ij} = (e^2\nu_0 / k_B T) G_{ij}'$, where G_{ij}' is the dimensionless conductance. For the model DOS shape and assumed αR distribution, and given c and T, we obtained the G_{ij}' distribution for hops to different neighboring sites by taking a large sample (of the order of 10^8) of ε_i, ε_j and αR.

The conductance G_c of the resistor network was then evaluated in the framework of percolation theory as the threshold G_{ij} where the cumulative number of hops with conductance larger than G_c, from each site, exceeds the bond percolation parameter B_c. For a square lattice with nearest-neighbor hopping, $B_c = 2$ exactly. For an array of randomly distributed point sites in 2D, $B_c \approx 4.5$, which is larger than 2 because of the increased probability for formation of closed clusters.[23] For the extended-range hops in our model, B_c is not explicitly known but likely to be just slightly larger than 2. G_c is determined by the condition $H(G_{ij} > G_c) = \sum_{G_{ij} > G_c} \sum_j P_j(G_{ij}) = B_c$, where $P_j(G_{ij})$ is the probability of a hop to the jth site that occurs at conductance G_{ij}, normalised to a log conductance interval. We give the distribution in $\log(G_{ij})$ because G_{ij} spans many orders of magnitude.

The conductivity of the system σ_c is given by G_c. Hence the carrier mobility μ is given by:

$$\mu = \frac{1}{e \cdot c} G_c = \frac{e \cdot \nu_o}{f \cdot N_t \cdot k_B \cdot T} G_c' \quad (3.3)$$

where N_t is the effective total transport site density, c is the 2D carrier density, and f is the fractional occupation of N_t that gives c. Since the comparison with experiment is undertaken on the log scale to understand behavior spanning several decades, we write:

$$\log(\mu) = \log(\frac{e \cdot \nu_o}{N_t \cdot k_B}) + \log(\xi) + \log(G_c')\log(\frac{1}{f}) + \log(\frac{1}{T}) \quad (3.4)$$

where we have now introduced an additional temperature and carrier-density independent parameter ξ to capture (i) a numerical factor of order unity in the evaluation of G_c', (ii) another factor of order unity to transform the model DOS site density N_t to the apparent site density required in G_c', and (iii) a "connectivity" factor ≤ 1 to capture the notion that the actual conduction channel may be a fraction of the geometric channel area of the FET due to the presence of severe disorder or other effects which act as hard boundaries to the field-effect current.

The last three terms on the right-hand side contain the essential temperature and carrier density dependences of μ which we wish to understand. We denote the sum of these terms as log μ'. The behavior of log μ' completely determines the shape of the log μ' surface on (c, T). The first two terms then together shift the computed log μ' surface on rigidly to match the experimentally-measured surface. If ν_o is known or otherwise assumed, ξ can be unambiguously determined.

μ can be written as $ln\mu = ln\mu' + cc$, cc is proportional to ev_0/k_BN_t and $\ln \mu' = \ln G_c' + \ln(1/T) - \ln c$.

3.3 Results and discussion

3.3.1 Variable-range hopping

Figure 3.3c shows representative $P_j(G_{ij})$ *vs* $log(G_{ij})$ histogram distributions (class interval, 0.25) plotted for $\hat{s} = 3$ and $\hat{s} = 12$, where $\hat{s} = \sigma / k_B T$, for $j = 1$, 3, 5, 7 and 9. The site energies are drawn from Gaussian distributions. The $\alpha_0 R$ values are taken from a uniform distribution with $\alpha_0 d = 0.85$, $\alpha_w = 0.06$ as shown in Fig. 3.3b. The selected $\hat{s}$ corresponds to 295 K and 77 K respectively for $\sigma \approx 90$ meV. This illustrates the typical transport behaviour at room temperature and at low temperature. The carrier fractional occupation is $p \approx 4.5$ %, which are typical values for OFETs in the usual accumulation mode operation (vide infra).

The results show that near room temperature, hopping is dominated by nearest-neighbour hopping with a small contribution from next-few-nearest neighbour hopping up to $j = 4$. There is generally enough thermal energy to overcome the site energy differences between the nearest neighbouring sites. At low temperatures however, the thermal energy is too small to allow significant up-energy hops. Thus carriers are forced to hop over to more distant sites which have the appropriate energies. This leads to a much larger contribution from extended-range hops, up to $j = 9$ here. Therefore macroscopic transport in this model is expected to be characterised by variable-range hopping for typical system parameters.

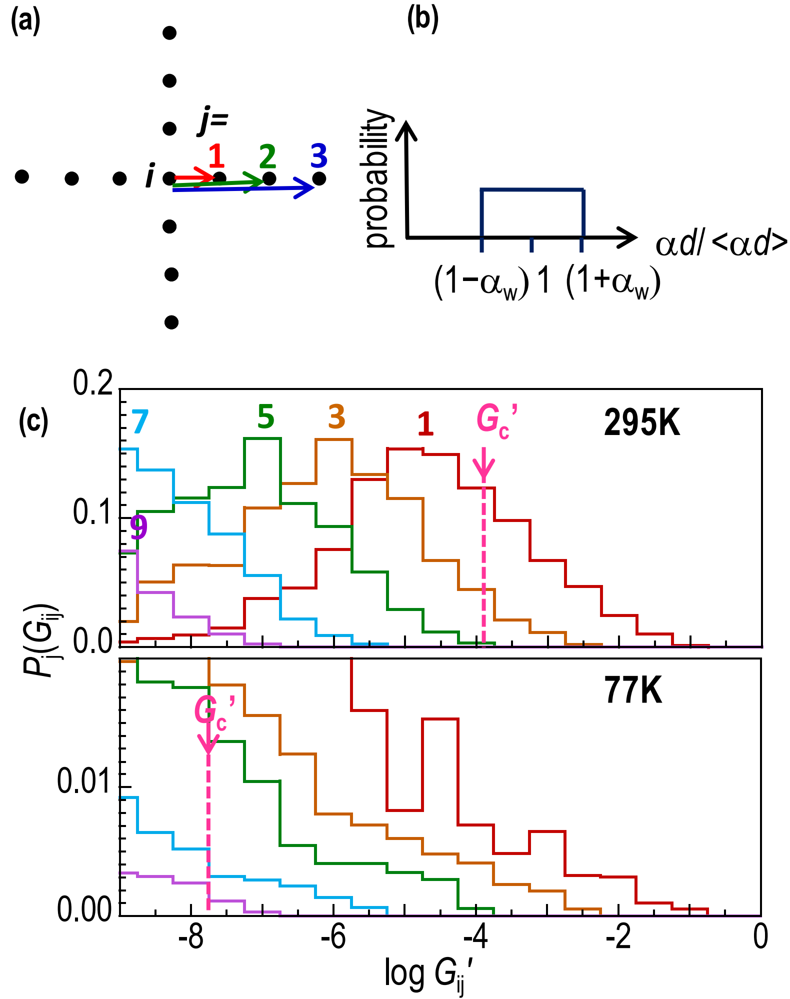

Figure 3.3 Variable-range hopping in polymer semiconductors. (a) Illustration of hopping to n^{th} neighbors in αR space. (b) Uniform distribution of αd in Miller-Abrahams hopping rate equation, d is the π-stacking distance. (c) Distribution of reduced conductance G_{ij}' to n^{th} neighbor at 295 K and 77 K under Gaussian DOS with σ = 90 meV and αd distribution with <αd> = 0.85 and α_w = 0.06. The reduced conductance G_c' of the resistor network is determined by using bond percolation number $B_c = 2$.

To test the sensitivity of the model to the morphology of the lattice morphology, we examined the results for a hopping in a square lattice with identical input parameters (see appendix D). The only difference is the diagonal hops are now allowed. The effect at room temperature is negligible (logG_c': square lattice, −3.80; cross lattice, −3.86). This is a consequence of the dominance of nearest-neighbor hopping. At low temperatures however (77 K), a difference emerges. The square lattice offers a higher

G_c' than the cross lattice (logG_c': square lattice, −6.98; cross lattice, −7.77). This difference amounts to an increase in carrier mobility in the square lattice by a factor of 6 over the cross lattice, which is relatively small on the log scale on which temperature dependence of the mobility is often plotted. The higher mobility in the square lattice arises from the emergence of increasingly larger number of off-axis sites for diagonal hops as the hopping range becomes larger. This characteristic of a square lattice does not appear to be physically meaningful in conjugated polymers and oligomers. Nevertheless, the results suggest that the use of a square lattice model introduces an error only at low temperatures where extended-range hopping dominates.

3.3.2 Effect of distributed αd

Detailed simulations further show that the results are relatively insensitive to the width of the αd distribution centered at $<\alpha d>$, i.e. uniform distribution on the interval [$(1 - \alpha_w)* <\alpha d>$, $(1 + \alpha_w)* <\alpha d>$], for realistic α_w values between zero and 0.5. A α_w value of zero corresponds to the case of a delta distribution at $<\alpha d>$, while $\alpha_w = 0.5$ corresponds to a uniform distribution on the interval [$0.5*<\alpha d>$, $1.5*<\alpha d>$] (Fig. 3.3b). For the rest of the paper, we therefore fixed α_w at 0.065.

3.3.3 Transport level

With Gaussian transport DOS and $<\alpha d> = 1.0$, figure 3.4 shows the calculated Fermi level E_F, activation energy E_A and transport level E_T for a broad range of (c, σ) points at 295 K and 77 K respectively. The three values are related by the equation $E_F + E_A = E_T$. The results show that E_F is at the DOS tail and E_T is below the DOS center

under all conditions, therefore it is valid to use simple analytical functions such as Gaussians or sum-of-Gaussians, or treated as a numerical function to model the transport DOS.

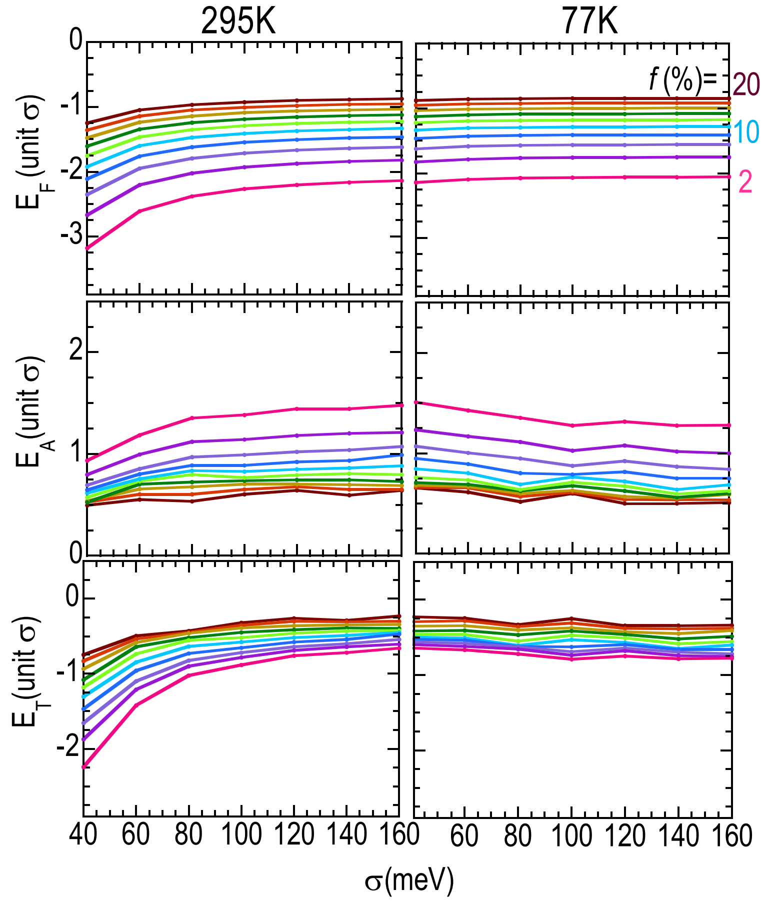

Figure 3.4 Calculated Fermi level (E_F), Activation energy (E_A) of mobility and Transport level (E_T) at different carrier concentrations ($f = 2 - 20\%$, interval 2%) with Gaussian DOS (width σ) and <αd> = 1.0.

3.3.4 Significance of this approach

This transport model has only a very small number of adjustable parameters with distinct physical meanings: (i) the transport DOS edge itself where the field-induced carriers reside, (ii) interchain coupling parameter <αd> for carrier hopping, and (iii) ξ which measures the macroscopic transport "connectivity" across the channel region.

Detailed simulations have revealed that these parameters are substantially decoupled and can thus be reliably evaluated from carrier mobility measurements provided a wide span of the $\mu(c, T)$ surface is used. It is clear that ξ is a carrier-density and temperature-independent shift factor that rigidly shifts the computed $\mu(c, T)$ surface without altering its local surface gradients. On the other hand both the transport DOS shape (width parameter σ) and interchain coupling parameter determine the temperature and carrier-density dependences of μ but in different ways that allows each of them to be reliably evaluated. The σ parameter determines these characteristics through the energetic disorder present, but the $<\alpha d>$ parameter does so as a consequence of a change in the hopping range. Figure 3.5 shows for example that as σ increases at constant $<\alpha d>$, both the temperature and carrier-density dependences of μ increase simultaneously. However as $<\alpha d>$ increases at constant σ, the primary impact on μ is its temperature dependence.

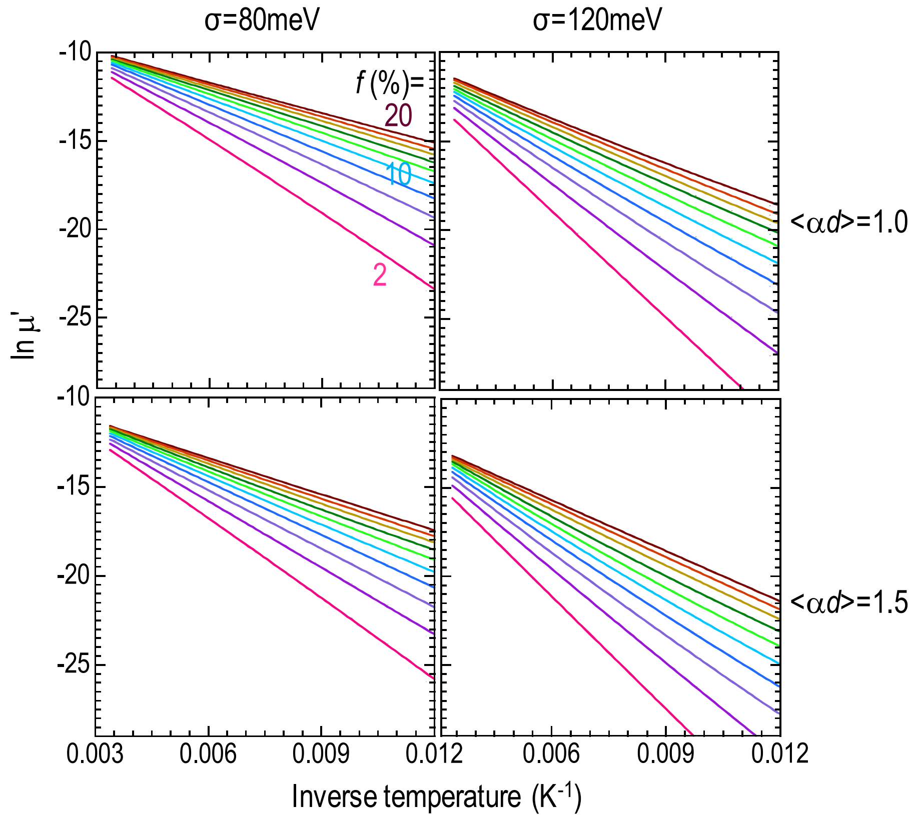

Figure 3.5 Calculated reduced mobility μ' with Gaussian DOS.

If this effort to simulate the entire $\mu(c, T)$ surface using only these three fundamental "global" parameters is successful, we can be conclude that variable-range-hopping at the macroscopic level provides an appropriate basis to quantitatively understand field-induced transport in these materials. Furthermore the properties of different polymer semiconductor/ dielectric interfaces can then be reduced to the three fundamental parameters that govern transport in this model, the transport DOS tail shape, the interchain coupling parameter and the connectivity parameter. This will provide a significant step forward to understand the essential role of disorder and its dependence on various key aspects of polymer organic semiconductor materials and devices, such as molecular weight and its distribution, processing conditions, and different gate dielectrics.

3.5 Conclusion

We have developed a self-consistent 2D variable-range hopping model for organic field -effect transistors. In this model, the anisotropic transport along polymer chain and in π-stacking direction could be modeled as hopping in a cross lattice; this transport DOS at π-band edge could be modeled by simple analytical functions such as Gaussians or sum-of-Gaussians, or treated as a numerical function, and the site density inside transport DOS is related to its width; The mobility-carrier concentration-temperature $\mu(c, T)$ surface is calculated using Miller-Abrahams (MA) hopping rate, resistor network approach and percolation method. We show it is possible to simulate the entire $\mu(c, T)$ surface with only these three parameters: the transport DOS tail shape, the interchain coupling parameter and the connectivity parameter ξ which measures the macroscopic transport "connectivity" across the channel region.

3.6 References

1 Liu, S. H., Wang, W. C. M., Briseno, A. L., Mannsfeld, S. C. E. & Bao, Z. N. Controlled deposition of crystalline organic semiconductors for field-effect-transistor applications. *Adv. Mater.* **21**, 1217 (2009).

2 Arias, A. C., MacKenzie, J. D., McCulloch, I., Rivnay, J. & Salleo, A. Materials and Applications for Large Area Electronics: Solution-Based Approaches. *Chem. Rev.* **110**, 3 (2010).

3 Wen, Y. G., Liu, Y. Q., Guo, Y. L., Yu, G. & Hu, W. P. Experimental Techniques for the Fabrication and Characterization of Organic Thin Films for Field-Effect Transistors. *Chem. Rev.* **111**, 3358 (2011).

4 Nielsen, C. B., Turbiez, M. & McCulloch, I. Recent advances in the development of semiconducting DPP-containing polymers for transistor applications. *Adv. Mater.* **25**, 1859 (2013).

5 Sirringhaus, H. 25th Anniversary Article: Organic Field-Effect Transistors: The Path Beyond Amorphous Silicon. *Adv. Mater.* **26**, 1319 (2014).

6 Street, R. A., Northrup, J. E. & Salleo, A. Transport in polycrystalline polymer thin-film Transistors. *Phys. Rev. B* **71**, 165202 (2005).

7 Coropceanu, V. *et al.* Charge transport in organic semiconductors. *Chem. Rev.* **107**, 926 (2007).

8 Tessler, N., Preezant, Y., Rappaport, N. & Roichman, Y. Charge transport in disordered organic materials and its relevance to thin-film devices: A tutorial review. *Adv. Mater.* **21**, 2741 (2009).

9 Bässler, H. & Kohler, A. in *Unimolecular and Supramolecular Electronics I: Chemistry and Physics Meet at Metal-Molecule Interfaces* Vol. 312 *Topics in Current Chemistry* 1-65 (2012).

10 Rivnay, J., Noriega, R., Kline, R. J., Salleo, A. & Toney, M. F. Quantitative analysis of lattice disorder and crystallite size in organic semiconductor thin films. *Phys. Rev. B* **84**, 045203 (2011).

11 Rivnay, J., Mannsfeld, S. C. B., Miller, C. E., Salleo, A. & Toney, M. F. Quantitative determination of organic semiconductor microstructure from the molecular to device scale. *Chem. Rev.* **112**, 5488 (2012).

12 Noriega, R. *et al.* A general relationship between disorder, aggregation and charge transport in conjugated polymers. *Nat. Mater.* (2013).

13 Bässler, H. Charge transport in disordered organic photoconductors - a monte-carlo simulation study. *Phys. Status Solidi B* **175**, 15 (1993).

14 Tanase, C., Meijer, E. J., Blom, P. W. M. & de Leeuw, D. M. Unification of the hole transport in polymeric field-effect transistors and light-emitting diodes. *Phys. Rev. Lett.* **91**, 216601 (2003).

15 Vissenberg, M. & Matters, M. Theory of the field-effect mobility in amorphous organic transistors. *Phys. Rev. B* **57**, 12964-12967 (1998).

16 Coehoorn, R., Pasveer, W. F., Bobbert, P. A. & Michels, M. A. J. Charge-carrier concentration dependence of the hopping mobility in organic materials with Gaussian disorder. *Phys. Rev. B* **72**, 155206 (2005).

17 Pasveer, W. F. *et al.* Unified description of charge-carrier mobilities in disordered semiconducting polymers. *Phys. Rev. Lett.* **94**, 206601 (2005).

18 Sirringhaus, H. Device physics of solution-processed organic Field-Effect Transistors. *Adv. Mater.* **17**, 2411 (2005).

19 Chang, J. F., Sirringhaus, H., Giles, M., Heeney, M. & McCulloch, I. Relative importance of polaron activation and disorder on charge transport in high-mobility conjugated polymer field-effect transistors. *Phys. Rev. B* **76** (2007).

20 Chua, L. L., Friend, R. H. & Ho, P. K. H. Organic double-gate field-effect transistors: Logic-AND operation. *Appl. Phys. Lett.* **87**, 253512 (2005).

21 Miller, A. & Abrahams, E. Impurity conduction at low concentrations. *Phys. Rev.* **120**, 745 (1960).

22 Png, R. Q. Private communication

23 Pike, G. E. & Seager, C. H. Percolation and conductivity - computer study. 1. *Phys. Rev. B* **10**, 1421 (1974).

Chapter 4. Effect of dielectric surface on the transport DOS of rrP3HT

In this chapter, we use regioregular poly(3-hexylthiophene) (rrP3HT) bottom-gate bottom-contact FETs to validate the new charge transport model developed in Chapter 3 and to study the effect of dielectric surfaces on the transport DOS. The different dielectric surfaces are made by doing surface treatments on SiO_2 with (a) Octadecyltrichlorosilane i.e. OTS; (b) 1H,1H,2H,2H-perfluorodecylsiloxy i.e. PDS; (c) Hexadimethylsilazane i.e. HMDS. The extracted $\mu(c,\ T)$ surface of FET device with OTS surface treatment is used for model validation since at this interface rrP3HT is known to form a relatively well-ordered layer, the transport DOS of which could be modeled by a hemi-Gaussian. This entire $\mu(c,\ T)$ surface can quantitatively reproduced with only transport DOS width, the interchain coupling and the connectivity parameter as fitting parameters. A temperature dependence of the transport DOS width is found in simulation, which is verified by variable-temperature ultraviolet photoemission spectroscopy (UPS) measurement. The other two dielectric surfaces i.e. the perfluoroalkyl- and TMS-SiO_2 give rise to a non-Gaussian tailing of the DOS and a depression of the connectivity parameter. Both these factors together completely account for the progressive degradation of the $\mu(c,\ T)$ characteristics across the channels, alkyl-SiO_2 > perfluoroalkyl-SiO_2 > TMS-SiO_2, for spin-on rrP3HT transistors. The results are consistent with the generation of shallow traps from the co-existence of a population of perturbed rrP3HT chain segments in the lying-down P3HT orientation.

4.1 Introduction

The device performance of bottom gated organic FETs are known to vary greatly depending on the gate material and its treatment before semiconductor deposition.[1,2] This dependence comes from two types of contributions: 1) properties of dielectric materials i.e. dielectric constant,[3-6] surface roughness,[7] surface chemical groups etc.[1,8] 2) semiconductor packing near the interface after deposition and annealing.[9] In order to get good device performance, the semiconductor is generally deposited on dielectric surface with low surface energy e.g. SiO_2 treated with certain self assembled monolayers (SAMs)[9,10] or oxygen plasma treated perfluoropolymers[11,12], followed with annealing to achieve optimal packing with lowest energy. The resulted packing at the bottom interface of semiconductor layer can be exposed by peeling off from dielectric surface[13] and characterized with X-ray techniques[14]. There remains question on whether the packing would remain the same when it is not in contact with the dielectric surface. Also it is impossible to peel off semiconductor films deposited on most dielectric surfaces as a result of strong interaction between them, making it very difficult to study the change in the semiconductor packing on different dielectric surfaces by experiment.

In this case one could choose to use computer simulation to get semiconductor packing structure under certain conditions and do comparison. This method is straightforward and its result is very easy to interpret, but currently the calculation is restricted to small sample size due to both software and practical limitations.[15,16] Nonetheless it would provide useful link between the semiconductor packing, electronic structure and its charge transport properties. In this consideration, it seems that charge transport model is the easiest way to explain the origin of the observed

differences, by fitting experiment current-voltage curves or $\mu_{FET}(c, T)$ curves to get transport DOS on the macroscopic level together with other useful information.[17-19] In current charge transport models, there exist several unpractical assumptions e.g. limitation of DOS shape to Gaussian or exponential, fixed width of localized wavefunction ect., that would comprise our understanding from the fitted results.

In this chapter, we will first validate our new charge transport model and then use it to study the effect of dielectric surface i.e. surface treatment in this particular case, by using regioregular poly(3-hexylthiophene) (rrP3HT) as our model material.

4.2 Experiment

As shown in Fig. 4.1, we made regioregular poly(3-hexylthiophene) (rrP3HT) bottom gate bottom contact FET devices with three different surface treatments at the semiconductor/SiO_2 interface, these surface treatments were made with (a) Octadecyltrichlorosilane i.e. OTS; (b) 1H,1H,2H,2H-perfluorodecylsiloxy i.e. PDS; (c) Hexadimethylsilazane i.e. HMDS. The FET channel length $L = 20$ μm and channel width $W = 22.5$ cm.

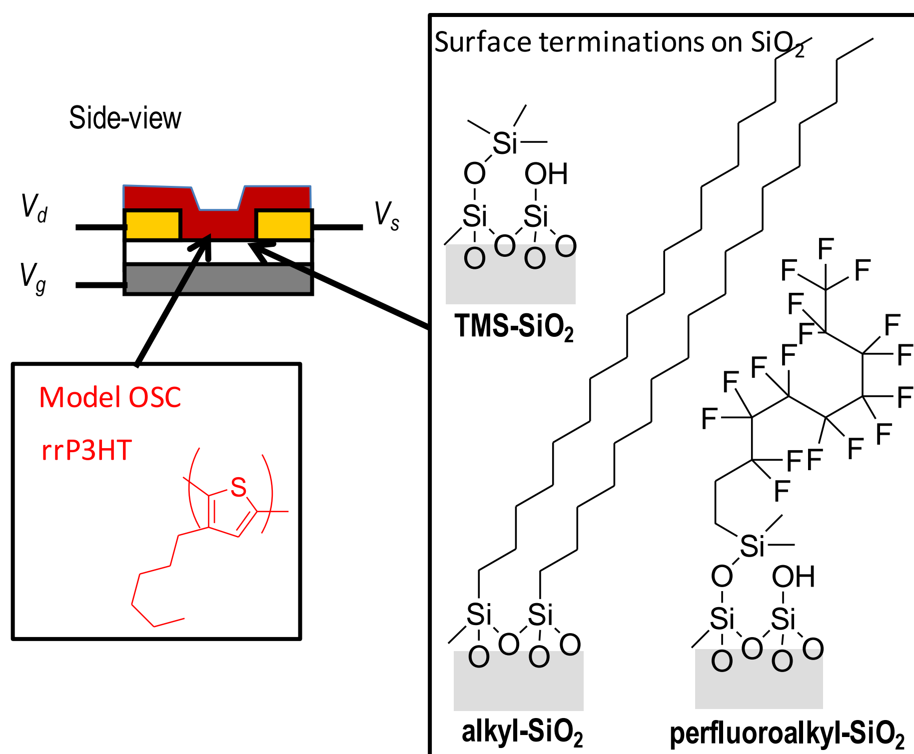

Figure 4.1 Schematic of BGBC FET structure, top to bottom: semiconductor (red), source-drain contacts (yellow), SiO_2 dielectric with surface treatment (white) and *p*-doped silicon gate (grey). The structure of rrP3HT is shown together with the three surface treatments on SiO_2.

Surface-treatment. Alkyl-surface modification: After oxygen-plasma treatment, SiO_2 surfaces were treated with octadecyltrichlorosilane in 0.1 mM solution (HPLC-grade toluene, without added H_2O, 25ºC; 2 h) in a N_2 glovebag to give a single monolayer, confirmed by variable-angle spectroscopic ellipsometry. The substrates were then rinsed thrice with clean toluene and annealed at 120°C (10 min; hotplate, N_2) to promote covalent bonding to the SiO_2 surface. The surface was then treated with refluxing HMDS vapor (1 atm; 120°C, 10 min) to terminate excess silanol groups in the tridentate SAM. **Perfluoroalkyl-surface modification:** As above but with 1*H*,1*H*,2*H*,2*H*-perfluorodecyldimethylchlorosilane as organosilane and without HMDS post-treatment since the organosilane is monodentate. **Trimethylsiloxy-surface modification:** After oxygen-plasma treatment, the SiO_2 surfaces were treated with refluxing HMDS vapor (1 atm; at 120°C, 10 min).

General. P3HT (>97% regioregular, nominal *Mn* = 17K; Sigma-Aldrich) was purified in-house by hydrazine reduction and flash chromatography to reduce unintentional doping to < 10^{17} cm^{-3}, and then dissolved in chlorobenzene in the glovebox. To "standardize" the π-stacking aggregation history, the polymer solution was heated to 85°C (15 min, isothermal well) in the glovebox and cooled to room temperature (15 min) just prior to spin-casting. The films were then annealed at 120°C (10 min, hotplate) to remove residual solvent. All processing steps were done in a N_2 glovebox (pO_2, H_2O < 1 ppm).

FETs. FETs were fabricated on 200 nm thermal SiO_2/p^{++}-Si with photo-lithographically defined 20 μm channel length and 225 mm channel width interdigitated Au souce-drain arrays. A layer of 50-nm thick P3HT was spin-cast from chlorobenzene solution after the respective SAM treatment.

Current–voltage characteristics were measured in a glovebox using a semiconductor characterization system (Keithley 4200). Variable-temperature FET measurements were carried out in a LakeShore TTP4 Probe Station kept at under 10^{-6} mbar and recorded by the Keithley 4200-SCS semiconductor parameter analyzer.

4.3 Results and discussion

4.3.1 Surface treatment induced difference in charge transport

From variable-temperature FET measurements, we extracted $\mu_{FET}(c, T)$ data for the three FET devices with alkyl, perfluoroalkyl, TMS treated SiO_2 dielectric respectively, as shown in Fig. 4.2. Both reduction of mobility and increase in activation energy are clearly observed in perfluoroalkyl, TMS treated devices compared to the alkyl treated

device. The carrier concentration is calculated from capacitor model after threshold correction in gate voltage. The missing data at low temperatures is because of the mobility is too low to measure or increased noise in $I-V$ curves.

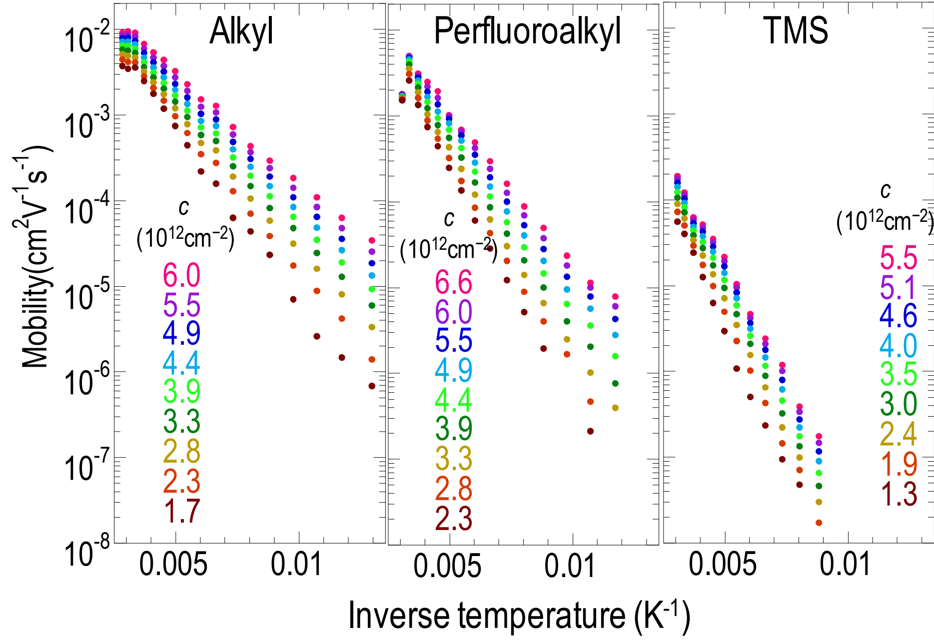

Figure 4.2 Measured $\mu(c, T)$ surfaces for rrP3HT BGBC FET devices with three different surface treatments.

The mobility was extracted in the linear regime according to:

$$\mu_{lin} = \frac{(dI_s / dV_{gs})L}{W \times V_{sd} \times C} \tag{4.1}$$

Where μ_{lin} is the linear mobility, C is the capacitance of the dielectric layer, W and L are channel width and length respectively, V_{gs} and V_{sd} are voltages on gate electrode and between source and drain electrodes, I_{sd} is the current between source and drain electrodes. During mobility extraction, one must take care of the effect of the threshold voltage V_{th} for applied gate voltage and the contact resistance if they exist. V_{th} will affect the number of free carrier density in the channel, which is an important input for the mobility fitting. The contact resistance will affect the real source-drain voltage

applied across in the channel, therefore affects the calculated mobility with Eqn. 4.1. Besides, we also need to take care of hysteresis. The detailed extraction process of $\mu_{FET}(c, T)$ is shown in Appendix B.

4.3.2 Model validation: regioregular P3HT on C_{18}-alkylsilyated SiO_2 gate dielectric

We chose FETs fabricated from regioregular poly(3-hexylthiophene) rrP3HT on the C18-alkylsilylated SiO_2 dielectric in the bottom-gate configuration as our model to test the validity of the transport mechanism. Previous near-edge fine structure spectroscopy measurements suggests that the frontier layer of P3HT on this dielectric is well-ordered with an average thiophene-ring setting angle of *ca*. 70° which indicates the formation of well-ordered lamellae at the buried interface.[9] Furthermore the current−voltage characteristics of these transistors are very well behaved. They are repeatable with no hysteresis.

In order to simulate the data, we first estimate the site density N_t in the π-packing lamella layer. By using thiophene repeat unit length a = 3.9 Å and π-π packing distance b = 3.7 Å, it is calculated that the number of thiophene unit in this layer is about 6.93 x 10^{14} cm^{-2}. So the corresponding total number of orbital N_0 in the carbon π-band is 1.3 x 10^{15} cm^{-2}. The P3HT bandwidth is estimated to be 6.7 eV by extrapolating the bandwidths of oligothiophene with different number of thiophene units to get its value at infinite oligothiophene chain length. The bandwidth of oligothiophene is calculated by using PM3 method in ChemDraw 3D software. With these two values, N_t can be calculated by the equation described earlier

Figure 4.3a shows the measured μ (c, T) surface represented by colour-coded symbols, and the fitted single-Gaussian transport DOS model represented by correspondingly colour-coded lines. Excellent agreement between simulation and experiment data over a wide temperature range (77 K to room temperature) was obtained over a factor of four range in hole density, spanning four orders of magnitude of μ. The effective N_t = 1.3 x 10^{14} cm^{-2} at 295 K, so the highest carrier density probed in the experiment c = 6.0 x 10^{12} cm^{-2} corresponds to 4% of N_t.

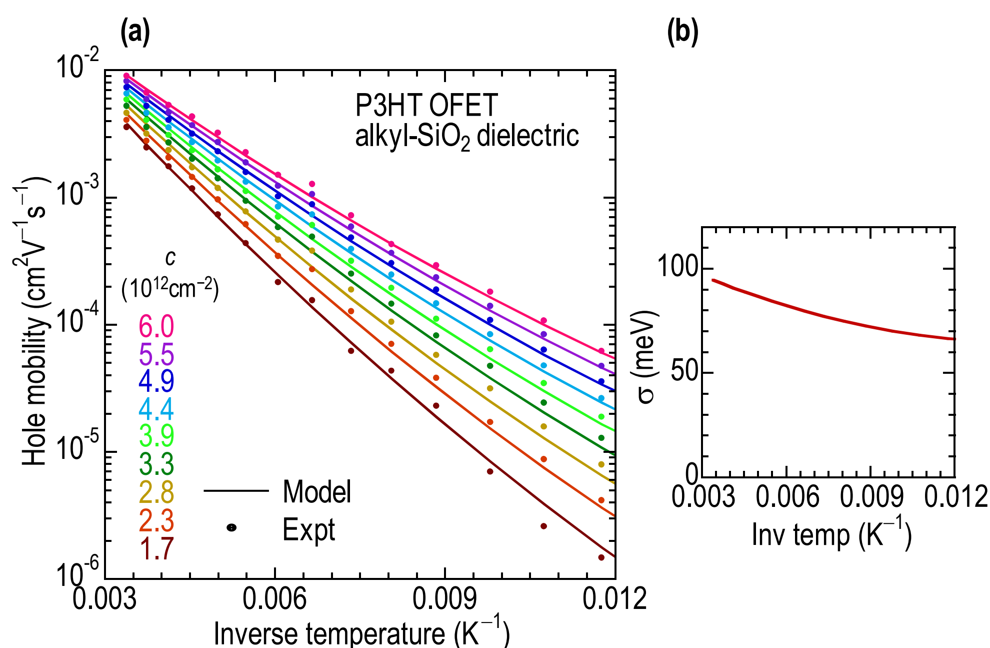

Figure 4.3 Fitting result for rrP3HT OFET with alkyl-SiO_2 dielectric. (a) Comparison of experimental and simulated $\mu(c, T)$ surfaces. (b) Transport DOS width narrowing with temperature decreasing.

The extracted <αd> parameter is 1.1, with an uncertainty of 10%. For an average interchain spacing of 3.7 Å, the interchain electronic wavefunction decay rate is 0.30 $Å^{-1}$. This is much slower than that across saturated hydrocarbon chains (0.8 – 1.0 $Å^{-1}$), similar to that across phenyleneethynylene and polyene chains (0.3 – 0.6 $Å^{-1}$), but larger than that across phenylenevinylene chains (0.06 – 0.1 $Å^{-1}$).[20-22] The value of α obtained here suggests that interchain coupling across the π stacks of rrP3HT chains

is rather more efficient than previously thought even though it is across a van der Waals gap.

The effective transport DOS width σ is 95 meV at 295 K. For comparison, population DOS width measured by the ultraviolet photoemission spectroscopy (UPS) measured at the valence band edge is 195 meV. The UPS sample was made by spin-casting a 14-nm-thick P3HT film on a Au/ Si substrate. The sample spot was translated between measurements to avoid photo- and electron-induced damage. The valence band edge was fitted to a Gaussian to extract the population DOS width. The results reveal that the transport DOS width is about half of that of the population DOS width. This is not surprising as the transport DOS width can be narrowed by correlation effects since the site-to-site energy fluctuations that the carrier senses can be smaller than the population site energy fluctuation.

In order to fit the $\mu(c, T)$ surface, the effective transport DOS width however has to decrease from 95 meV at 295 K to 65 meV at 77 K, as shown in Fig. 4.3b. This rather large effect was unexpected. To obtain independent evidence for a sizeable temperature-dependent width of the frontier edge of the DOS, we collected the UPS spectra of a rrP3HT film as a function of temperature from 295 K to 115 K. The UPS spectra of the frontier region are show in Fig. 4.4a. The valence band edge of each spectrum was fitted to a Gaussian and the effective Gaussian width plotted against inverse temperature in Fig. 4.4b. This width decreases by 18 meV from 295 K to 115 K, which is similar to the 22 meV decrease over the same temperature range deduced from transport DOS modeling. Therefore it appears firmly established that the transport DOS width can have a temperature dependence that needs to be taken into account as it is significant on the hopping energy scale.

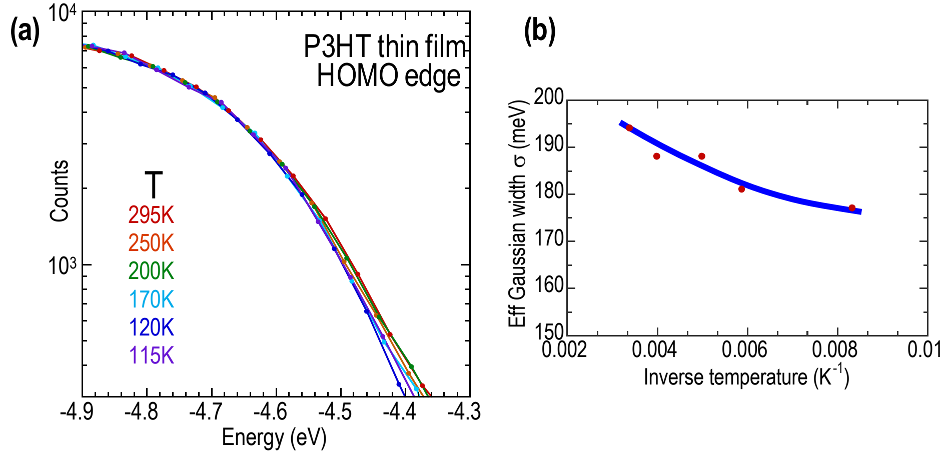

Figure 4.4 Variable temperature UPS measurement result of rrP3HT film. (a) HOMO edge narrowing with temperature decreasing. (b) HOMO edge can be fitted well with a single Gaussian function. Extracted Gaussian width (red dots) decreases with temperature, the trend is illustrated by the blue curve.

Figure 4.5 shows the transport DOS tail at 295 K and 77 K revealed by this analysis. Only the lower-energy half-Gaussian representing the relevant transport DOS edge is shown. The higher-energy half-Gaussian is irrelevant as the actual transport DOS continues to rise. The DOS is annotated with the Fermi level (E_F) and transport level (E_T) for the lowest and highest carrier densities (1.7 and 6.0 x 10^{12} cm^{-2} respectively). The E_F was computed from the Fermi-Dirac occupation of the DOS. The E_T represents the average energy level which carriers have to reach to achieve macroscopic transport.[23-26] E_T was estimated here from E_F by adding the computed apparent activation energy for transport E_A,

where $E_A = -d(ln\mu)/d(1/T)$.

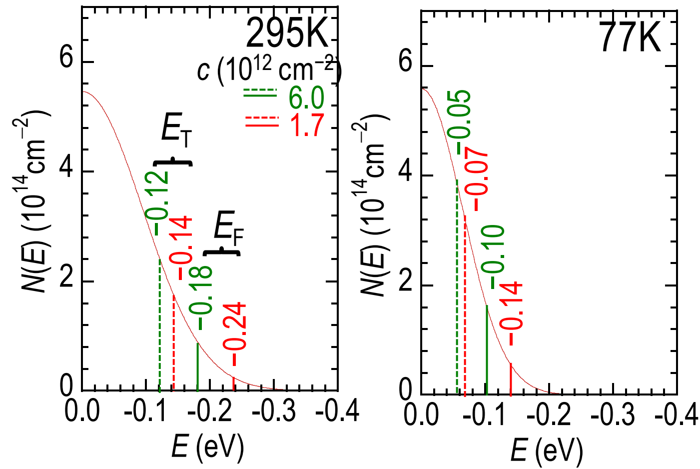

Figure 4.5 The transport DOS of rrP3HT OFET with alkyl-SiO_2 dielectric at 295 K and 77 K, together with the transport levels (E_T) and Fermi levels (E_F) for high and low carrier densities.

At 295 K, E_F occurs at −180 meV and −240 meV (below the Gaussian centre, which is 0 meV) for the highest and lowest carrier densities respectively. This shows that the carriers do occupy up quite high up in the transport DOS tail. The corresponding E_T occurs at −120 meV and −140 meV respectively. This shows that transport occurs quite high up the frontier edge of the DOS but still well within the forward half of the model Gaussian DOS. These conclusions are not qualitatively changed at 77 K. The carriers sample a significant fraction of the frontier transport DOS shape, and hence the observed transport can discriminate between different DOS shapes. The observed match between experiment and simulation suggests the hemi-Gaussian functional form for the frontier edge of the transport DOS is substantially correct. An exponential DOS form would be far less appropriate. The precise form of the DOS shape more than a few kT below E_F or above E_T is not relevant to transport. For an assumed $\nu_0 \approx 1500$ cm^{-1}, we find $\xi \approx 0.38$, which is of order unity as expected. Therefore all parameters extracted from the model are realistic and self-consistent.

To determine to what extent the assumed lattice topology influences these results, we performed another simulation assuming a square hopping lattice (with diagonal hopping elements) instead of the more realistic cross hopping lattice. The results are shown in the Appendix D. A similarly high quality-of-fit can be obtained over the entire $\mu(c, T)$ surface. The model parameters obtained at room temperature are practically identical too: $\sigma = 100$ meV, $<\alpha d> = 0.85$, $\xi = 0.36$. The locations of E_F and E_T are −190 meV and −130 meV respectively for $c = 6.0 \times 10^{12}$ cm^{-2}, practically identical to those obtained in the cross lattice model. This shows the model parameters are not overly sensitive to the assumed hopping topology, at least at room temperature, where hopping is dominated by nearest neighbor hops. Therefore the transport parameters extracted are reliable. At 77 K, a small difference emerges. The simulated σ for the square lattice model is 80 meV, which is larger than that of the cross lattice model by 15 meV. The extended hopping range that occurs at cryogenic temperatures leads the square lattice model to provide considerably more states available to the carriers than the cross lattice model. As a result, the square lattice model can tolerate a higher amount of disorder. Nevertheless the difference is still small. An important feature that is still retained is the positive temperature coefficient of σ.

Although the quality-of-fit alone is not able to discriminate between model topologies, we consider the cross lattice is the more appropriate one from electronic coupling considerations. Furthermore, the similar values in the transport parameters give us confidence in the adequacy of the variable-range hopping model and the correctness of the model parameters. Thus we conclude that the mobility characteristics over wide temperature and carrier density ranges in rrP3HT transistors with the C18-alkylsilylated SiO_2 dielectric are accurately described by variable-range hopping in a transport DOS with a forward edge that is substantially hemi-Gaussian in distribution.

The other feature that this work emphasizes again is that the μ of organic FETs has a carrier-density dependence, which we may term a dispersion phenomenon. This is a fundamental feature of the width of the transport DOS at the frontier edge. Some of this comes from disorder inherent in the packing, conformation and lattice vibrations in these van der Waals solids and is thus a fundamental feature of organic semiconductor materials. As the carrier density increases, the E_F shifts significantly up the DOS tail, as does the E_T, and meet higher DOS. Therefore μ increases with increasing carrier density. This notion has been described in the context of the relation between space-charge mobility and field-effect mobility some years ago.[27] Thus it is not appropriate to make precise comparisons of field-effect mobility values without stating the carrier density (and temperature) at which they were measured.

4.3.3 Effect of dielectric surface on the transport DOS of rrP3HT

It has been known for some time already that the apparent μ of rrP3HT in a bottom gate configuration with SiO_2 as gate dielectric is markedly influenced by the presence of any self-assembled monolayers (SAMs) which has been assembled on the SiO_2.[9,28,29] However, the physical reasons for this are much less well understood. In the following we wish to extract the transport DOS of the bottom channel of rrP3HT FETs fabricated on a perfluorodecylsilylated SiO_2 surface (i.e., perfluoroalkyl-SiO_2) and a trimethylsilylated SiO_2 surface (i.e., TMS-SiO_2) and compare these with that on a octadecylsilylated SiO_2 surface (i.e., alkyl-SiO_2) described in the previous section.

The usual way is to extract the activation energy E_A in an Arrhenius plot at a selected carrier density and temperature. This is done in Fig. 4.6, which shows that E_A at c = 6.0 x 10^{12} cm^{-2} and for 295 K < T < 100 K, increases across the series alkyl-SiO_2 (51

meV) < perfluoroalkyl-SiO_2 (69 meV) < TMS-SiO_2 (99 meV). For comparison, the E_A on an oxygen-plasma-treated SiO_2 surface (HO-SiO_2) is 46 meV, closer to that on alkyl-SiO_2. Phenomenologically, rrP3HT FETs on perfluoroalkyl-SiO_2 and on TMS-SiO_2 surfaces exhibit lower apparent field-effect mobility and larger mobility activation energies compared to those on alkyl-SiO_2 surfaces. The exact difference depends on the extent of surface treatment. Here we have used nearly exhaustive treatments as indicated by the experimentally-measured surface contact angles (advancing angles θ_a (water): HO-SiO_2,19°; perfluoro-SiO_2, 82°; TMS-SiO_2, 89°; alkyl-SiO_2, 107°. Data from G.H. Lim, ONDL). The drop in mobility is often attributed to trap formation in the channel region, but the nature of these traps and their resultant modification of the DOS have not been clarified.

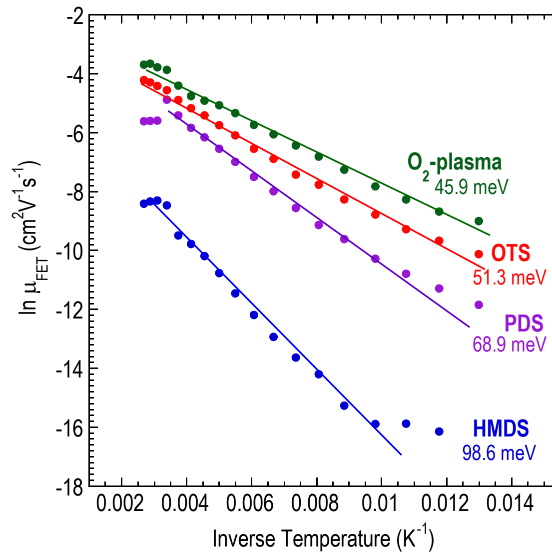

Figure 4.6 The activation energy (E_A) of mobility for rrP3HT BGBC devices with different surface treatments on SiO_2. O_2-plasma: oxygen plasma treated SiO_2 dielectric; OTS: alkyl-SiO_2 dielectric; PDS: perfluoroalkyl-SiO_2 dielectric; HMDS: TMS-SiO_2 dielectric.

To extract the DOS, we assumed the resultant DOS is a composite of the pristine DOS superposed with a downshifted DOS_{trap} which act as traps in the tail. We imagined that

the channel layer comprises a well-ordered π-stacked pristine rrP3HT frontier layer that is interrupted by regions of perturbed rrP3HT. Macroscopic field-effect transport across the channel has to occur over both the well-ordered and perturbed domains. We further assumed for simplicity that the DOS_{trap} can be modeled by a sum of Gaussians with total density N_{trap}. Self-consistency in N_t was imposed. ν_0 and $\langle\alpha d\rangle$ was assumed unchanged from those obtained for the channel with alkyl-SiO_2 dielectric surface. The DOS was iterated until excellent agreement between model and experiment $\mu(c, T)$ was obtained, as shown in Figs. 4.7a and 4.7b for the channels fabricated on perfluoroalkyl-SiO_2 and TMS-SiO_2 dielectric surfaces respectively. The key features of the progressively (i) higher apparent activation energy, (ii) stronger dispersion of transport, and (iii) lower field-effect μ in the perfluoroalkyl- and TMS-SiO_2 channels have been remarkably well reproduced. The overall transport DOS distributions extracted this way are compared in Fig. 4.8, and the ξ values are compared in Table 1. The key result is that the transport DOS for the perfluoroalkyl- and TMS-SiO_2 surfaces show an apparent increase DOS in the tail in the region where E_F and E_T reside. This tailing was modeled for the perfluoroalkyl-SiO_2 channel as an additional Gaussian component centered at −180 meV with width 57 meV and $N_{trap} =$ 6 x 10^{12} cm^{-2}; and for the TMS-SiO_2 channel as a sum of Gaussians located over −110 to −220 meV with total $N_{trap} =$ 33 x 10^{12} cm^{-2}. Therefore the results show that the degradation of the effective mobility in these channels in particular of the TMS-SiO_2 channel arises from emergence of shallow traps in the DOS that resulted in non-Gaussian tailing with enhanced intensity over the −100 to −300 meV region. The perturbed rrP3HT which gives rise to this behavior has recently been related to the population of lying down P3HT segments at the dielectric interface from charge

modulation spectroscopy and near edge X-Ray absorption fine structure measurements.[30]

In addition, the apparent ξ value for the perfluoroalkyl-SiO_2 channel decreases marginally to 0.30 while that for the TMS-SiO_2 channel severely to 0.03. This suggests that in addition to the emergence of states in the DOS tail that trap carriers, the connectivity parameter of the channel is also severely depressed over the most unfavorable dielectric surface. Therefore the carrier in the perturbed rrP3HT has to execute more difficult hops. This is not simply the result of energy of the perturbed rrP3HT relative to the rest of the well-ordered material, as this has already been accounted for in the DOS. It is attributed to a depression of the jump rate, which appears as a lowering of ξ here because $<\alpha d>$ which is dominated by transport within the well-ordered rrP3HT domain remains constant. These two features – the emergence of a DOS tail and depression of jump rate – are consistent with the rise of a perturbed rrP3HT fraction associated with a lying-down rrP3HT population at the interface.

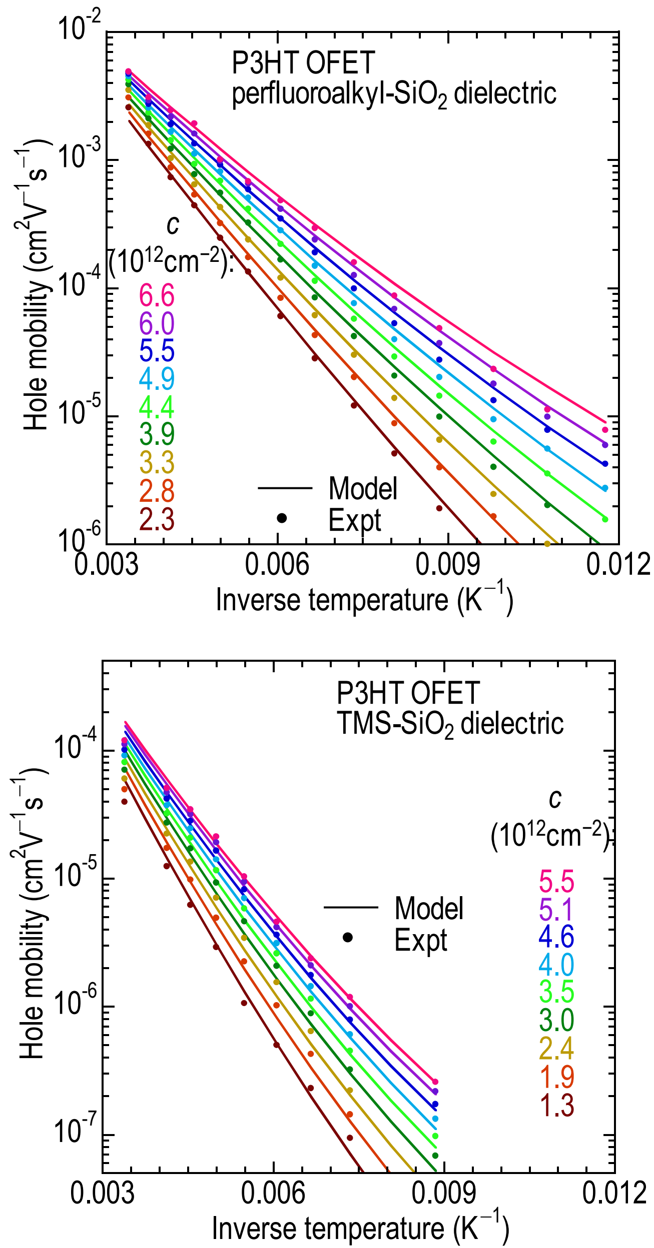

Figure 4.7 Fitting results for rrP3HT OFET devices with (a) perfluoroalkyl-SiO_2 dielectric and (b) TMS-SiO_2 dielectric.

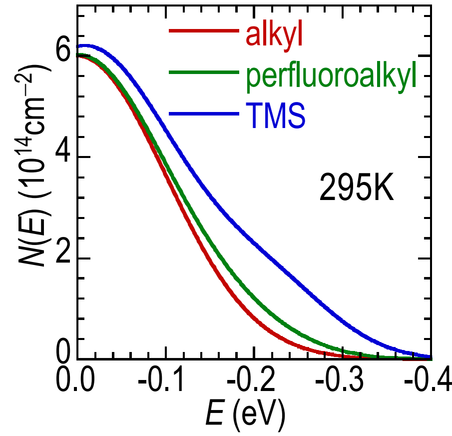

Figure 4.8 Transport DOS at 295 K for rrP3HT OFET devices with the three different surface treatments.

	ξ
alkyl-SiO_2	0.38
perfluoroalkyl-SiO_2	0.30
TMS-SiO_2	0.03

Table 4.1 Connectivity parameter ξ for rrP3HT OFET devices with the three different surface treatments.

4.4 Conclusion

We show that the model can quantitatively reproduce the entire measured $\mu(c, T)$ behavior of rrP3HT FETs with the rrP3HT layer fabricated on a model alkyl-SiO_2 dielectric surface. This surface results in a relatively well-ordered rrP3HT layer at the interface whose transport DOS turns out to be adequately modeled by a hemi-Gaussian. The width of the model Gaussian is about half of what is measured in an ultraviolet photoemission spectrum due to correlation of site energies. More

significantly a temperature dependence was found in this width in both the transport DOS and the population DOS. Other dielectric surfaces such as the perfluoroalkyl- and TMS-SiO_2 give rise to a non-Gaussian tailing of the DOS and a depression of the connectivity parameter. Both these factors together completely account for the progressive degradation of the $\mu(c, T)$ characteristics across the channels, alkyl-SiO_2 > perfluoroalkyl-SiO_2 > TMS-SiO_2, for spin-on rrP3HT transistors. The results are consistent with the generation of shallow traps from the co-existence of a population of perturbed rrP3HT chain segments in the lying-down P3HT orientation.

4.5 References

1 Yoon, M. H., Kim, C., Facchetti, A. & Marks, T. J. Gate dielectric chemical structure-organic field-effect transistor performance correlations for electron, hole, and ambipolar organic semiconductors. *J. Am. Chem. Soc.* **128**, 12851 (2006).

2 Ortiz, R. P., Facchetti, A. & Marks, T. J. High-k Organic, Inorganic, and Hybrid Dielectrics for Low-Voltage Organic Field-Effect Transistors. *Chem. Rev.* **110**, 205 (2010).

3 Veres, J., Ogier, S. D., Leeming, S. W., Cupertino, D. C. & Khaffaf, S. M. Low-k insulators as the choice of dielectrics in organic field-effect transistors. *Adv. Func. Mater.* **13**, 199 (2003).

4 Veres, J., Ogier, S., Lloyd, G. & de Leeuw, D. Gate insulators in organic field-effect transistors. *Chem. Mater.* **16**, 4543 (2004).

5 Hulea, I. N. *et al.* Tunable Frohlich polarons in organic single-crystal transistors. *Nat. Mater.* **5**, 982 (2006).

6 Richards, T., Bird, M. & Sirringhaus, H. A quantitative analytical model for static dipolar disorder broadening of the density of states at organic heterointerfaces. *J. Chem. Phys.* **128** (2008).

7 Chua, L. L., Ho, P. K. H., Sirringhaus, H. & Friend, R. H. Observation of field-effect transistor behavior at self-organized interfaces. *Adv. Mater.* **16**, 1609 (2004).

8 Chua, L. L. *et al.* General observation of n-type field-effect behaviour in organic semiconductors. *Nature* **434**, 194-199 (2005).

9 Kline, R. J., McGehee, M. D. & Toney, M. F. Highly oriented crystals at the buried interface in polythiophene thin-film transistors. *Nat. Mater.* **5**, 222 (2006).

10 Chabinyc, M. L., Toney, M. F., Kline, R. J., McCulloch, I. & Heeney, M. X-ray scattering study of thin films of poly(2,5-bis(3-alkylthiophen-2-yl)thieno 3,2-b thiophene). *J. Am. Chem. Soc.* **129**, 3226 (2007).

11 Kalb, W. L., Mathis, T., Haas, S., Stassen, A. F. & Batlogg, B. Organic small molecule field-effect transistors with Cytop™ gate dielectric: Eliminating gate bias stress effects. *Appl. Phys. Lett.* **90**, 092104 (2007).

12 Kang, I., Yun, H. J., Chung, D. S., Kwon, S. K. & Kim, Y. H. Record High Hole Mobility in Polymer Semiconductors via Side-Chain Engineering. *J. Am. Chem. Soc.* **135**, 14896 (2013).

13 Chabinyc, M. L. *et al.* Lamination method for the study of interfaces in polymeric thin film transistors. *J. Am. Chem. Soc.* **126**, 13928 (2004).

14 Kline, R. J. *et al.* Significant dependence of morphology and charge carrier mobility on substrate surface chemistry in high performance polythiophene semiconductor films. *Appl. Phys. Lett.* **90**, 062117 (2007).

15 Cheung, D. L., McMahon, D. P. & Troisi, A. A Realistic Description of the Charge Carrier Wave Function in Microcrystalline Polymer Semiconductors. *J. Am. Chem. Soc.* **131**, 11179 (2009).

16 McMahon, D. P. *et al.* Relation between Microstructure and Charge Transport in Polymers of Different Regioregularity. *J. Phys. Chem. C* **115**, 19386 (2011).

17 Chang, J. F., Sirringhaus, H., Giles, M., Heeney, M. & McCulloch, I. Relative importance of polaron activation and disorder on charge transport in high-mobility conjugated polymer field-effect transistors. *Phys. Rev. B* **76** (2007).

18 Wang, C. C. *et al.* Microstructural Origin of High Mobility in High-Performance Poly(thieno-thiophene) Thin-Film Transistors. *Adv. Mater.* **22**, 697 (2010).

19 Chen, Z. Y. *et al.* Origin of the different transport properties of electron and hole polarons in an ambipolar polyselenophene-based conjugated polymer. *Phys. Rev. B* **84**, 115211 (2011).

20 Sachs, S. B. *et al.* Rates of interfacial electron transfer through pi-conjugated spacers. *J. Am. Chem. Soc.* **119**, 10563 (1997).

21 Davis, W. B., Svec, W. A., Ratner, M. A. & Wasielewski, M. R. Molecular-wire behaviour in p-phenylenevinylene oligomers. *Nature* **396**, 60 (1998).

22 Sikes, H. D. *et al.* Rapid electron tunneling through oligophenylenevinylene bridges. *Science* **291**, 1519 (2001).

23 Bässler, H. Charge transport in disordered organic photoconductors - a monte-carlo simulation study. *Phys. Status Solidi B* **175**, 15 (1993).

24 Baranovskii, S. D., Faber, T., Hensel, F. & Thomas, P. The applicability of the transport-energy concept to various disordered materials. *J. Phys.: Condens. Matter* **9**, 2699 (1997).

25 Baranovskii, S. D., Cordes, H., Hensel, F. & Leising, G. Charge-carrier transport in disordered organic solids. *Phys. Rev. B* **62**, 7934 (2000).

26 Arkhipov, V. I., Heremans, P., Emelianova, E. V., Adriaenssens, G. J. & Bassler, H. Weak-field carrier hopping in disordered organic semiconductors: the effects of deep traps and partly filled density-of-states distribution. *J. Phys. C - Solid State Phys.* **14**, 9899 (2002).

27 Tanase, C., Meijer, E. J., Blom, P. W. M. & de Leeuw, D. M. Unification of the hole transport in polymeric field-effect transistors and light-emitting diodes. *Phys. Rev. Lett.* **91**, 216601 (2003).

28 Sirringhaus, H., Tessler, N. & Friend, R. H. Integrated optoelectronic devices based on conjugated polymers. *Science* **280**, 1741 (1998).

29 Kim, D. H. *et al.* Enhancement of field-effect mobility due to surface-mediated molecular ordering in regioregular polythiophene thin film transistors. *Adv. Func. Mater.* **15**, 77 (2005).

30 Zhuo, J. M. *et al.* Evidence for a transistion adlayer interface structure that determines the field-effect transport in semicrystalline polymer organic semiconductor films (Manuscript in preparation).

Chapter 5. Effect of molecular weight and processing in PBTTT OFETs

In this chapter, we study the effect of molecular weight and processing on charge transport in PBTTT-C14 top-gate bottom-contact OFETs. The mobility vs carrier density and temperature surfaces $\mu(c, T)$ of poly[2,5-bis(3-tetradecylthiophen-2-yl)thieno[3,2-b]thiophene] (PBTTT-C14) top-gate bottom-contact organic FETs with different molecular weights (MW) have been characterized. PBTTT-C14 films exhibit remarkable lamellar organization in which the polymer chains are π-stacked in monolayers of extended chain configurations. However the 2D spatial extent of these lamellae varies with MW. Atomic force microscopy (AFM) shows this morphology vary from long and partially fused ribbons at low MWs, through short ribbons, then to 2D terraces at high MWs, after the same annealing to the liquid crystalline (LC) phase and slow cooling. The resultant hole carrier mobility increases with number-average MW from 2,600 to 8,200 g mol^{-1} and thereafter levels off at *ca*. 0.05 cm^2 V^{-1} s^{-1}. Its temperature and carrier-density dependences also vary systematically but not monotonically with MW. Simulation of the $\mu(c, T)$ surfaces using the hopping transport model reveals for the first time that these behaviors arise from a trade-off between transport DOS tail width and microstructural connectivity, while interchain coupling is more or less constant. Both the disorder width and connectivity parameters vary strongly with MW and the associated film morphology, decreasing at first, then increasing and leveling off at high MWs. This non-monotonic behavior is the consequence of the microstructural evolution from long and partially fused ribbons, to short separated ribbons, and finally to 2D lamellae, as the MW increases. Furthermore

the significantly higher μ in high-MW PBTTT-C14 compared to rrP3HT is attributed surprisingly not to a narrower DOS tail width but to better connectivity within the 2D lamellar π-stacks. In separate experiments to decouple MW effects from morphology, we subjected the lowest-MW film to different annealing conditions below or above its LC transition followed by quench or slow cooling, then measured and simulated their $\mu(c, T)$ surfaces. The film morphologies obtained varied from fine terraces (after annealing in the para-crystalline phase) to short ribbons (after quenched cooling from its LC phase) and long partially fused ribbons (after slow cooling from LC phase). This sequence of morphology mimics that from varying MW above. The evolution of the transport DOS tail width and microstructural connectivity parameters show mimic the earlier trend. This demonstrates that the MW effects observed earlier are in large part related to the microstructural evolution. The study therefore reveals rich details in the factors influencing the macroscopic carrier mobility in organic semiconductor thin films that have not previously been accessible.

5.1 Introduction

Poly[2,5-bis(3-tetradecylthiophen-2-yl)thieno[3,2-b]thiophene] (PBTTT-C14) has been recently developed as a highly ordered material that shows a remarkable high degree of lamellar order.[1,2] Large monolayer terraces 2.2-nm thick and several hundred nanometers wide form readily in films which have been annealed to a liquid-crystal transition temperature, although it is clear now that orientation order has more or less fully developed in the spin-cast film.[3] Recently ONDL has developed PBTTT-C14 with different weight-average molecular weights (MWs) between 2,600 and 16,000 g mol^{-1} but identical chain ends. This range of polymers exhibit a rich variety of film morphologies depending on molecular weight and thus affords an excellent model system to probe molecular-weight and morphology influences on mobility through their effects on the transport DOS, interchain coupling and connectivity.

The effect of molecular weight (MW) on mobility has been of great interest since the pioneering measurements on regioregular poly(3-hexylthiophene) (rrP3HT)[4-8] and poly(9,9-di-n-octylfluorene-*alt*-bithiophene) (F8T2)[9]. Since polymer film morphology varies with MW, it is important to be able to distinguish various possibly opposing effects of morphology, disorder and interchain coupling. Previously this has not been possible. Nevertheless, the value of μ appears empirically to increase with and then saturate at high MW. For example, Chang et al.[8] reported that for rrP3HT, μ saturates at 0.1 $cm^2 V^{-1} s^{-1}$ beyond M_w of 50,000 g mol^{-1}. This appears to be related to better interchain π-stacking within the film,[10] perhaps induced by early π-stacking in solution[3] of high MW materials which have lower solubility. Since carrier mobility varies with carrier density, the comparison of carrier mobility is meaningful only when performed at constant carrier densities even if this has sometimes been neglected in the literature.

However understanding the influence of these parameters on the DOS, its interchain coupling and connectivity will provide even more fundamental insights than the empirical correlations of mobility alone.

We chose PBTTT-C14 for study because this is a high performance liquid crystalline semiconductor polymer with high hole mobility of the order of 0.1 $cm^2 V^{-1} s^{-1}$, and exhibits remarkably well-ordered lamellae from the π-stacking of extended PBTTT-C14 chains.[1,11,12] The unusual degree of lamellar order is evidenced by the appearance of large molecular terraces that are 2.2-nm tall, corresponding to the lamellar thickness, but several hundred nanometers wide[3] on the surfaces of these films when they are annealed above the liquid crystal transition temperature T_k and cooled down.[13-16] Near edge X-ray absorption fine structure spectroscopy measurements show indeed that the polymer backbones are well oriented.[17] The lamellar orientation persists from the buried interface to the top interface.[3,18] Therefore PBTTT-C14 films provide an excellent well-defined model to quantify the influences of MW and processing conditions on the transport DOS and associated characteristics.

5.2 Experiment

5.2.1 Material synthesis and thermal property

As shown in Fig. 5.1a, the material PBTTT-C14 was synthesized by Dr Jie-cong TANG (ONDL) with four molecular weights broadly following the McCulloch route[1] and were capped with phenyl group. The molecular weights were determined from ^{1}H- Nuclear magnetic resonance spectroscopy (^{1}H-NMR) method. The number-average repeat units were determined to be 2.9, 5.5, 11 and 22 for materials prepared. Therefore the

number-average molecular weights (M_n) were calculated to be 2,600; 4,300; 8,200 and 16,000 respectively. The polymers were then denoted **Pn** where **n** is the number-average repeat units in the polymer. This maximum accessible MW is smaller than that for rrP3HT because PBTTT is much less soluble in its polymerization reaction medium than rrP3HT, probably due to its lower density of side chains. The values here are the true MWs determined by ^{1}H NMR end-group analysis. These values are about half of the values obtained from gel permeation chromatography (GPC) based on polystyrene molecular weight standards.[3] Thus uncorrected GPC values, which are almost exclusively reported in the literature, overestimates the true molecular weight by a factor of 2.3 − 2.5.[19] The polydispersity index (M_w/M_n) is 1.7 for **P6−P22**, and 1.4 for **P3**.[19]

The thermal properties of the four polymers were determined by a combination of several methods including Differential scanning calorimetry (DSC), Variable temperature polarised optical microscopy (POM) and Variable temperature wide-angle X-ray scattering (WAXS).[3] As shown in Fig. 5.1b that (1) for P22, as temperature increased the polymer film changed from paracrystal into liquid crystal (LC) in nematic phase at temperature T_k and furthers changed into isotrpic phase at temperature T_i; (2) for P11−P3, there are two liquid crystal phases, the polymer films first went into layered nematic phase at temperature T_k' and then changed to nematic phase at T_k'' and finally became isotropic at T_i; (3) Both liquid crystal transition temperatures (T_k or T_k') and isotropic melting temperatures (T_i) decreased with MW.

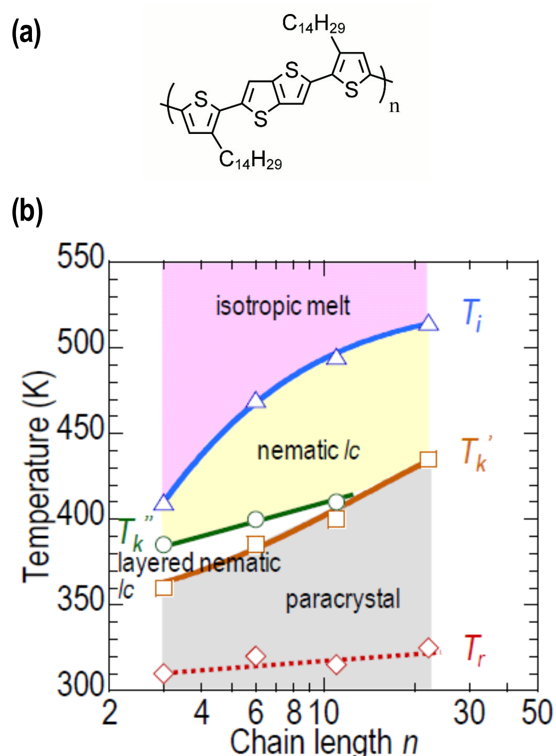

Figure 5.1 (a) Chemical structure of PBTTT-C14. (b) Phase transition temperatures for PBTTT-C14 with different molecular weights (MWs). (Data from Lihong)

Since annealing temperatures will affect the microstructure of the PBTTT films, we chose three annealing conditions for each MW: (B) annealed at nematic phase, annealing temperatures are T_k + 10K (P22) or T_k'' + 10K (P11-P3), quench cooled down; (C) annealed at nematic phase, same annealing temperatures as (B) but slow cooled down at 0.1 K/min. We will use letter A, B and C respectively to label the three annealing conditions.

5.2.2 Atomic force microscopy (AFM)

To measure the morphology of PBTTT film with various MW and annealing conditions, we prepared the Atomic force microscopy (AFM) samples by first cleaning native silicon substrates with SC-1 solution (H_2O : H_2O_2 : NH_4OH = 10 : 2 : 0.5) at about 70 ℃ for 30 min, followed by oxygen plasma cleaning for 10min. PBTTT solution (10 mg/ml

in chlorobenzene) was heated at 85 °C for 15 min and cooled down for another 15 min before it was used to spin-coat the substrates to get a 30 – 40 nm film. The solution was dropped onto the substrates with a syringe with 0.45 μm pore size PTFE filter. The spin-coated films were then heated on hotplate and cooled according to annealing conditions given above, Linkam hot stage was used for slow cooled down samples. All processing was done in N_2 filled glovebox.

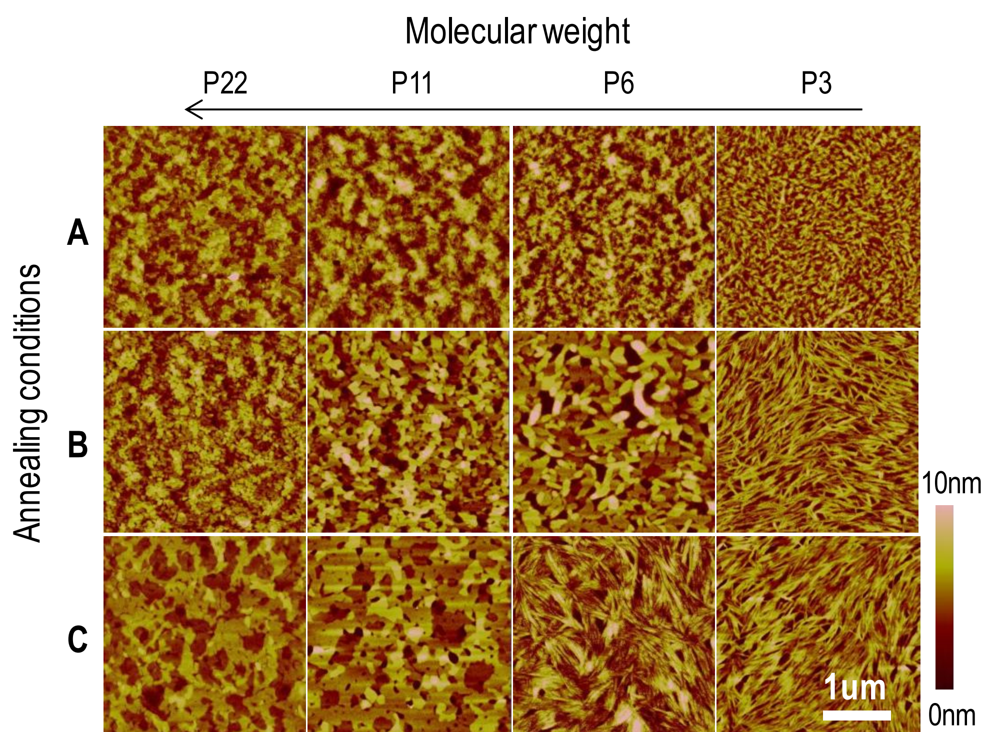

Figure 5.2 AFM pictures of different MWs PBTTT-C14 films under different annealing conditions: (**A**) Annealed at temperatures below nematic phase, annealing temperatures are T_k − 10K (P22) or T_k'' − 10K (P11–P3), quench cooled down; (**B**) Annealed at nematic phase, annealing temperatures are T_k + 10K (P22) or T_k'' + 10K (P11–P3), quench cooled down; (**C**) Annealed at nematic phase, same annealing temperatures as (B) but slow cooled down at 0.1 K/min.

The AFM pictures are shown in Fig. 5.2 for all MWs and processing conditions; all pictures are 3 x 3 μm in size and use the same 10 nm scale bar. We can see that (1) for films not heated to liquid crystal (LC) phase, they seem to be amorphous in morphology; (2) for film heated at LC phase and quench cooled down, the morphology

becomes related to MW. For P22−P6 films, they all show domain structure. As MW decreases, the domain sizes increase from tens to hundreds of nm, however the domain packing becomes loose and surface roughness seems to increase. In the P3 film, molecules form fiber-like structure and the film morphology is totally different with the others; (3) for film heated at LC phase and slow cooled down, the morphology show obvious change for P22−P6 samples. The domain sizes in P22 and P11 films increase to several hundred nm compared to quench cooled down films and the films show terrace-like morphology. Interestingly for P6 film, the morphology changes completely from domain structure in quench cooled down films to fiber-like structure, which is observed again for P3 slow cooled film. This might suggest that this structure is energy favorable for low MW PBTTT films.

5.2.3 FET measurement

Top-gate bottom-contact (TGBC) PBTTT FETs were made for all four MWs with three processing conditions, in total 12 FET devices. The device structure is shown in Fig. 5.3a and the device is fabricated as follow: First chromium-gold (thickness 7 and 40 nm) source/drain electrodes were patterned on SC-1 cleaned borosilicate glass substrates by photolithography, channel length L = 5, 10 or 20 μm, channel width W = 2 cm. After that the substrates were treated with hexamethyldisilazane (HMDS) before the PBTTT films were spin-coated on them and annealed following same procedure described in previous section. Then on top of that 200 nm Teflon AF2400 dielectric film (an amorphous copolymer of 65 mol% 4,5-difluoro-2,2-bis(trifluoromethyl)-1,3-dioxole with 35 mol% tetrafluoroethylene) was spin-coated and the devices were heated at 80-90 ºC for 10 min to remove residual solvents. At last chromium-silver (thickness 7 and

30 nm) gate electrode was evaporated on the dielectric layer to complete the FET. The spin-coating, annealing and evaporation processes were done in glove box.

The FETs were tested on probe station in glove box to check device performance first before they were transferred into Desert cryostat for variable temperature measurement. In the transfer process the devices were covered from room light but exposed to ambient atmosphere for short period (~ 10 min) which did seem to cause any performance degradation partially because of the encapsulating dielectric layer. The measurement was done in vacuum (~ 10^{-6} mbar) and dark at selected temperature points from 77 K to room temperature.

5.3 Results and discussion

The output threshold voltage V_{th} is less than 5 V for all devices for T > 150 K. We removed this from the V_{sd} to account for space-charge and contact resistance. Data from the temperature range 295 to 150 K was used for modeling. For each device, the mobility surface $\mu(c, T)$ was extracted from the linear region of the transfer curve, as a function of carrier density *c* and thermodynamic temperature T which is temperature.

The integrated π-electron density was determined to be 1.4 x 10^{15} cm^{-2} from molecular modeling (b = 3.6 Å and c = 13.3 Å, on π-stacking plane). The π-band width was assumed to be 6.7 eV, same as that of rrP3HT. A single Gaussian transport DOS of width σ was used. Then σ, $<\alpha d>$ and ξ were extracted from the iterative simulation of the experimental $\mu(c, T)$ surface, following the procedures described for rrP3HT devices. As before, a weak temperature dependence of σ was allowed, and α_w was taken to be 0.065. Excellent match between the experimental and simulated $\mu(c, T)$

surfaces were obtained in all cases. The fitting results for selected devices were shown in Table 5.1.

5.3.1 Molecular weight effect

To study molecular weight effect, we fabricated top-channel PBTTT-C14 FETs using **P3**, **P6**, **P11** and **P22**. The channel dielectric is a perfluorinated polymer AF2400® from Dupont. The organic semiconductor films were all annealed to the LC phase and cooled down slowly to room temperature at 0.1 K min^{-1}. Figure 5.3b shows the experimental and simulated $\mu(c, T)$ surfaces for these four MWs. The symbols are the experimental results, and the lines are the simulations. The measured temperature range is 150 − 295 K, and carrier-density range is 0.5 − 2.6 x 10^{12} cm^{-2}. Excellent match of the two surfaces was obtained. The hole mobility of the films generally decreases with decreasing MW below **P11**. This trend is qualitatively similar to that reported earlier for P3HT[8] and F8T2[9], but the increase in mobility from **P22** to **P3** is only about half a decade, which is smaller than in the other polymers. Detailed measurements here show in addition the temperature and carrier-density dependences of mobility also exhibit a systematic variation with MW. This does not appear to have been noted previously. The temperature dependence tends to become weaker at the lower MWs but the carrier-density dependence becomes stronger.

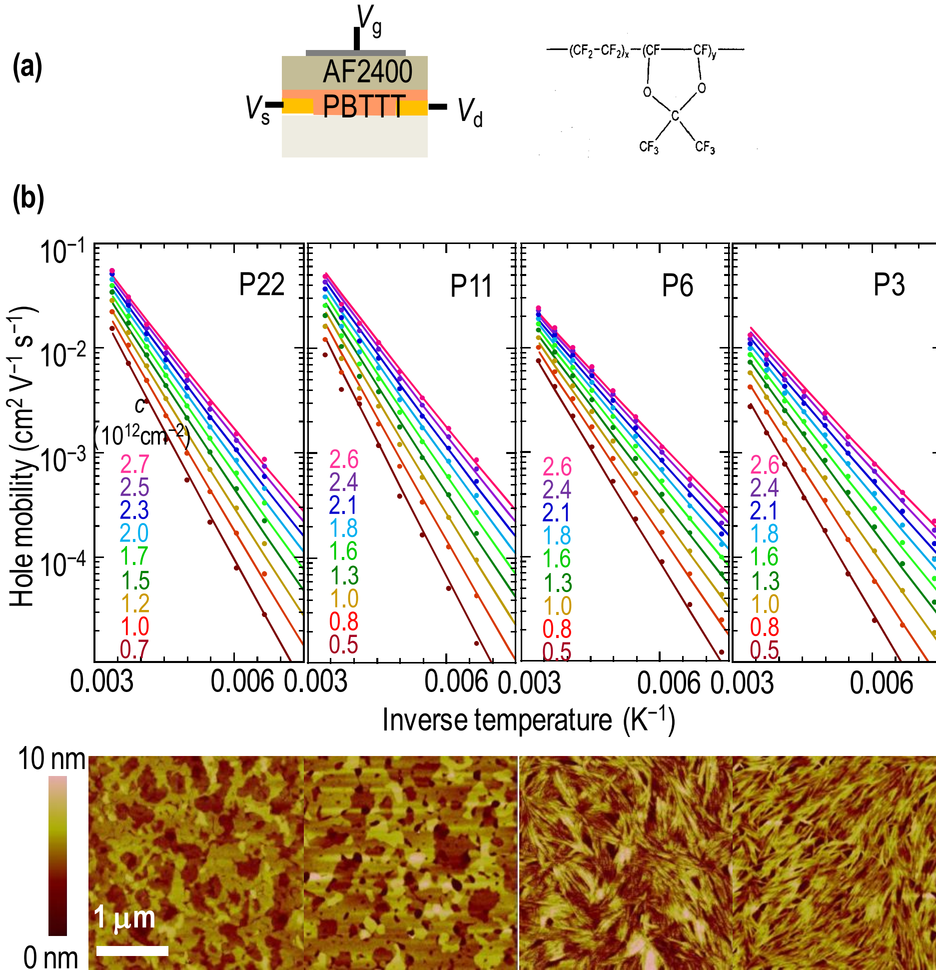

Figure 5.3 (a) Structure of the top-gate bottom-contact (TGBC) FET on the left, chemical structure of AF2400 on the right. (b) Fitting results for PBTTT-C14 TGBC FET devices with different MWs and processed with annealing condition C.

The evaluated transport DOS is shown in Fig. 5.4, together with their E_T and E_F energy levels at 295 K. The E_F lies just below -2σ while E_T lies just below -1σ for all these devices under typical operating conditions. This is far from the center of the semi-Gaussian transport DOS model, which again justifies the use of this form to describe the frontier edge of the transport DOS. The linear hole mobility at 2.6 x 10^{12} cm^{-2} and 295 K, together with the transport parameters $<\alpha d>$, ξ and σ are plotted in Fig. 5.5. The hole mobility increases from *ca.* 0.01 cm^2 V^{-1} s^{-1} to near 0.1 cm^2 V^{-1} s^{-1} as M_n increases from 2,000 to 10,000 g mol^{-1}, and levels off thereafter, qualitatively similar to the other materials systems.[8]

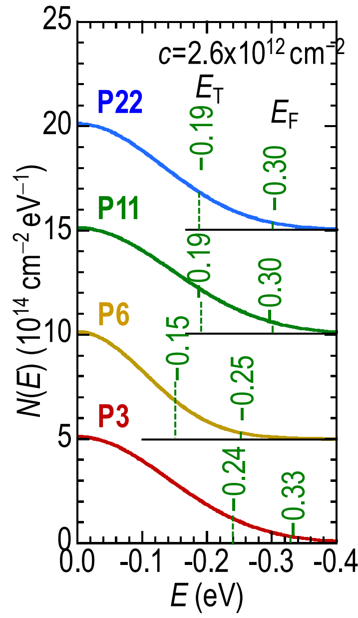

Figure 5.4 Extracted transport DOS at 295 K for PBTTT-C14 TGBC FET devices with different MWs and processed with annealing condition C.

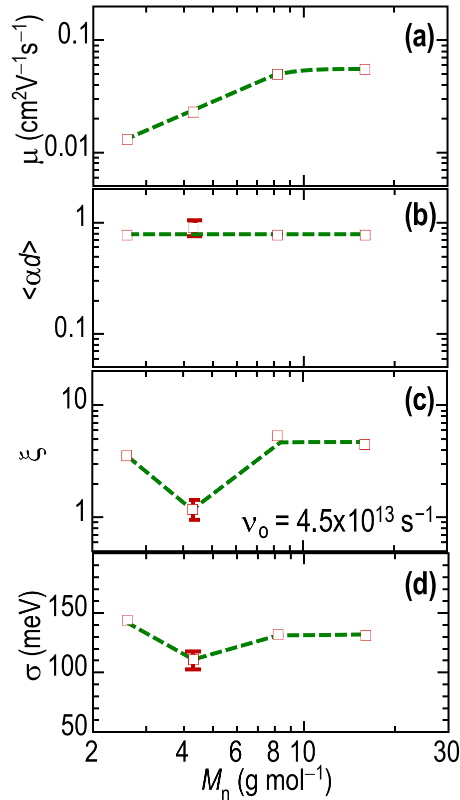

Figure 5.5 Fitting parameters for PBTTT-C14 TGBC FET devices with different MWs and processed with annealing condition C. (a) Mobility of the four devices under room temperature at highest carrier density. (b)-(d) Coupling parameter, connectivity

parameter and DOS width at 295 K respectively. Error in the fitting parameters indicated in the plot for P6 device.

Detailed analysis of the transport parameters however reveals the apparently simple temperature dependence behavior of mobility is an accidental outcome of the opposite influences of different factors. The <αd> parameter is nearly constant, between 0.8 and 0.9 for all molecular weights. These parameters quantifies interchain coupling, which should be constant for a given polymorph of interchain packing. The <αd> parameter in PBTTT-C14 is smaller than in rrP3HT (*ca*. 1.1). Thus the interchain coupling in PBTTT-C14 is better than that in rrP3HT. Part of this is attributed to a shorter π stacking distance in PBTTT-C14 (3.6 Å) than in rrP3HT (3.7 Å).[20]

The apparent width of the frontier edge of the transport DOS however shows a significant non-monotonic dependence on molecular weight. The σ parameter decreases from 120 meV for **P22** and **P11** to 100 meV for **P6** but increases again to 120 meV for **P3**. The X-ray diffraction (01) Bragg reflection of these samples occurs at 3.64 ± 0.01 Å, independent of MW, but the corresponding Scherrer width increases from 13−14 nm in **P22−P11** to 17−18 nm in **P6−P3**.[19] The lowest molecular-weight sample **P3** only shows a marginal improvement in structure coherence and bulk crystallinity over the **P6** or the others. Although the existence of long-range order may not be directly relevant to transport,[10] the initial narrowing of σ with decreasing chain length and then broadening at the shortest chain length, suggests energetic disorder which does limit transport broadly tracks the long-range π-stacking order. The surprising increase in energetic disorder in the transport DOS tail of **P3** is attributed to disproportionately stronger influence of polydispersity on low-molecular-weight samples due to proximity to chain ends. This is reflected in the limited crystallinity and structure coherence observed in the **P3** material.

Although the field-effect channel of **P6** exhibits the lowest energetic disorder, its mobility is not the highest, because it exhibits a low ξ of *ca*. 1 compared to 4−5 in **P11−P22**. AFM images of the film morphology suggests a strongly fibrillar film organization, in which the polymer chains are π-stacked in the extended-chain conformation into highly anisotropic whiskers. The typical length of a whisker is one to several hundred nanometers long, and tens of nanometer wide. For comparison, the average extended chain is only 7.5 nm. Hence more than one chain is required to span the whisker width. Although neighbouring whiskers are oriented in the same direction, the overall orientation distribution is random. There also appears to be gaps between adjacent whiskers and whisker bundles at least at the top surface visualized by AFM. The low ξ parameter obtained suggests that this fibrillar film retains poor connectivity at the buried interface. Charge carriers need to hop across the domain boundaries, which greatly hampers the overall charge transport mobility. This connectivity appears to partly recover in the **P3** film. AFM images of the film morphology indicate also a fribillar morphology, but the fibres are much longer (micrometers), curves in different directions and show an incipient broadening towards 2D islands. The improvement in ξ appears to be related to the emergence of this more favorable microstructure. In contrast **P11** and **P22** films give the usual terraced monolayer morphology with large terrace widths of several hundred nanometers in AFM. Since the terrace width is much larger than the extended chain lengths (15 and 30 nm for **P11** and **P22** respectively), each monolayer lamella must comprise numerous sub-domains of 2D π-stacked PBTTT-C14 chains.

Finally the tail width of the transport DOS in PBTTT-C14 here is larger compared to that in rrP3HT channels formed over octadecylsilyl-SiO_2 dielectric surfaces where $\sigma \approx$ 100 meV, despite the facile appearance of lamellar order in the former. However the ξ

parameter is also considerably larger by slightly more that one order of magnitude. Hence the improvement in field-effect carrier mobility in PBTTT-C14 over rrP3HT channels is not due to lower energetic disorder, but better interchain coupling and microstructure connectivity within the channel arising from the more extended 2D π-stacks. The characteristic signatures that led to these conclusions - changes in temperature and carrier-density dependences of mobility and its absolute - are directly observable in the data without before modeling.

5.3.2 Processing effect

The question now is whether the same technique can be applied to extract the signatures of film processing on transport DOS and other parameters. PBTTT-C14 affords a good model system for study because of strong morphological dependence on processing because of the intervention of the liquid-crystalline transition. To decouple morphology effects from MW, we studied the effects of different annealing conditions on **P3** and **P22**: (**A**) anneal to just below the liquid-crystalline transition temperature, i.e. $T_k' - 10$ K, then quenched; (**B**) anneal to just above the nematic liquid-crystalline temperature, i.e., $T_k'' + 10$ K, then quenched; or (**C**) as in (**B**) but slow cool at 0.1 K min^{-1}. For **P22**, these three conditions make very little difference to μ. The $\mu(c, T)$ surfaces of the FETs subjected to conditions **B** and **C** are identical, although AFM images show that the domain size of the monolayer terraces increase after slow cool down. Thus the macroscopic domain sizes imaged by AFM may not be directly relevant to the transport DOS and microstructure which determine carrier mobility.

A significant processing dependence of mobility was found for **P3** devices. The apparent μ at room temperature drops from 0.04 after **3A** to 0.01 after **3B**, and partially recover to 0.013 cm^2 V^{-1} s^{-1} after **3C**. The $\mu(c, T)$ surface was therefore investigated further by simulation, as shown in Fig. 5.6. Again excellent fits were obtained. The transport DOS together with E_F and E_F at 295 K are shown in Fig. 5.7a. The room temperature μ at 2.6 x 10^{12} cm^{-2}, <αd>, ξ, and room temperature σ values for different heat-treatment conditions are shown in Fig. 5.7b. The results reveal that the dominant factors that determine the mobility trend here are again ξ and σ acting in opposition.

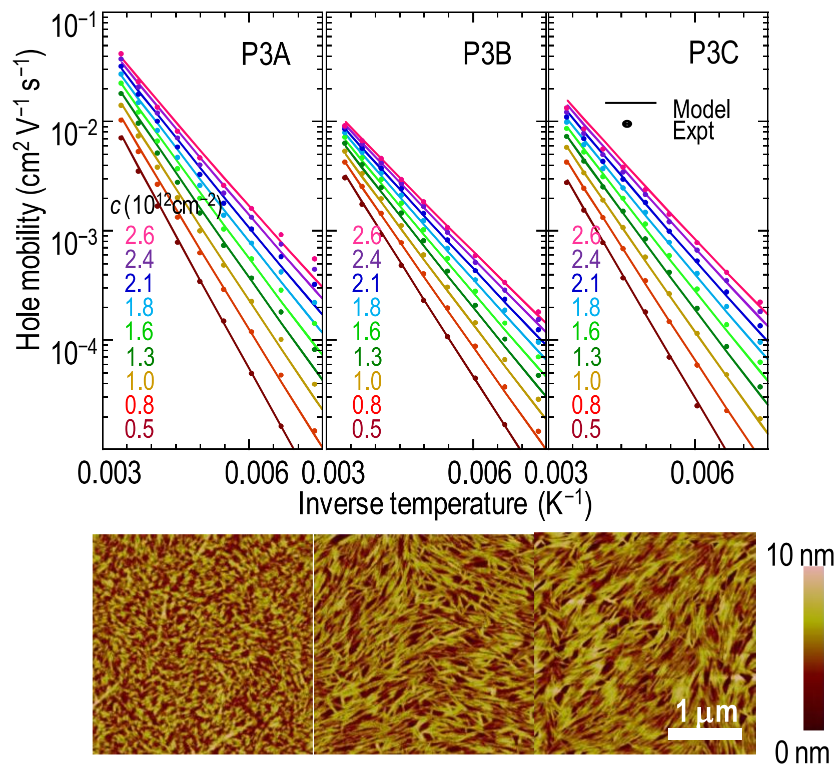

Figure 5.6 Fitting results for PBTTT-C14 TGBC FET devices with lowest MW (P3) and processed with different annealing conditions.

The transport DOS tail width decreases from 140 meV in film **3A** to 110 meV after quench-cool from the liquid-crystalline state in film **3B**. This is consistent with the AFM images which suggest the film morphology becomes better ordered. This factor alone

should promote mobility as both E_T and E_F occur higher up in the DOS. However ξ decreases by one order of magnitude from 5.5 to 0.6. As a consequence mobility is depressed at room temperature, even though its temperature and carrier-density dependences improve. After slow cool from the liquid-crystalline state in film **3C**, ξ improves but σ also broadens. As a result the room-temperature mobility improves marginally, but low-temperature mobility remains more or less unchanged. The **3B** $\rightarrow$ **3C** changes are strongly reminiscent of those of **P6** $\rightarrow$ **P3**. In fact the AFM images for **3B** $\rightarrow$ **3C** show a similar transformation of surface morphology from short whiskers that appear separated on the film plane to longer whiskers which show incipient fusing to give 2D monolayer islands. Therefore this appears to correspond to a microstructural transformation that leads to improved connectivity across the channel.

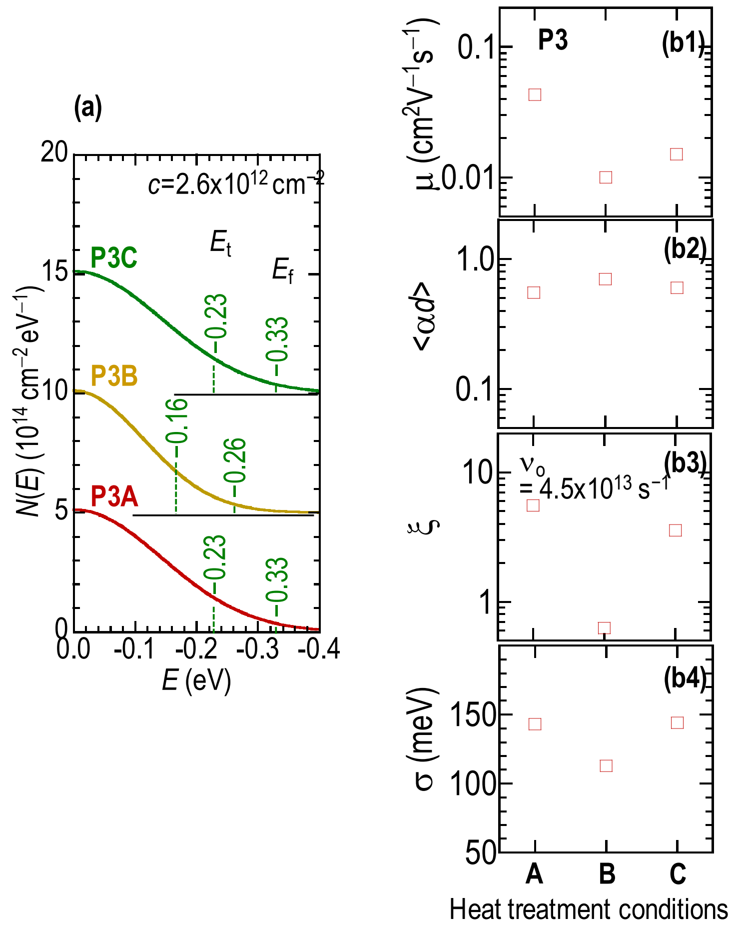

Figure 5.7 Fitting parameters for PBTTT-C14 TGBC FET devices with lowest MW (P3) and processed with different annealing conditions. (a) Transport DOS at 295 K. (b1) Mobility of the three devices under room temperature at the highest carrier density. (b2)-(b4) Coupling parameter, connectivity parameter and DOS width at 295 K respectively.

	Mn ($10^3 gmol^{-1}$)	μ ($cm^2 V^{-1} s^{-1}$)	$\langle \alpha d \rangle$	ξ	σ(meV) 295K
P22	22	0.055	0.8	4.4	131
P11	8.2	0.050	0.8	5.3	132
P6	4.3	0.023	0.9	1.6	104
P3A		0.043	0.7	5.6	111
P3B	2.6	0.010	0.9	0.6	113
P3C		0.013	0.8	3.6	144

Table 5.1 Summary of molecular weights, mobility at 295 K and fitting parameters for the PBTTT-C14 TGBC FET devices.

5.4 Conclusion

We use the numerical model to study the MW and processing condition effect on charge transport in PBTTT TGBC FET devices. The fitting results for different MW devices suggest the higher mobility in high MW devices is due to better coupling in high MW films which comes from the improved connection between ordered domains by long polymer chains acting as fast charge transporting link. Study for processing effect shows that the performance of high MW devices is insensitive to annealing conditions while low MW devices are greatly affected since the microstructure of low MW films are sensitive to those conditions. Similarly the connection between ordered

domains by polymer chain is proved to be important for the charge transport process and to achieve high FET mobility.

5.5 References

1 McCulloch, I. *et al.* Liquid-crystalline semiconducting polymers with high charge-carrier mobility. *Nat. Mater.* **5**, 328 (2006).

2 McCulloch, I. *et al.* Semiconducting thienothiophene copolymers: Design, synthesis, morphology, and performance in thin-film organic transistors. *Adv. Mater.* **21**, 1091 (2009).

3 Zhao, L. H. *et al.* Role of borderline solvents to Induce pronounced extended-chain lamellar order in pi-stackable polymers. *Macromol.* **44**, 9692 (2011).

4 Kline, R. J., McGehee, M. D., Kadnikova, E. N., Liu, J. S. & Frechet, J. M. J. Controlling th field-effect mobility of regioregular polythiophene by changing the molecular weight. *Adv. Mater.* **15**, 1519 (2003).

5 Kline, R. J. *et al.* Dependence of regioregular poly(3-hexylthiophene) film morphology and field-effect mobility on molecular weight. *Macromol.* **38**, 3312 (2005).

6 Zen, A. *et al.* Effect of molecular weight and annealing of poly (3-hexylthiophene)s on the performance of organic field-effect transistors. *Adv. Funct. Mater.* **14**, 757 (2004).

7 Zen, A. *et al.* Effect of molecular weight on the structure and crystallinity of poly(3-hexylthiophene). *Macromol.* **39**, 2162 (2006).

8 Chang, J. F. *et al.* Molecular-weight dependence of interchain polaron delocalization and exciton bandwidth in high-mobility conjugated polymers. *Phys. Rev. B* **74**, 115318 (2006).

9 Donley, C. L. *et al.* Effects of packing structure on the optoelectronic and charge transport properties in poly(9,9-di-n-octylfluorene-alt-benzothiadiazole). *J. Am. Chem. Soc.* **127**, 12890 (2005).

10 Noriega, R. *et al.* A general relationship between disorder, aggregation and charge transport in conjugated polymers. *Nat. Mater.* **12**, 1037 (2013).

11 Wang, S. *et al.* Solvent effects and multiple aggregate states in high-mobility organic field-effect transistors based on poly(bithiophene-alt-thienothiophene). *Appl. Phys. Lett.* **93**, 162103 (2008).

12 Zhao, N. *et al.* Polaron localization at interfaces in high-mobility microcrystalline conjugated polymers. *Adv. Mater.* **21**, 3759 (2009).

13 Chabinyc, M. L., Toney, M. F., Kline, R. J., McCulloch, I. & Heeney, M. X-ray scattering study of thin films of poly(2,5-bis(3-alkylthiophen-2-yl)thieno 3,2-b thiophene). *J. Am. Chem. Soc.* **129**, 3226 (2007).

14 Kline, R. J. *et al.* Significant dependence of morphology and charge carrier mobility on substrate surface chemistry in high performance polythiophene semiconductor films. *Appl. Phys. Lett.* **90**, 062117 (2007).

15 Northrup, J. E. Atomic and electronic structure of polymer organic semiconductors: P3HT, PQT, and PBTTT. *Phys. Rev. B* **76**, 245202 (2007).

16 Brocorens, P. *et al.* Solid-State Supramolecular Organization of Polythiophene Chains Containing Thienothiophene Units. *Adv. Mater.* **21**, 1193 (2009).

17 DeLongchamp, D. M. *et al.* High carrier mobility polythiophene thin films: Structure determination by experiment and theory. *Adv. Mater.* **19**, 833 (2007).

18 Kline, R. J., McGehee, M. D. & Toney, M. F. Highly oriented crystals at the buried interface in polythiophene thin-film transistors. *Nat. Mater.* **5**, 222 (2006).

19 Zhao, L. H., Png, R. Q., Zhuo, J. M., Ho, P. K. H. & Chua, L. L. Manuscript in preparation.

20 Zhuo, J. M. *et al.* Direct Spectroscopic Evidence for a Photodoping Mechanism in Polythiophene and Poly(bithiophene-alt-thienothiophene) Organic Semiconductor Thin Films Involving Oxygen and Sorbed Moisture. *Adv. Mater.* **21**, 4747 (2009).

Chapter 6. Charge transport in high electron mobility P(NDI2OD-T2) FETs

In this chapter, we study the charge transport in a high electron mobility donor-acceptor polymer P(NDI2OD-T2) with top-gate bottom-contact FET devices, which show mobility ~0.1 $cm^2 V^{-1} s^{-1}$ at room temperature. The extracted $\mu(c, T)$ surface show much narrower mobility spread with charge carrier density, along with similar activation energy to that of rrP3HT and PBTTT. The narrow spread was attributed to a narrow transport DOS of P(NDI2OD-T2), the width of which is less than half of that in rrP3HT and PBTTT also has much weaker temperature dependence. This narrow transport DOS width is the primary reason for the high electron mobility in P(NDI2OD-T2) despite its slightly worse interchain coupling and intermediate connectivity compared to rrP3HT and PBTTT. The study shows that narrow transport DOS, good interchain coupling and good connectivity between aggregates are key factors in charge transport process to achieve high FET mobility.

6.1 Introduction

Very recently some classes of donor-acceptor polymers were reported to have unexpected high mobility for hole or electron transport with the highest hole and electron mobility reported to be around 12 and 6 $cm^2 V^{-1} s^{-1}$ respectively for unaligned films,[1,2] which is well above the benchmark value (1 $cm^2 V^{-1} s^{-1}$) of amorphous silicon and mobility around or larger than 1 $cm^2 V^{-1} s^{-1}$ is widely reported in literature,[3-5] bringing semiconducting polymer one more step closer towards real, wide-range application in markets. Together with the high mobility, in some cases the kind of material can also show balanced ambipolar charge transport behavior,[6-8] which is useful for application in complementary circuits.

The donor-acceptor polymer chain consists of alternating donor (electron donating) unit and acceptor (electron withdrawing) unit.[9] The reason for the high mobility in donor-acceptor polymers is still unknown and under intensive study. Up to now as reviewed by Sirringhaus[10], the microstructure of the donor-acceptor polymers seems to have following features: 1) very small backbone distortion from the coplanar conformation;[5,11] 2) Between polymer chains, there exists predominantly donor-donor/acceptor-acceptor packing;[4,12] 3) high degree of in-plain alignment of the polymer chain;[4,13,14] 4) high mobility obtained for both plane-on and edge-on orientations of the polymer chain; [8,13,15,16] 5) side-chain choice is important.[1,12,17] The broad correlation between the microstructure and charge transport is reported by Noriega et al.,[18] however there is still no report to study the charge transport behavior quantitatively through $\mu(c, T)$ data modeling to show insight into the factors that contribute into the high charge transport mobility from theoretical point of view. In this chapter we used a recently reported high mobility *n*-type donor-acceptor material to

characterize its transport DOS and other transport parameters, and to see whether from them we could get useful information to explain its superior performance and provide guidelines for further material development.

6.2 Experiment

The material poly{[N,N9-bis(2-octyldodecyl)-naphthalene-1,4,5,8-bis(dicarboximide)-2,6-diyl]-alt-5,59-(2,29-bithiophene)} (P(NDI2OD-T2))[19] or known by its commercial name ActivInk N2200 was purchased from Polyera company, and used without further purification. Its molecular structure is shown in Fig. 6.1a.

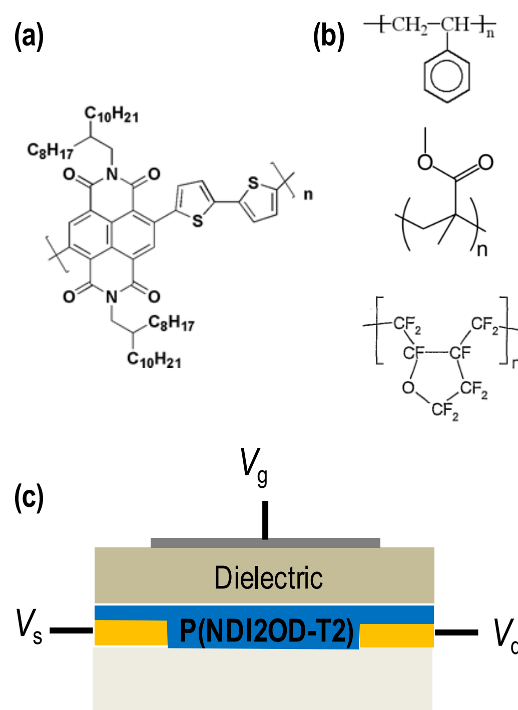

Figure 6.1 (a) Chemical structure of P(NDI2OD-T2). b) Structure of dielectric polymers. From top to bottom: PS, PMMA, CYTOP. c) BGTC FET device structure

Top-gate-bottom-contact (TGBC) P(NDI2OD-T2) FETs were made with three different dielectrics[20] as shown in Fig. 6.1b, i.e. Polystyrene (PS, MW = 2M), CYTOP

fluoropolymer, Poly(methyl methacrylate) (PMMA, MW = 35K), The device structure is shown in Fig. 6.1c and the devices were fabricated as follow: First chromium-gold (thickness 7 and 30 nm) source/drain electrodes were patterned on SC-1 cleaned borosilicate glass substrates by reverse photolithography, channel length L = 200 μm, channel width W = 3.15 cm. The substrates were then thoroughly cleaned with oxygen plasma (30 min, 300 W) followed with solvent wash (Acetone, IPA) and another 30 min oxygen plasma treatment. The P(NDI2OD-T2) polymer was dissolved in anhydrous Dichlorobenzene to make 9 mg/ml solution, which was spin-coated at 3000 rpm to get 30 nm film. The film was annealed at 110 °C for 10 min to remove residual solvents. Then the dielectric films were spin-coated on top from individual dielectric solutions (PS/PMMA in *n*-butyl acetate, CYTOP diluted in its own solvent) and then annealed at 110 °C for 10 min to remove residual solvents. The dielectric film thickness was 340, 400, 260 nm for PS, PMMA, CYTOP respectively. At last chromium-silver (thickness 7 and 30 nm) gate electrode was evaporated on the dielectric layer to complete the FET. The spin-coating, annealing and evaporation processes were done in glove box.

The FETs were tested on probe station in glove box to check device performance first before they were transferred into Desert cryostat for variable temperature measurement. In the transfer process the devices were covered from room light but exposed to ambient atmosphere for short period (~ 10 min) which did seem to cause any performance degradation partially because of the encapsulating dielectric layer. The measurement was done in vacuum (~ 10^{-6} mbar) and dark at selected temperature points from 77 K to room temperature.

6.3 Results and discussion

The FET data is extracted according to procedure described in Appendix B. The contact resistance is negligible but the threshold V_{th} for gate is shown to be quite large. After analyzing transfer curves at all temperatures, the V_{th} value for CYTOP and PS device is taken as 12 V and 14 V respectively. For the PMMA device, the V_{th} value keeps increasing when temperature goes down, so we do not use its data for further model fitting as there might be other unknown factors causing this problem and comprise the fitting result. Data between 295 K to 113 K was used for modeling for CYTOP and PS device.

The integrated π-electron density was determined to be 2.04 x 10^{15} cm^{-2} from molecular modeling (b = 3.65 Å and c = 14.3 Å,[21] π-stacks tilted 35° form substrate normal[22]). The π-band width was assumed to be 4.8 eV according to quantum calculation in section 6.3.1. A single Gaussian transport DOS of width σ was used. Then σ, $<\alpha d>$ and ξ were extracted from the iterative simulation of the experimental $\mu(c, T)$ surface, following the procedures described for rrP3HT devices. As before, a weak temperature dependence of σ was allowed, and αd_w was taken to be 0.065.

6.3.1 π-band calculation

For P(NDI2OD-T2) the charge carriers are electrons, which transport at energy levels in the unoccupied π^*-band that are near LUMO (lowest unoccupied molecular orbital). The width of this π^*-band is needed to calculate the π^*-orbital density for further fitting. With our quantum calculation software we can only calculate the π^*-band for the monomer of P(NDI2OD-T2), i.e. Single thiophene − naphthalene-bis(dicarboximide)

−thiophene (T-NDI-T) unit, the width of which is about 4.8 eV. However, for the π-band we are able to calculate until 3 monomers as shown in Fig. 6.2a. The π-band structure is similar to that of oligothiophenes with relatively high edges and flat over central region. The π-band width increases from 7.8 eV to 8.4 eV when the monomer number increases to 2, and does not further increases. This feature of the donor-acceptor polymer is clearly different from that of the thiophene polymers.

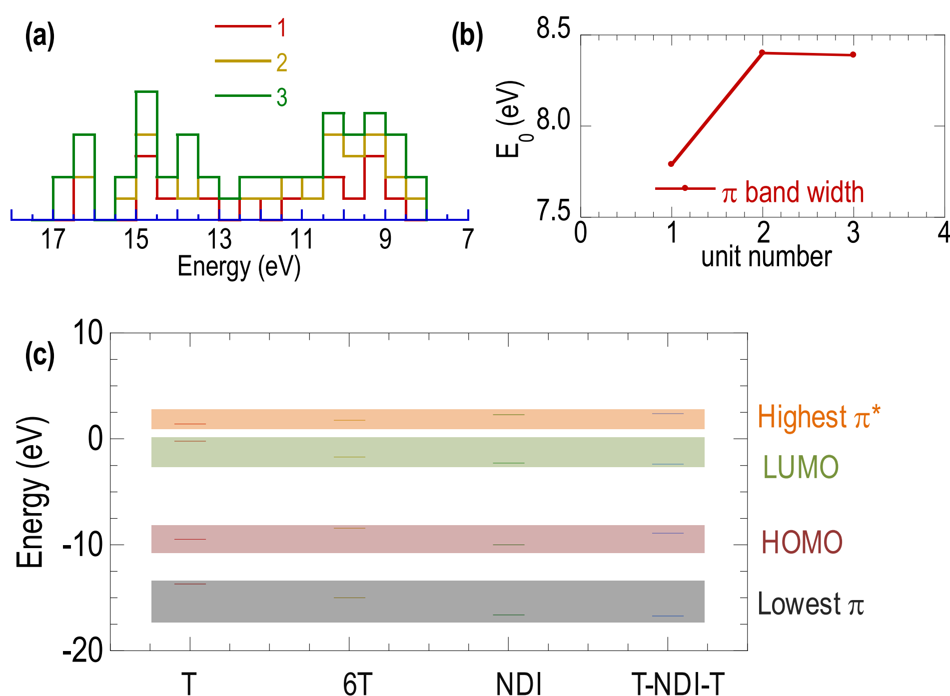

Figure 6.2 (a) π band structure of $(T\text{-}NDI\text{-}T)_x$ unit, x = 1, 2, 3. (b) π band width for x = 1 − 3. (c) Energy levels of four molecular orbital for four molecular structures, from left to right: thiophone (T), 6-thiophene (6T), NDI, T-NDI-T. From top to bottom: highest π^* orbital, LUMO, HOMO, lowest π orbital.

From more detailed analysis, we could get to the conclusion that the π^* band width of P(NDI2OD-T2) is expected to remain the same when the monomer number is larger than 1. When thiophene and NDI unit connects to form P(NDI2OD-T2) monomer unit, their molecular orbital hybrids to form new molecular orbital and as a result the new energy levels can be viewed as a combination of the two sets of energy levels. Thus as

shown in Fig. 6.2c, the π band width of T-NDI-T unit is roughly determined by the energy level of lowest occupied π orbital of NDI and HOMO of thiophene. Similarly, the $\pi*$ band width of T-NDI-T unit would be solely determined by the highest unoccupied $\pi*$ orbital and LUMO of NDI unit. The HOMO level of oligothiophenes increases as the monomer number increases, causing HOMO level of $(\text{T-NDI-T})_x$ (x monomers) to increases and π band width broaden although the effect quickly disappears for x > 2. In contrast, the $\pi*$ band of oligothiophenes broadens as well with increasing monomer number, but its $\pi*$ band range never exceeds that of the NDI unit. It indicates the $\pi*$ band width is constant for P(NDI2OD-T2), so we just use $\pi*$ band width of T-NDI-T unit for further calculation.

6.3.2 Transport DOS in donor-acceptor polymer

Figure 6.3a shows the experimental and simulated $\mu(c, T)$ surfaces for CYTOP-gated device. The symbols are the experimental results, and the lines are the simulations. The measured temperature range is 113 − 295 K, and carrier-density range is 0.2 − 1.9 x 10^{12} cm^{-2}. Excellent match of the two surfaces was obtained. The electron mobility is at the level of 0.1 cm^2 V^{-1} s^{-1}, which is similar to literature reported value[19]. One interesting feature of this $\mu(c, T)$ surface is that the mobility spread is very small when the charge carrier concentration changes over one order of magnitude at all temperatures, compared to that of rrP3HT and PBTTT. However, the activation energy appears to be similar between these materials.

This narrow spread in mobility leads naturally to small DOS width within this model. The fitted DOS width changes from 45 meV at 295 K to 40 meV at 113 K as shown in

Fig. 6.3b, which is only half of that of rrP3HT and less than half of that of PBTTT at room temperature. Furthermore, the change in DOS width with temperature is much smaller than rrP3HT and PBTTT. This narrow DOS width is likely to be an intrinsic feature of donor-acceptor polymer, as shown in previous section that the π and $\pi*$ band widths stop increasing at very small number of monomers i.e. short length range. As a result, the spread of HOMO/LUMO levels i.e. transport DOS tends to be narrow despite polymer chain twist/bending and change in polymer chain environment at different packing structures. Figure 6.3c and d show the transport DOS tail at 295 K and 113 K respectively together with the E_T and E_F energy levels for the highest carrier concentration c = 1.9 x 10^{12} cm^{-2}. The E_T lies near -1σ at low T or even lower at high T, again showing it is reasonable to use single Gaussian function to describe the frontier edge of the transport DOS.

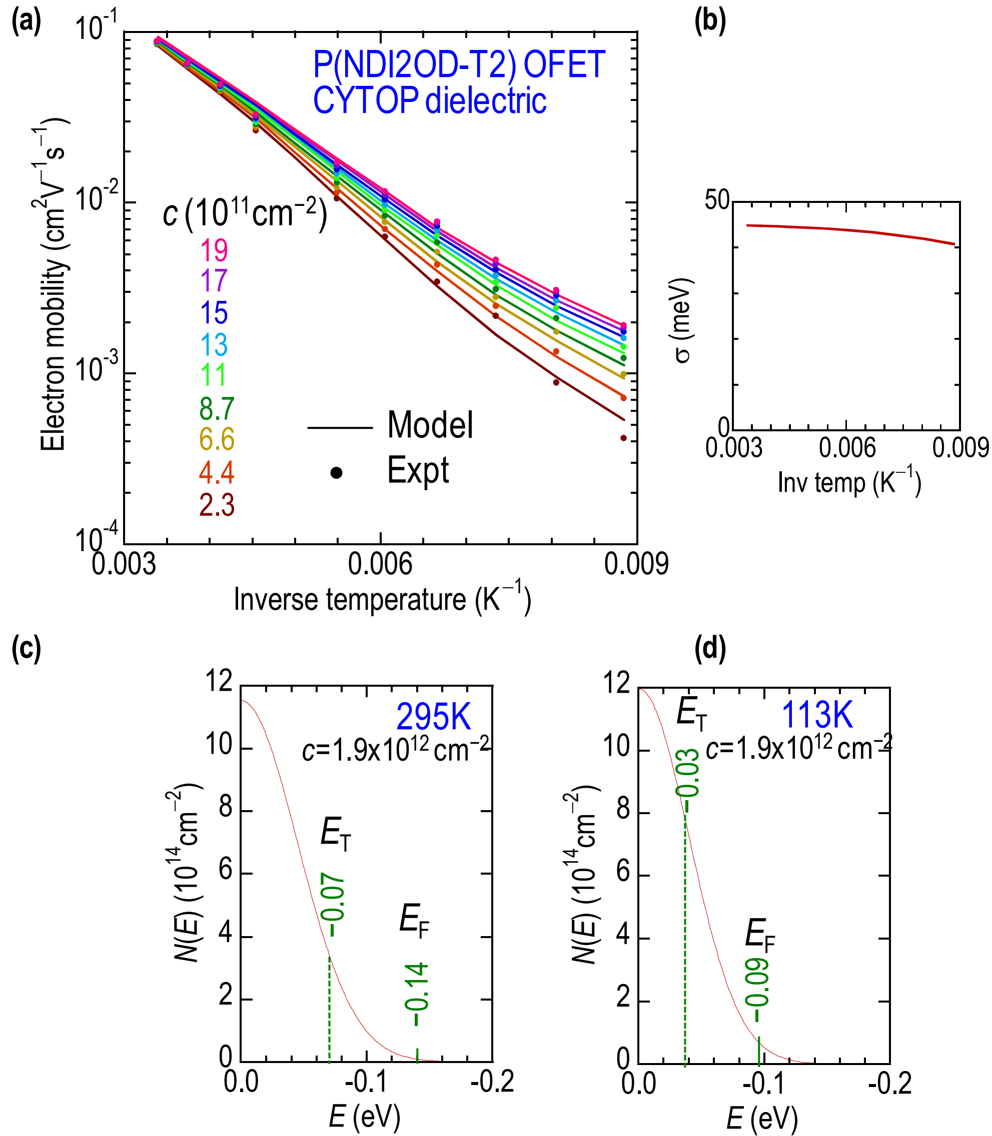

Figure 6.3 Fitting results for P(NDI2OD-T2) TGBC FET With CYTOP dielectric. a) Experimental and simulated $\mu(c,\ T)$ surface. b) Transport DOS width change with temperature in simulation. c) & d) Transport DOS together with transport level (E_T)and Fermi level (E_F) for c = 1.9 x 10^{12} cm^{-2} for CYTOP-gated device at 295 K and 113 K respectively.

Other transport parameters for this device is $<\alpha d>$ = 1.8 and ξ = 1.35. The $<\alpha d>$ parameter is larger than both that of rrP3HT(*ca*. 1.1) and PBTTT (*ca*. 0.8 – 0.9). It shows that interchain coupling is slightly worse despite similar π stacking distance (3.65 Å) with PBTTT-C14 (3.6 Å) and rrP3HT (3.7 Å). This is likely to be due to poor

overlapping between neighboring polymer chains considering its face-on stacking structure. So hopping in the π-stacking direction in P(NDI2OD-T2) is not as favorable as in P3HT and PBTTT where the polymer chains have well ordered edge-on π-stacking structure. As a result, its value $<\alpha d>$ becomes larger. The connectivity parameter ξ is between that of rrP3HT (*ca*. 0.3) and PBTTT (*ca*. 4 − 5 except P6). The better connection between aggregates in P(NDI2OD-T2) than in rrP3HT is possibly due to better charge transport along long polymer chain whose electronic structure is not sensitive to chain deformation from twisting etc, compared to that of rrP3HT chain which is more sensitive to those changes. The even better connectivity in PBTTT is because in PBTTT films the domains/sub-domains closely pack together therefore the equivalent distance between aggregates are much smaller than that in P(NDI2OD-T2) and rrP3HT. So charge carriers can transport comparably very easily between domains.

Figure 6.4a shows the experimental and simulated $\mu(c, T)$ surfaces for PS-gated device. Similarly, the symbols are the experimental results, and the lines are the simulations. The measured temperature range is 113 – 295 K, and carrier-density range is 0.1 − 1.8 x 10^{12} cm^{-2}. Again excellent match of the two surfaces was obtained. There is a slight drop in mobility and increase in activation energy compared to CYTOP-gated device. The DOS for PS-gated device is taken the same as CYTOP-gated device as shown in Fig. 6.4b, since it is not sensitive to environment and not likely to be broadened by the PS dielectric layer. Other transport parameters for the PS device is $<\alpha d> = 2.5$ and $\xi = 3.4$. The worse interchain coupling and better connectivity is possibly due to microstructure change in the P(NDI2OD-T2) film as a result of solvent wash with *n*-butyl acetate during PS film spin-coating process. Figure 6.4c and d show the transport DOS tail at 295 K and 113 K respectively together with

the E_T and E_F energy levels for the highest carrier concentration c = 1.8x10^{12} cm^{-2}. The E_T lies near -1σ at low T or even lower at high T, basically same as that in CYTOP-gated device.

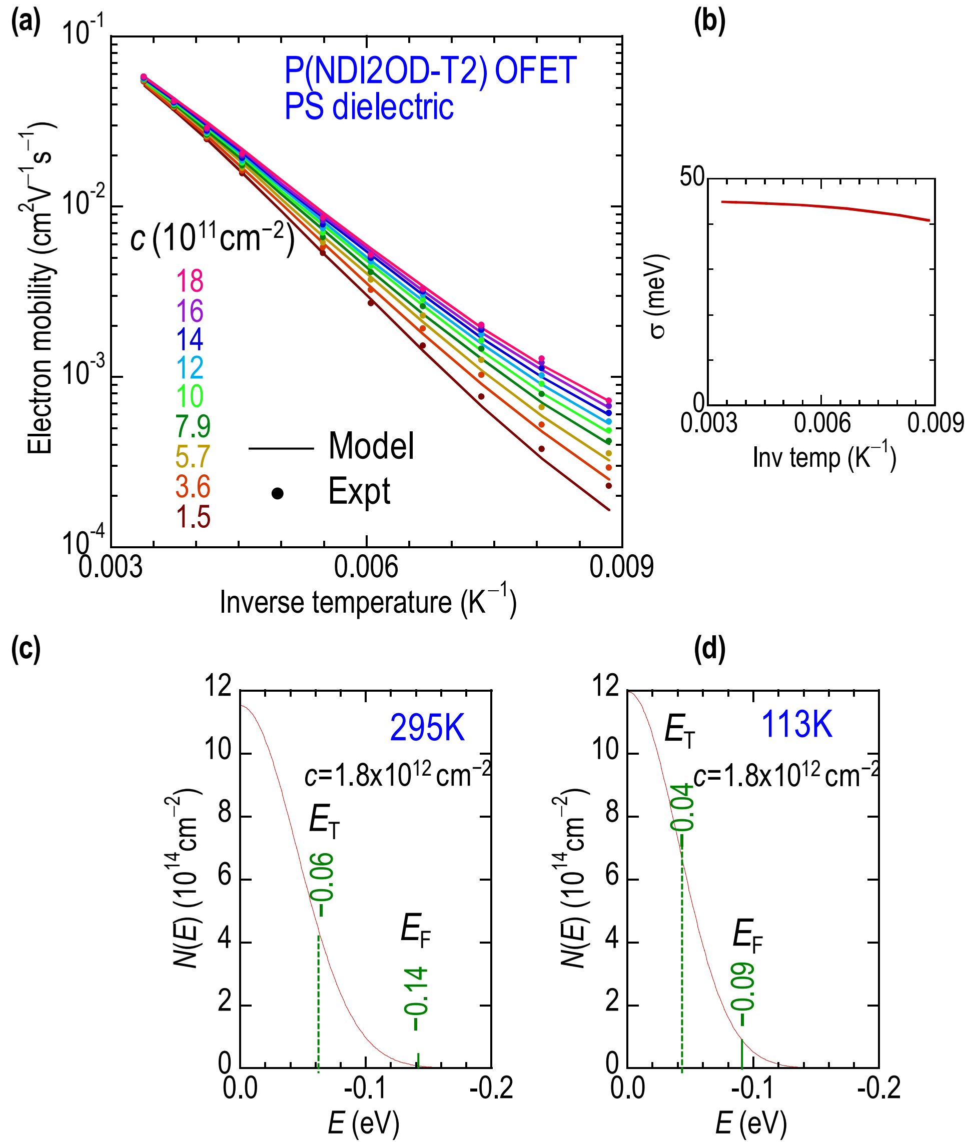

Figure 6.4 Fitting results for P(NDI2OD-T2) TGBC FET With PS dielectric. (a) Experimental and simulated $\mu(c, T)$ surface. (b) Transport DOS width change with temperature in simulation. (c) & (d) Transport DOS together with transport level (E_T)and Fermi level (E_F) for c = 1.8 x 10^{12} cm^{-2} for PS-gated device at 295 K and 113 K respectively.

6.4 Conclusion

We have used the model to study the charge transport in P(NDI2OD-T2) BGTC FET devices. The study shows that P(NDI2OD-T2) has much narrower transport DOS compared to rrP3HT and PBTTT, together with very small DOS width change with temperature. This is the primary reason for the high electron mobility in P(NDI2OD-T2) despite its slightly worse interchain coupling and intermediate connectivity between aggregates. The study shows that narrow transport DOS, good interchain coupling and connectivity between aggregates are key factors in charge transport process to achieve high FET mobility.

6.5 References

1 Kang, I., Yun, H. J., Chung, D. S., Kwon, S. K. & Kim, Y. H. Record High Hole Mobility in Polymer Semiconductors via Side-Chain Engineering. *J. Am. Chem. Soc* **135**, 14896 (2013).

2 Sun, B., Hong, W., Yan, Z., Aziz, H. & Li, Y. Record High Electron Mobility of 6.3 $cm^2 V^{-1} s^{-1}$ Achieved for Polymer Semiconductors Using a New Building Block. *Adv. Mater.*, doi:10.1002/adma.201305981 (2014).

3 Zhang, W. M. *et al.* Indacenodithiophene Semiconducting Polymers for High-Performance, Air-Stable Transistors. *J. Am. Chem. Soc* **132**, 11437 (2010).

4 Tsao, H. N. *et al.* Ultrahigh Mobility in Polymer Field-Effect Transistors by Design. *J. Am. Chem. Soc* **133**, 2605 (2011).

5 Nielsen, C. B., Turbiez, M. & McCulloch, I. Recent advances in the development of semiconducting DPP-containing polymers for transistor applications. *Adv. Mater.* **25**, 1859 (2013).

6 Chen, Z. Y. *et al.* High-Performance ambipolar Diketopyrrolopyrrole-Thieno 3,2-b thiophene copolymer Field-Effect Transistors with balanced hole and electron mobilities. *Adv. Mater.* **24**, 647 (2012).

7 Baeg, K. J. *et al.* Remarkable enhancement of hole transport in top-gated n-Type polymer field-effect transistors by a high-k dielectric for ambipolar electronic circuits. *Adv. Mater.* **24**, 5433 (2012).

8 Kronemeijer, A. J. *et al.* A Selenophene-Based Low-Bandgap Donor-Acceptor Polymer Leading to Fast Ambipolar Logic. *Adv. Mater.* **24**, 1558 (2012).

9 Zhang, Z. G. & Wang, J. Z. Structures and properties of conjugated Donor-Acceptor copolymers for solar cell applications. *J. Mater. Chem.* **22**, 4178 (2012).

10 Sirringhaus, H. 25th Anniversary Article: Organic Field-Effect Transistors: The Path Beyond Amorphous Silicon. *Adv. Mater.* **26**, 1319 (2014).

11 Caironi, M. *et al.* Very Low Degree of Energetic Disorder as the Origin of High Mobility in an n-channel Polymer Semiconductor. *Adv. Func. Mater.* **21**, 3371 (2011).

12 Niedzialek, D. *et al.* Probing the Relation Between Charge Transport and Supramolecular Organization Down to Angstrom Resolution in a Benzothiadiazole-Cyclopentadithiophene Copolymer. *Adv. Mater.* **25**, 1939 (2013).

13 Zhang, X. R. *et al.* Molecular Packing of High-Mobility Diketo Pyrrolo-Pyrrole Polymer Semiconductors with Branched Alkyl Side Chains. *J. Am. Chem. Soc.* **133**, 15073 (2011).

14 Zhang, X. R. *et al.* Molecular origin of high field-effect mobility in an indacenodithiophene-benzothiadiazole copolymer. *Nat. Commun.* **4**, 3238 (2013).

15 Rivnay, J. *et al.* Unconventional Face-On Texture and Exceptional In-Plane Order of a High Mobility n-Type Polymer. *Adv. Mater.* **22**, 4359 (2010).

16 Rivnay, J. *et al.* Drastic Control of Texture in a High Performance n-Type Polymeric Semiconductor and Implications for Charge Transport. *Macromol.* **44**, 5246 (2011).

17 Lee, J. *et al.* Solution-Processable Ambipolar Diketopyrrolopyrrole-Selenophene Polymer with Unprecedentedly High Hole and Electron Mobilities. *J. Am. Chem. Soc.* **134**, 20713 (2012).

18 Noriega, R. *et al.* A general relationship between disorder, aggregation and charge transport in conjugated polymers. *Nat. Mater.* **12**, 1037 (2013).

19 Yan, H. *et al.* A high-mobility electron-transporting polymer for printed transistors. *Nature* **457**, 679 (2009).

20 Lim, Y. H. Charge transport behaviour of n-type polymer field-effect transistors. (2013).

21 Schuettfort, T. *et al.* Surface and Bulk Structural Characterization of a High-Mobility Electron-Transporting Polymer. *Macromol.* **44**, 1530 (2011).

22 Zhuo, J. M. *et al.* Evidence for a transistion adlayer interface structure that determines the field-effect transport in semicrystalline polymer organic semiconductor films (Manuscript in preparation).

23 Rivnay, J., Noriega, R., Kline, R. J., Salleo, A. & Toney, M. F. Quantitative analysis of lattice disorder and crystallite size in organic semiconductor thin films. *Phys. Rev. B* **84**, 045203 (2011).

Chapter 7. Summary and outlook

We have developed a self-consistent 2D variable-range hopping model for organic field -effect transistors with only these three fitting parameters: the transport DOS tail shape, the interchain coupling parameter and the connectivity parameter, to study the experimentally observed rich diversity of transport behavior for a number of important families of polymer semiconductors, including rrP3HT, PBTTT and P(NDI2OD-T2). From the systematic study, we show that variable-range-hopping at the macroscopic level provides an appropriate basis to quantitatively understand field-induced transport in these materials. Furthermore, it shows that narrow transport DOS, good interchain coupling and good connectivity between aggregates are key factors in charge transport process to achieve high FET mobility, as shown in Table 7.1 below.

The rapid increase of charge carrier mobility in polymer FETs in recent few years is an exciting breakthrough. It pushes the polymer semiconductors to the edge of long-awaited large scale application in low-cost, flexible plastic electronics. Apart from work in this thesis, the model could be used to study the fundamental properties of other recently reported high performance materials. With systematic study, this could let us understand the link between the chemical structures and the electric properties of the materials. It would lead to an in-depth understanding and a clearer picture of charge transport physics in polymer semiconductors; also provide guidelines for developing materials with even higher mobility to meet the performance requirements in real applications.

Material	Experiment conditions	$\langle \alpha d \rangle$	ξ	σ(meV) at 295K
P3HT	alkyl-SiO_2	1.1	0.38	95
	perfluoroalkyl-SiO_2		0.30	n.a.
	TMS-SiO_2		0.03	n.a.
PBTTT	P22	0.8	4.4	131
	P11	0.8	5.3	132
	P6	0.9	1.6	104
	P3A	0.7	5.6	111
	P3B	0.9	0.6	113
	P3C	0.8	3.6	144
P(NDI2OD-T2)	CYTOP	1.8	1.35	45
	PS	2.5	3.4	

Table 7.1 Summary of extracted parameters for all materials and experiment conditions studied in this thesis.

Appendix A. Disorder broadened π-band edge fitting

In polymer semiconductors, the disorder causes the HOMO edge of the Density of States (DOS) of π-band to broaden. Here we study the broadening effect by convolution of a uniform DOS (height h_0) and a Gaussian function (width σ_{dis}), which represents the simplified DOS of real π-band and the disorder in the system respectively. The broadened DOS edges are shown in Fig. A.1a. The majority part of the tail of the broadened edge could be fitted well with a single Gaussian function (width σ) for all calculated results, an example of the fitting is shown in Fig. 3.1(c) for $\sigma_{dis} = 80$ meV. Fig. A.1b shows the parameters of the fitted Gaussian function, which suggests the broadened tail generally could be fitted with a Gaussian with peak height $A = 0.913h_0$, width $\sigma = 1.13\sigma_{dis}$, center position at 5 eV + $1.52\sigma_{dis}$.

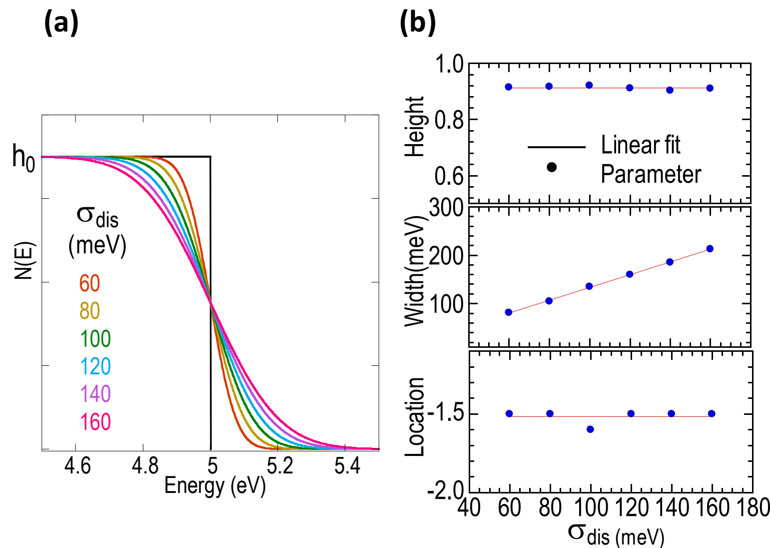

Figure A.1 Convolution of uniform DOS (width 10 eV) with Gaussian disorder (width σ_{dis}). (a) Broadening at the edge after convolution compared to the uniform DOS (black line). (b) The parameters of the single Gaussian function that can best fit the broadened DOS tail. From top to bottom: peak height normalized to uniform DOS

height, width, Difference of the original DOS edge (5 eV) with its center location, normalized by σ_{dis}.

Appendix B. FET mobility extraction

Mobility Equation: The $\mu(c, T)$ surface is extracted from FET transfer curves measured at temperature points from 77 K to 295 K. The transfer curve with small source-drain bias V_{sd} (normally 5 or 10 V) is used so that the FET device is in the linear region for a wide range of gate bias V_{gs}. At each temperature, the transfer curve is fitted with a low order polynomial function then the slope of the polynomial function at each V_{gs} point is used to calculate the linear mobility $\mu(c)$ by this equation:

$$\mu_{lin} = \frac{(dI_s / dV_{gs})L}{W \times V_{sd}' \times C}$$

Where dI_s / dV_{gs} is the slope, C is the capacitance of the dielectric layer, W and L are channel width and length respectively. V_{sd}' is voltage across the channel after the voltage loss at the source/drain contacts is corrected, which is generally needed for bottom-gate bottom-contact (BGBC) device. We assume the loss can be represented by a threshold voltage $V_{sd,th}$ so that $V_{sd}' = V_{sd} - V_{sd,th}$. The average carrier density in the channel is calculated from capacitor equation: $c = C(V_{gs} - V_{gs,th} - V_{sd}'/2)$, where $V_{gs,th}$ is the threshold for gate bias and $V_{sd}'/2$ is the source-drain bias at the middle point of the channel. In order to calculate mobility, we need to extract the two threshold voltages $V_{sd,th}$ and $V_{gs,th}$.

Threshold voltage extraction: The $V_{sd,th}$ is taken from $I_s - V_{sd}$ curve at high V_{gs} bias, according to the criterion that $I_s - V_{sd}$ curve is linear when V_{sd} is above $V_{sd,th}$. By fitting the linear region of the $I_s - V_{sd}$ curve region, $V_{sd,th}$ is taken as the interception point with x axis. Fig. B.1a shows an example of $V_{sd,th}$ extraction for P3HT BGBC FET

device with alkyl-SiO_2 dielectric at 295 K, for which $V_{sd,th}$ is determined to be around −15 V. The extraction should be done for all temperature points to check whether it is temperature dependent. It is temperature for this example device.

The $V_{gs,th}$ is taken roughly same to the onset voltage V_{on} to simplify the extraction process, while still can get the carrier density in the channel more or less accurately. Fig. B.1b shows an example of V_{on} extraction for P(NDI2OD-T2) TGBC FET device with CYTOP dielectric. It can be seen clearly that the device turns on around $V_{on} = 12$ V at all temperatures.

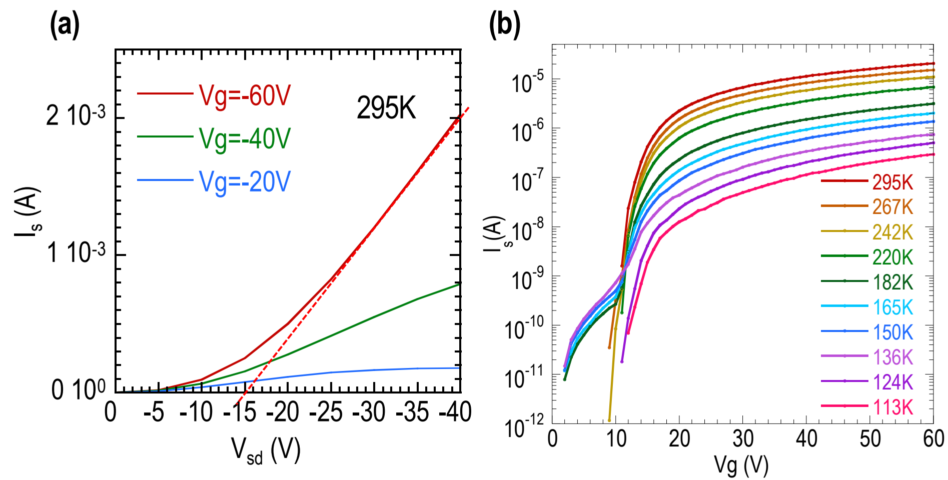

Figure B.1 (a) Example of threshold voltage extraction at source-drain contact. Data from rrP3HT BGBC FET device with alkyl-SiO_2 dielectric. (b) Example of threshold voltage extraction in gate bias V_{gs}. Data from P(NDI2OD-T2) TGBC FET device with CYTOP dielectric.

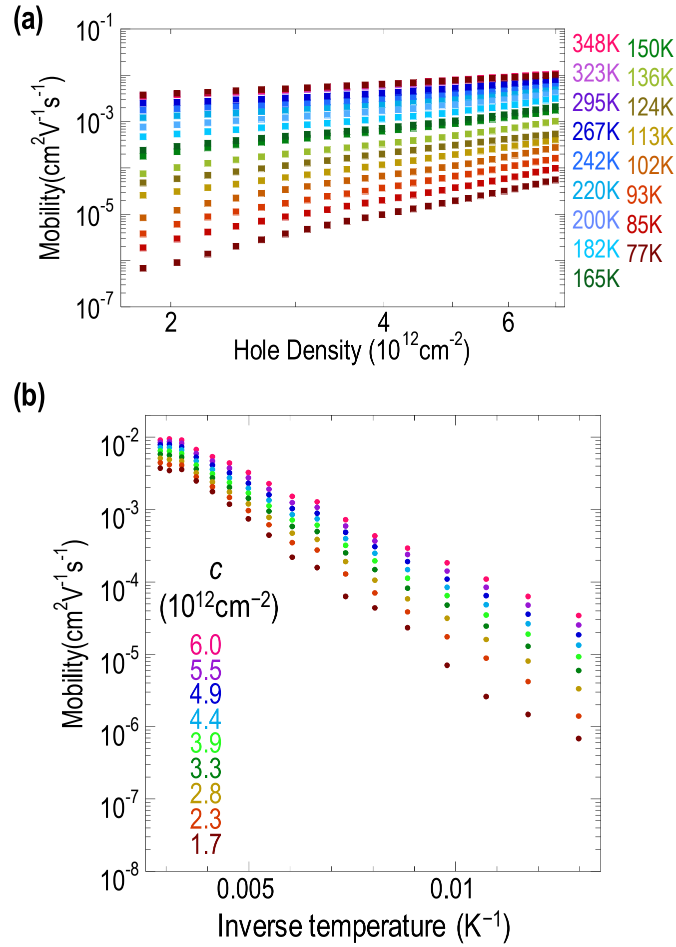

Figure B.2 (a) $\mu(c, T)$ surface plotted as $\mu(c)$ curves at different temperatures. (b) $\mu(c, T)$ surface plotted by $\mu(T)$ curves at different carrier densities, which is used for fitting. Data from rrP3HT BGBC FET device with alkyl-SiO_2 dielectric.

Mobility surface: With extracted $V_{sd,th}$ and $V_{gs,th}$ the $\mu(c)$ curve is calculated for each temperature, as shown in Fig. B.2a, then the $\mu(T)$ curves at selected carrier densities are plotted to give the $\mu(c, T)$ surface for model fitting, as shown in Fig. B.2b.

Appendix C. FET data fitting

From $\mu(c, T)$ surface shape fitting we can get DOS related parameters and the coupling parameter $<\alpha d>$. For example of fitting with Gaussian DOS, we only need to determine DOS width (σ) change with temperature and $<\alpha d>$. σ may vary with temperature while $<\alpha d>$ is constant.

For any given two temperature points (T_{high}, T_{low}) and carrier density points (c_{high} and c_{low}), we can define four values Δ1 − Δ4 as shown in Fig. C.1a. Fig. C.1b shows the calculated Δ1 − Δ4 under conditions: c_{high} and c_{low} = 6.0 x 10^{12} and 1.7 x 10^{12} cm^{-2}, T_{high} and T_{low} = 295 and 77 K respectively, with Gaussian DOS (fixed σ) for rrP3HT BGBC FET device with alkyl-SiO_2 dielectric as an example. The calculation result shows that Δ1 and Δ2 are only sensitive to σ unless the carrier concentration (p) is very high; Δ3 and Δ4 are sensitive to all parameters: σ, $<\alpha d>$ and p. For each σ, the allowed carrier concentration for c_{high} of the device can be determined according to equation which couples σ and c together. So σ at high and low temperatures (σ_{high} and σ_{low}) can be relatively easily estimated in the plot from experiment Δ1 and Δ2 respectively. The only other parameter $<\alpha d>$ can be estimated from experiment Δ3 and Δ4. Then the three estimated parameters (σ_{high}, σ_{low} and $<\alpha d>$) are used to generate a set of Δ1 − Δ4, based on which we can adjust these parameters in iteration process until the calculated and experiment Δ1 − Δ4 match each other. The process is repeated for several temperatures to get a few σ points, which is fitted to get $\sigma(T)$ curve, the $\sigma(T)$ curve is used together with $<\alpha d>$ to generate theoretical $\mu(c, T)$ surface to match experiment $\mu(c, T)$ surface. Fine adjustments of fitting parameters in iteration process are needed to get good match.

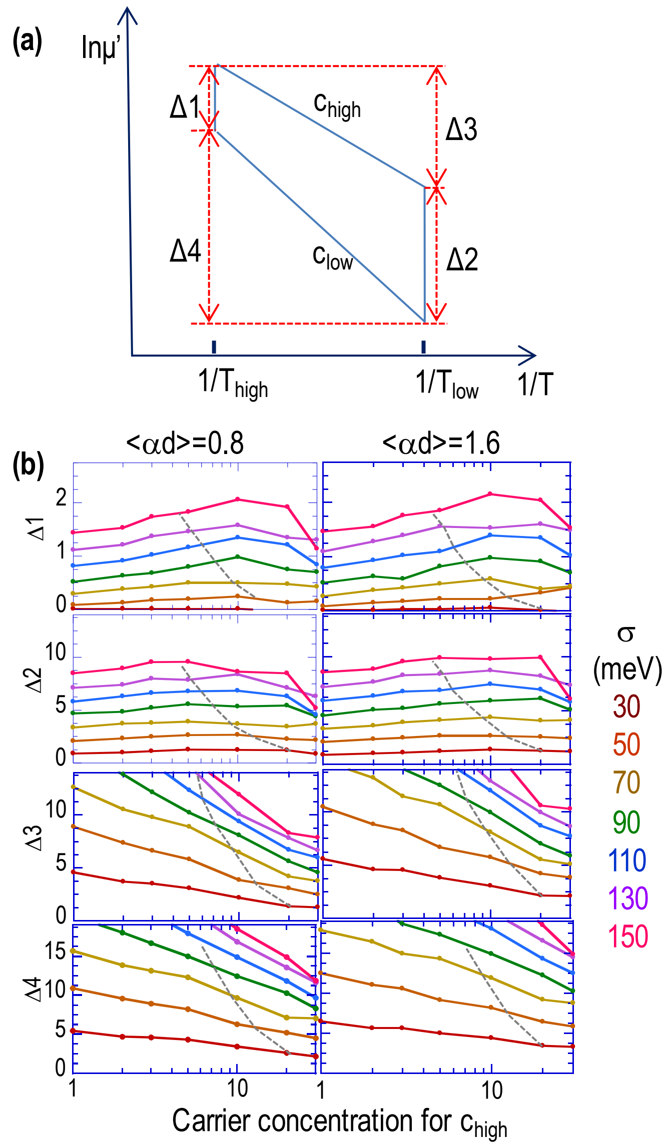

Figure C.1 (a) Δ1 – Δ4 defined by the four (c,T) points. (b) Calculated Δ1 – Δ4 for rrP3HT BGBC FET device with alkyl-SiO_2 dielectric, using Gaussian DOS (fixed width σ) under conditions: c_{high} and $c_{low} = 6.0 \times 10^{12}$ and 1.7×10^{12} cm^{-2}, T_{high} and T_{low} = 295 and 77 K. Grey lines give the allowed carrier concentration for this device at each σ, which comes from the coupling between carrier concentration and σ.

Appendix D. Hopping transport in square lattice

We also study the hopping transport in square lattice in R space, in which charge carriers are allowed to hop in all directions and α form uniform distribution. Apart from this, all the other assumptions are same as those in the cross lattice model. This cross lattice model predicts very similar charge transport behavior as the cross lattice model, and gives similar fitting result for rrP3HT BGBC FET device with alkyl-SiO_2 dielectric, as shown in Fig. D1−5. The difference of these two models only shows at low temperature.

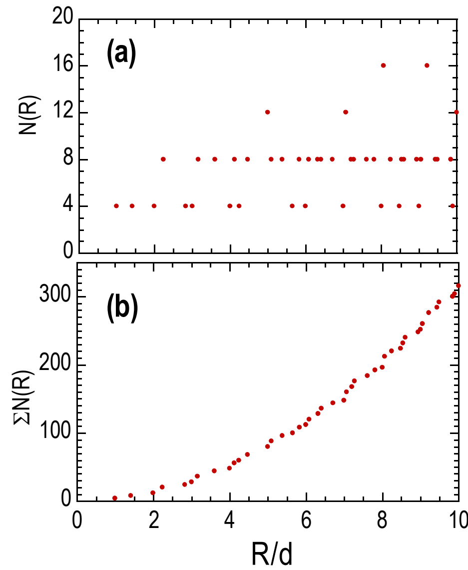

Figure D.1 In square lattice, (a) the number of neighbors $N(R)$ at distance R (R is normalized by lattice constant d), (b) total number of neighbors $\Sigma N(R)$ within distance R.

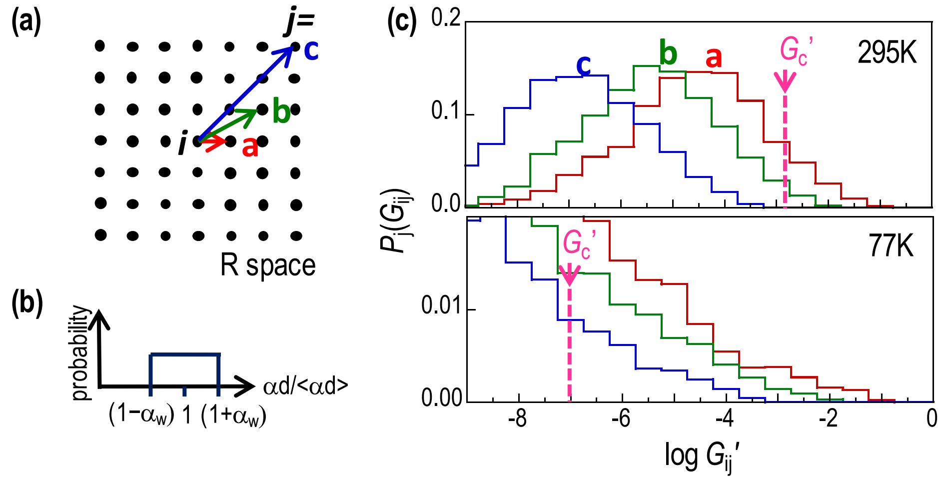

Figure D.2 Variable-range hopping in square lattice. (a) Illustration of hopping to neighbors at different distances in R space. (b) Uniform distribution of αd. (c) Distribution of reduced conductance G_{ij}' for hopping paths to neighbor sites a, b and c at 295 K and 77 K with Gaussian DOS ($\sigma = 90$ meV) and a uniform distribution ($<\alpha> = 0.85$ and $\alpha_w = 0.06$). The reduced conductance G_c' of the resistor network is determined by using bond percolation number $B_c = 2$.

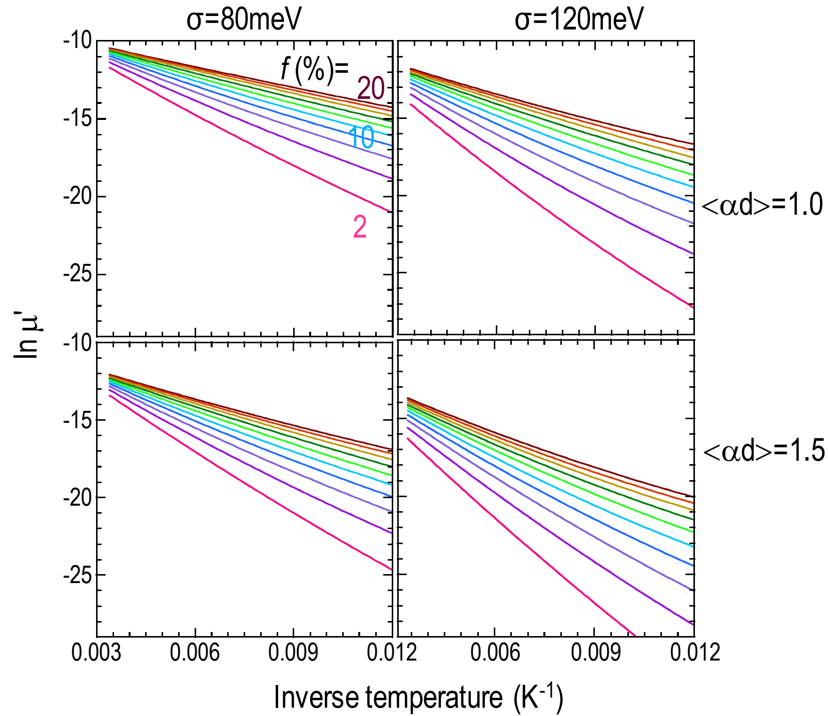

Figure D.3 Calculated reduced mobility μ' in square lattice with Gaussian DOS.

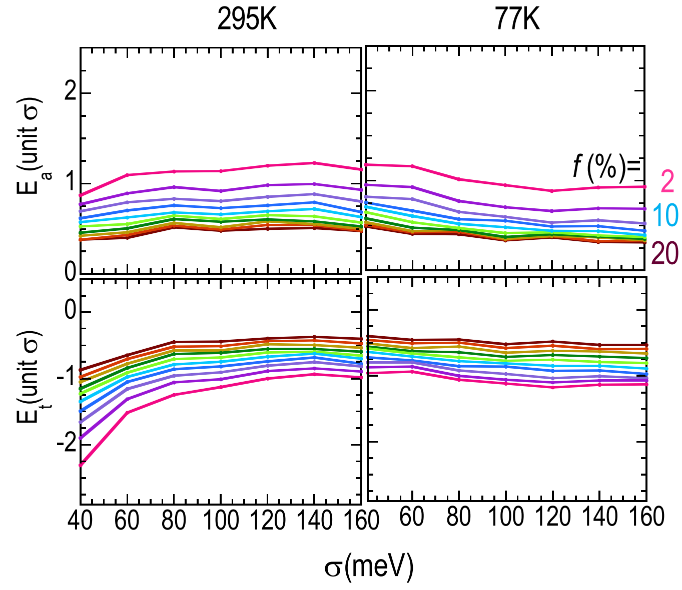

Figure D.4 Calculated Activation energy (E_A) of mobility and Transport levels (E_T) at different carrier concentrations (f = 2 – 20 %, interval 2 %) with Gaussian DOS (width σ) and $<\alpha d> = 1.0$ in square lattice.

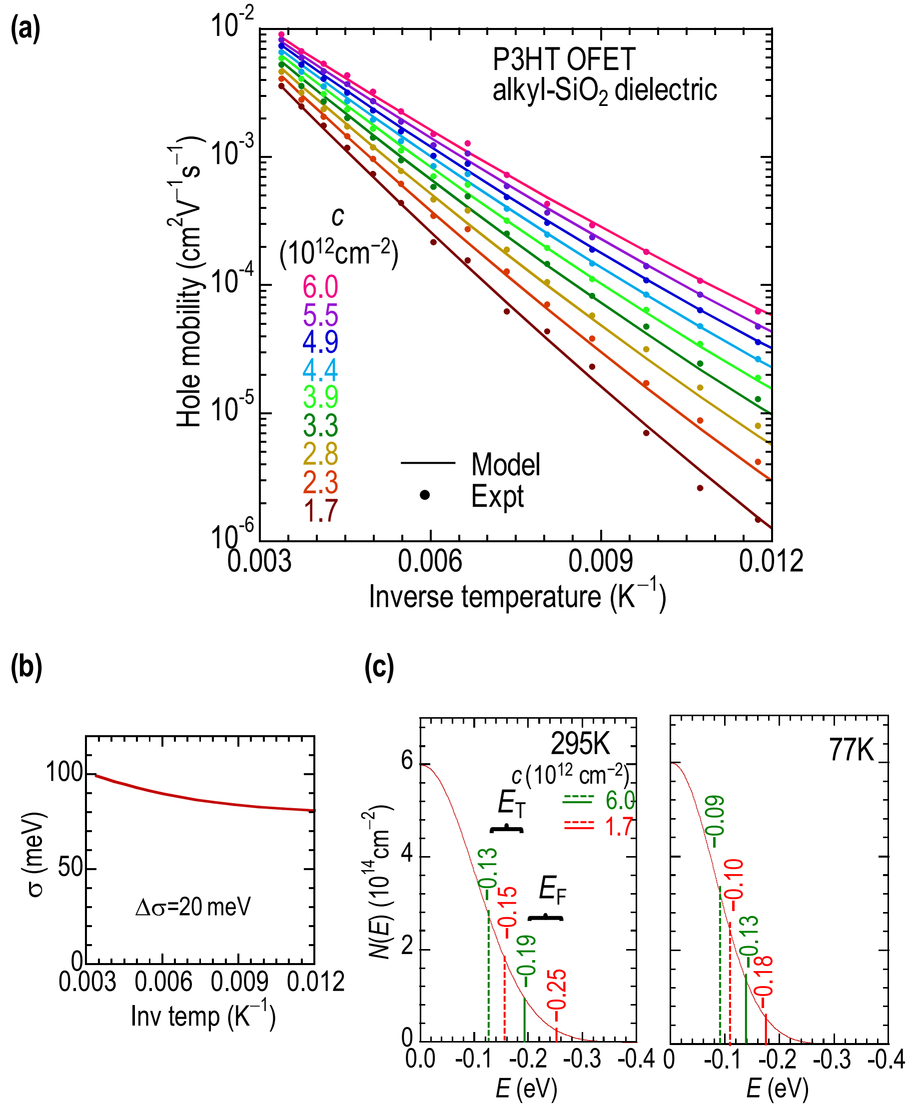

Figure D.5 Fitting result for rrP3HT OFET with alkyl-SiO_2 dielectric in square lattice (a) Comparison of experimental and simulated $\mu(c,\ T)$ surfaces, $\sigma = 100$ meV at 295 K and 80 meV at 77 K, $<\alpha d> = 0.85$, $\xi = 0.36$. (b) Transport DOS width narrowing with temperature decreasing. (c) The transport DOS at 295 K and 77 K, together with the transport levels (E_T) and Fermi levels (E_F) for high and low carrier densities.